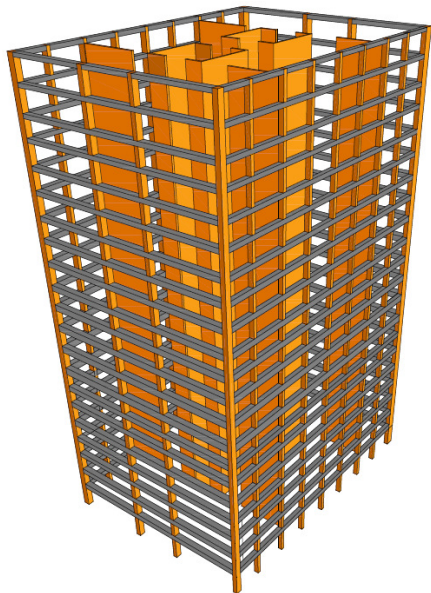


WIND AND EARTHQUAKE DESIGN FRAMEWORK FOR TALL WOOD-CONCRETE HYBRID SYSTEM



PRINCIPAL INVESTIGATOR

Dr. Solomon Tesfamariam, P.Eng.
(Professor, UBC Okanagan Campus)

STUDENTS

Matiyas Bezabeh
(PhD Candidate, UBC Okanagan Campus)
(Visiting research student, Western University)

Konstantinos Skandalos
(PhD Student, UBC Okanagan Campus)

Edel Martinez
(PhD Student, UBC Okanagan Campus)

Selamawit Dires
(PhD Student, UBC Okanagan Campus)

ACADEMIC COLLABORATORS

Dr. Girma Bitsuamlak, P.Eng.
(Associate Professor, Canada Research Chair in Wind
Engineering, Director Boundary Layer Wind Tunnel
Laboratory, Western University)

Dr. Katsuichiro Goda
(Associate Professor, Western University)

Final Report

August 2019

Prepared for:

Forestry Innovation Investment Ltd.
#1200 - 1130 West Pender Street, Vancouver, BC Canada V6E 4A4

By:

Dr. Solomon Tesfamariam, P.Eng.
The University of British Columbia
3333 University Way, Kelowna, BC Canada V1V 1W7

Disclaimers

This report includes a seismic and wind design for RC-timber hybrid structure consisting CLT walls, glulam columns and RC beams. Other ways of conducting the wind analysis, seismic analysis and design are possible, and they may result in different demands on the building. The connections detailing in this report were chosen to represent the use of off-the shelf solutions, and other ways of connection detailing are available. The report has no intention of promoting or endorsing any particular proprietary connection or building system.

The authors have taken reasonable actions and due diligence to ensure the accuracy of the information provided in this report; however, THE AUTHORS, UNIVERSITY OF BRITISH COLUMBIA, OR OTHER CONTRIBUTORS ASSUME NO LIABILITY FOR ANY DIRECT OR INDIRECT DAMAGE, INJURY, LOSS OR EXPENSE THAT MAY BE INCURRED OR SUFFERED AS A RESULT OF THE USE OF THIS REPORT INCLUDING WITHOUT LIMITATION PRODUCTS, BUILDING TECHNIQUES OR PRACTICES. The authors do not guarantee the completeness of the information published in this report. Users of this report agree to use the information in this report (analysis suggestions, design procedures, detailing, etc.) at their own risk. We will not be liable for any errors, inaccuracies, omissions or damages arising from the use of the information presented in this report, nor any action taken in reliance to the presented information.

Building science, products and construction practices change and improve over time and rather than relying on this report, it is advisable to: (a) regularly consult up-to-date technical publications on products and practices, (b) seek specific information and professional advice on the use of products mentioned in this report from manufacturers or suppliers of the products and consultants with appropriate qualifications and experience, and (c) review and comply with the specific requirements of the applicable building codes for each construction project.

The wind design process and results of the 10- and 30-storey mass-timber buildings are presented in this report were published (the Journal of Wind Engineering and Industrial Aerodynamics and Engineering Structures) and presented at the World Conference on Timber Engineering-WCTE 2018 (Seoul, South Korea) and the 2018 Canadian Society for Civil Engineering, Structural Specialty Conference (Fredericton, NB, Canada). The papers included in the conference proceedings and published in the journals by the authors of this report are:

- 1) Bezabeh, M. A., Bitsuamlak, G. T., Popovski, M., and Tesfamariam, S. (2018). Probabilistic serviceability-performance assessment of tall mass-timber buildings subjected to stochastic wind loads: Part I-structural design and wind tunnel testing. *Journal of Wind Engineering and Industrial Aerodynamics*, 181, 85-103.
- 2) Bezabeh, M. A., Bitsuamlak, G. T., Popovski, M., and Tesfamariam, S. (2018). Probabilistic serviceability-performance assessment of tall mass-timber buildings subjected to stochastic wind loads: Part II-structural reliability analysis. *Journal of Wind Engineering and Industrial Aerodynamics*, 181, 112-125.
- 3) Bezabeh, M. A., Bitsuamlak, G. T., Popovski, M., and Tesfamariam, S. (2018). Structural Performance of multi-story mass-timber buildings under tornadic wind fields. *Engineering Structures*, 177, 519-539.
- 4) Bezabeh, M. A., Bitsuamlak G., Popovski, M., and Tesfamariam, S., (2018). Probabilistic serviceability-performance assessment of tall mass-timber buildings subjected to stochastic wind loads. World Conference on Timber Engineering, August 19-23, Seoul, South Korea.
- 5) Bezabeh, M. A., Gairola A., Bitsuamlak G., Popovski, M., and Tesfamariam, S., (2018). On the Lateral Stability of Multi-Story Mass-Timber Buildings Subjected to Tornado-Like Wind Field. World Conference on Timber Engineering, August 19-23, Seoul, South Korea.
- 6) Bezabeh, M. A., Bitsuamlak G., and Tesfamariam, S. (2018). Risk-based wind design of tall mass-timber buildings. The 2018 Canadian Society for Civil Engineering, Structural Specialty Conference, Fredericton, NB, Canada.

Acknowledgements

Development of the design guideline in this project was supported through the BC Forestry Innovation Investment's (FII) Wood First Program. The Wind and Earthquake Design Framework for Tall Wood-Concrete Hybrid System, is collaborative work between researchers at the University of British Columbia (UBC) and Western University. Under the supervision of Dr. Tesfamariam, various students have contributed to the knowledge presented in this report:

- Matiyas Bezabeh (Dr. Tesfamariam's and Dr. Bitsuamlak's PhD student) has carried out the wind tunnel test at Western University and developed the probabilistic based design under wind loads.
- Konstantinos Skandalos (Dr. Tesfamariam's PhD student) was actively involved in the seismic design, OpenSees modelling, simulation and final report writing.
- Selamawit Dires (Dr. Tesfamariam's PhD student) was actively involved in early part of the seismic design archetype development.
- Edel Rolando Martínez (Dr. Tesfamariam's PhD student) was actively involved in the seismic design of the hybrid building.

Table of Contents

Disclaimers	iii
Table of Contents.....	vi
List of Figures.....	ix
Chapter 1 Background	14
1.1 Motivation	14
1.2 Concrete jointed mass timber-based hybrid structures.....	15
Chapter 2 Wind Tunnel Model Tests of Tall-Wood Buildings	16
2.1 Introduction	16
2.2 Facility overview	16
2.3 High-frequency pressure integration test.....	17
2.4 Building model descriptions.....	18
2.4.1 Tap layout design.....	18
2.4.2 Tributary areas for taps	20
2.4.3 Model manufacturing.....	21
2.5 Experimental setup, instrumentation, and data acquisition	21
2.6 Wind tunnel tests	24
2.6.1 Boundary layer wind field simulation	24
2.6.2 Experimental results	24
2.6.3 Statistics of pressure coefficients.....	28
Chapter 3 Wind-induced Response and Serviceability-Performance Assessment of Tall Mass-timber Buildings.....	32
3.1 Description of the studied case study mass-timber buildings	32
3.2 Structural design of the tall-mass timber building	33
3.2.1 Design of gravity load resisting system.....	34

3.2.2 Design of lateral load resisting systems.....	34
3.2.3 Design of modified HSK connectors	35
3.2.4 Design of RC link beams and spandrel beams	35
3.3 Modal analysis.....	36
3.4 Dynamic structural analysis	38
3.5 Preliminary load factor for serviceability design of tall mass-timber buildings	46
Chapter 4 Archetype Development and Seismic Design	52
4.1 Archetype building	52
4.2 Seismic design	54
4.3 Numerical modeling and analysis considerations	54
Chapter 5 OpenSees Numerical Model.....	57
5.1 Introduction	57
5.1 CLT wall connections.....	59
5.2 Hold downs.....	61
5.3 Shear connections	62
5.4 Modelling CLT wall panels.....	63
5.5 System-level behavior	63
5.5.1 Wall meshing	63
5.5.2 CLT floors.....	64
5.5.3 Beam-to-wall interface	64
5.5.4 Wall-to-wall interface	64
5.5.5 Modeling of reinforced concrete link beams in the coupled-wall system	65
Chapter 6 Overstrength and Ductility Factors using Static Pushover Analysis.....	68
6.1 Capacity (pushover) curves	69

6.1.1 Pushover of uncoupled system	69
6.1.2 Pushover of coupled system	70
6.2 Static pushover to IDA (SPO2IDA)	71
Chapter 7 Seismic Hazard for Vancouver and Ground Motion Selection.....	76
7.1 Introduction	76
7.2 Seismic hazard in Vancouver	79
7.3 Ground motion database for real mainshock-aftershock records	82
7.4 Record selection of mainshock-aftershock sequence records for tall wood-concrete hybrid structural systems.....	84
Chapter 8 Validation of Proposed R_d and R_o Factors	88
8.1 Check for collapse prevention limit state according to NBCC 2015	88
8.2 FEMA P695 collapse risk performance evaluation.....	89
8.3 Performance assessment of the proposed R_d factors using incremental dynamic analysis (IDA)	92
8.3.1 Incremental dynamic analysis results	92
8.3.2 Total system uncertainty	95
8.3.3 Collapse fragility curves	95
Chapter 9 Conclusions and Future Recommendations	98
9.1 Wind tunnel testing and wind serviceability performance assessment study conclusions	98
9.2 Seismic design factors conclusions	100
9.3 System limitations and future recommendations	101

List of Figures

Figure 2.1: Schematics of the BLWTL.....	17
Figure 2.2: BLWTL interior views: a) roughness blocks; b) interior view of the tunnel with pitot tubes at the “gradient height.”	17
Figure 2.3: a) Typical test setup at BLWTL; b) Spires, roughness blocks and end barriers at BLWTL to generate turbulent wind flow	17
Figure 2.4: Roof tap layout	19
Figure 2.5: Pressure taps layout of the 40-storey building; a) Front view b) side view c) 3D view.....	19
Figure 2.6: Various building heights considered for wind tunnel testing.....	20
Figure 2.7: Tributary areas on the surface of the 40-storey model	20
Figure 2.8: Rigid building model and instrumentations photo with pressure scanners	21
Figure 2.9: Arrangement of the pitot tubes inside the wind tunnel	22
Figure 2.10: a) Bug test on the model; b) Puffer to check the pressure taps	22
Figure 2.11: Boundary layer wind tunnel tests on the hybrid tall mass-timber building models at BLWTL.....	23
Figure 2.12: Comparison of simulated exposures with ESDU (1974) a) mean wind speed and turbulence intensity profiles; b) longitudinal wind spectra at 51 cm.....	25
Figure 2.13: Pressure taps location on 40-storey building model.....	26
Figure 2.14: Chord-wise C_p time series variation on the 40-storey building model for the 0° angle of attack	26
Figure 2.15: Height-wise C_p time series variations on the 40-storey building model for the 0° angle of attack	27
Figure 2.16: Reduced spectra plot of pressure fluctuations for selected pressure taps.....	27
Figure 2.17: Contour plots of mean C_p for 30-storey building for AOA = 0°	29
Figure 2.18: Contour plots of rms C_p for 30-storey building for AOA = 0°	29
Figure 2.19: Contour plots of kurtosis C_p for 30-storey building for AOA = 0°	30
Figure 2.20: Contour plots of skewness C_p for 30-storey building for AOA = 0°	30
Figure 2.21: Contour plots of peak C_p for 30-storey building for AOA = 0°	31
Figure 3.1: a) Typical floor plan of the case study buildings, b) HSK connector, c) 3D view of 30-storey mass timber building without floor.....	33

Figure 3.2: Mode shapes and frequencies of the 40-storey tall wood building	36
Figure 3.3: Mode shapes and frequencies of the 30-storey tall wood building	37
Figure 3.4: Mode shapes and frequencies of the 20-storey tall wood building	37
Figure 3.5: Mode shapes and frequencies of the 15-storey tall wood building	37
Figure 3.6: Mode shapes and frequencies of the 10-storey tall wood building	38
Figure 3.7: Variation of spectra for open country exposure condition (Bezabeh et al. 2018a)	38
Figure 3.8: Time history response of 40-storey tall mass-timber building when AOA = 0°..	39
Figure 3.9: Time history response of 30-storey tall mass-timber building when AOA = 0°..	40
Figure 3.10: Time history response of 20-storey tall mass-timber building when AOA = 0°	41
Figure 3.11: Time history response of 15-storey tall mass-timber building when AOA = 0°	41
Figure 3.12: Structural response of 40-storey tall mass-timber building for various wind AOA	42
Figure 3.13: Structural response of 30-storey tall mass-timber building for various wind AOA	44
Figure 3.14: Structural response of 20-storey tall mass-timber building for various wind AOA	45
Figure 3.15: Structural response of 15-storey tall mass-timber building for various wind AOA	46
Figure 3.16: Variation of failure probability with a critical damping ratio	49
Figure 3.17: Fragility curves for deflection limit state suburban exposure case when AOA = 0° (Bezabeh et al. 2018b)	49
Figure 4.1: Lateral force resisting system: gravity columns and shear walls layout	52
Figure 4.2: 10-, 15- and 20-storey hybrid mass-timber buildings	53
Figure 4.4: Structural model representations of 20S-C building in ETABS	54
Figure 4.4: 5% damped response spectrum for Vancouver	56
Figure 5.1: Perspective view of the 10-storey uncoupled (10S-U) hybrid building	57
Figure 5.2: CLT shear wall assembly and connection detailing	58
Figure 5.3: Structural model representation in OpenSees	58

Figure 5.4: Modified HSK connection (Zhang 2017): a) Perforated steel plate with taped rows; b) Plates embedded and adhesively connected to CLT; c) Connection to stiff structural element	59
Figure 5.5: Calibrated modified HSK connection: a) with 11 shear links and 2 taped rows; b) with 23 shear links and 1 taped row	61
Figure 5.6: OpenSees elastic-no tension (ENT) material (http://opensees.berkeley.edu)	61
Figure 5.7: In-parallel formulation of the Steel02 and ENT uniaxial material models for hold-down simulation.....	62
Figure 5.8: Frame element modeling alternatives (Astroza <i>et al.</i> , 2015)	65
Figure 5.9: Modified Ibarra-Medina-Krawinkler peak-oriented model (http://opensees.berkeley.edu)	66
Figure 6.1: Illustration of seismic performance factors (R , Ω_o , and C_d) (from FEMA P695)	68
Figure 6.2: Ductility and force reduction factors of NBCC 2005 (Mitchell <i>et al.</i> 2003).....	69
Figure 6.3: Pushover analysis for the 10-storey uncoupled (10S-U) building: $R_d = 2$ and 3..	69
Figure 6.4: Pushover analysis for the 15-storey coupled (15S-C) building: $R_d = 2$	70
Figure 6.5: Pushover analysis for the 20-storey coupled (20S-C) building: $R_d = 2, 3$ and 4..	70
Figure 6.6: Sequence of link-beam (LB) damage in SPO for the coupled system; a) LB backbone; b) 15S-C with $R_d = 2.0$; and c) 20S-C with $R_d = 2.0$	71
Figure 6.7: SPO2IDA for the 10-storey uncoupled (10S-U) building: $R_d = 2$	71
Figure 6.8: SPO2IDA for the 10-storey uncoupled (10S-U) building: $R_d = 3$	72
Figure 6.9: SPO2IDA for the 15-storey coupled (15S-C) building: $R_d = 2$	72
Figure 6.10: SPO2IDA for the 20-storey coupled (20S-C) building: $R_d = 2$	72
Figure 6.11: SPO2IDA for the 20-storey coupled (20S-C) building: $R_d = 3$	73
Figure 6.12: SPO2IDA for the 20-storey coupled (20S-C) building: $R_d = 4$	73
Figure 6.13: ISDRs for the 10-storey uncoupled (10S-U) building: $R_d = 2$	74
Figure 6.14: ISDRs for the 15-storey-coupled (15S-C) building: $R_d = 2$	74
Figure 6.15: ISDRs for the 20-storey-coupled (20S-C) building: $R_d = 2$	75
Figure 7.1: Regional seismicity in south-western British Columbia, Canada	76
Figure 7.2: Uniform hazard spectra for Vancouver (Halchuk <i>et al.</i> , 2014, 2015)	80
Figure 7.3: Seismic hazard curves for Vancouver by distinguishing three contributing seismic sources.....	81

Figure 7.4: Seismic disaggregation for Vancouver – TR = 2475 years and for SA(T = 2 s) and SA(T = 5 s)	82
Figure 7.5: Magnitude–distance distribution of mainshock records and major aftershock records of the GM database	83
Figure 7.6: Histogram of average shear-wave velocity at recording sites of the GM database	84
Figure 7.7: Comparison of uniform hazard spectrum and conditional mean spectra for crustal, interface, and inslab records	85
Figure 7.8: Comparison of the response spectra of the selected records with the target response spectrum for T = 2.5 s	86
Figure 7.9: Comparison of the response spectra of the selected records with the target response spectrum for T = 3.6 s	87
Figure 8.1: Maximum inter-storey drift ratios for 2% in 50 years return period (design-based earthquake GMs) for 10S-U building, a) $R_d = 2$, and b) $R_d = 3$	88
Figure 8.2: Maximum inter-storey drift ratios for 2% in 50 years return period (design-based earthquake GMs) for $R_d = 2$, a) 15S-C and b) 20S-C buildings	89
Figure 8.3: Partial IDA method for the 10S-U building for $R_d = 2$ in Y direction: a) IDA curves, and b) Collapse fragility curve.....	93
Figure 8.4: Parametric analysis and derivation of maximum likelihood parameters for the partial IDA lognormal distribution	94
Figure 8.5: IDA curves of the 10S-U building in the Y direction: a) $R_d = 2$, and b) $R_d = 3$...	94
Figure 8.6: IDA curves for $R_d = 2$ in the Y direction, a) 15S-C and b) 20S-C buildings	95
Figure 8.7: Collapse fragility curves for the 10S-U building, a) $R_d = 2$, and b) $R_d = 3$	96
Figure 8.8: Collapse fragility curve for the $R_d = 2$, a) 15S-C and b) 20S-C buildings	96

List of Tables

Table 2.1: Parameters of wind tunnel testing.....	24
Table 3.1: Parameters of random variables (adopted from Bezabeh et al. 2018b)	48
Table 4.1: Material properties.....	55
Table 5.1: Calibration parameters of <i>IMK Bilin uniaxial material</i> for connection with 11 shear links and 2 covered rows.....	61
Table 6.1: preliminary CMR values of the 10- and 20-storey building based on SPO2IDA .	73
Table 7.1: First three fundamental periods of four buildings	78
Table 8.1: Quality rating of design requirements (FEMA 2009).....	90
Table 8.2: Quality rating of test data from an experimental investigation program (FEMA 2009)	90
Table 8.3: Quality rating of index archetype models.....	90
Table 8.4: Acceptable values of adjusted collapse margin ratio (ACMR _{10%} and ACMR _{20%}) (FEMA 2009).....	92
Table 8.5: Performance evaluation table per FEMA P695	97

Chapter 1

Background

1.1 Motivation

The use of wood in structural applications in Canada has been promoted by the wood industry and provincial governments. Several provinces, including British Columbia, have adopted a "Wood First Initiative" in order to create a "Culture of Wood Use." This initiative requires provincially-funded projects to use wood as the primary construction material and helps innovative design solutions to bring timber buildings to new heights. This provided designers a unique opportunity to take advantage of innovative designs (e.g. hybrid structures) and alternative solutions to overcome the building code's height restriction.

Through the NSERC network funded project (Network for Engineered Wood-based Building Systems, NewBuildS) and Forest Innovation Investment (FII), team of researchers from The University of British Columbia (UBC) and FPInnovations (FPI) have developed a timber-steel hybrid structural system that can potentially meet the current performance requirements and exceed the current building height limit. For steel-timber hybrid structures, a force-based design guideline, and corresponding ductility and overstrength seismic force modification factors, were developed (Tesfamariam *et al.*, 2015).

This report presents development of ductility and overstrength seismic force modification factors, and wind design guideline for timber-reinforced concrete (RC) hybrid building proposed by SOM (2013). Consistent to the FII's Wood First Program objectives, this research aimed in assisting the wood construction in public and private by adopting existing and emerging wood-based products and systems. Through this project, the following objectives are met:

- Keep BC's forest industry as a leading supplier of wood products and wood building technologies.
- With the use of a large volume of wood in tall buildings, it is envisioned to maximize the use of structural timber in governmental, public, and private projects.
- Provide a compressive wind and earthquake design guideline for tall timber buildings, which can be used as a reference by practicing engineers.
- By enhancing the confidence of construction stakeholders, increase the utilization of structural timber for tall buildings.
- Force modification factors from this research will provide a base to incorporate such factors required in force-based seismic design for the next generation of the British Columbia and Canadian building codes.

1.2 Concrete jointed mass timber-based hybrid structures

Advancement in engineered wood products altered the existing building height limitations and enhanced wooden structural members that are available on the market. These coupled with the need for a sustainable and green solution to address the ever-growing urbanization demand, avails wood as possible candidate for primary structural material in the construction industry. To this end, several researches carried out in the past decade to come up with sound structural solutions using a timber based structural system. Green and Karsh (2012) introduced the FFTT system; Tesfamariam *et al.* (2015) developed force-based design guideline for steel infilled with CLT shear walls, and SOM (2013) introduced the concrete jointed mass timber hybrid structural concepts. In this research, the basic structural concepts proposed by SOM (2013) is adopted.

The objective of this research is to develop a wind and earthquake design guideline for concrete jointed tall mass timber buildings in scope from 10- to 40-storey office or residential buildings. The specific objective of this research is as follow:

- Wind serviceability design guideline for hybrid mass-timber structures.
- Calibration of design wind load factors for the serviceability wind design of hybrid tall mass timber structures.
- Guidelines to perform probabilistic modeling, reliability assessment, and wind load factor calibration.
- Overstrength related modification factor R_o and ductility related modification factor R_d for future implementation in the NBCC.
- Force-based design guideline following the capacity based design principles.

Chapter 2

Wind Tunnel Model Tests of Tall-Wood Buildings

2.1 Introduction

In general, mass-timber buildings are lightweight and slightly more flexible than structures made from conventional construction materials. While their flexibility helps them to resist strong earthquakes, it limits their lateral stiffness, thus making them vulnerable to high along- and across-wind loads and the associated excessive vibration problems. Unlike earthquakes, wind loads can be affected by the surrounding, the structural form, height and shape of the building, the direction and speed of the approaching wind. Moreover, building codes such as NBCC 2015 (NRC 2015) and ASCE 7-10 (ASCE 2010) suggest wind tunnel experimental approaches for unusually lightweight, low frequency, and low damping buildings. Therefore, as a first step in the development of design guideline for wind sensitive mass-timber buildings, it is paramount to carry out an aerodynamic study using wind tunnel testing. From the aerodynamic study in this chapter, it is aimed to obtain floor-by-floor level wind load time history vectors of along-, across- and torsional-wind loads for various wind angles of attack. Using the wind load time history from the experimental tests, it is also aimed to perform a detail serviceability-performance assessment of the archetype buildings and an ultimate limit state design checks on the sections and connections of the main Lateral Load Resisting Systems (LLRS). Wind tunnel experimental design process consists of selecting the test type, instrumentation, experimental setups, and preliminary instrumentation and actuation checks. This chapter provides a detailed description of the wind tunnel experimental testing setups and methodology.

2.2 Facility overview

Wind flow around a bluff body is a complex phenomenon. Due to this complexity, in the wind engineering community, for accurate wind load and response estimations, experimental techniques are widely practiced. In this project, the wind tunnel testing was carried out at the Boundary Layer Wind Tunnel Laboratory (BLWTL) of Western University on the selected archetype building models was tested at 1:200 geometric scale using simulated boundary layer flows corresponding to an open country exposure condition. The wind tunnel has 39m long testing section that allows the development of a thick boundary layer like the natural wind flow over the terrain approaching the case study building. Figure 2.1 shows the schematics of the laboratory. At BLWTL different boundary layer wind flow can be obtained by adjusting floor roughness elements, spires, and end barriers (Figure 2.2 and Figure 2.3).

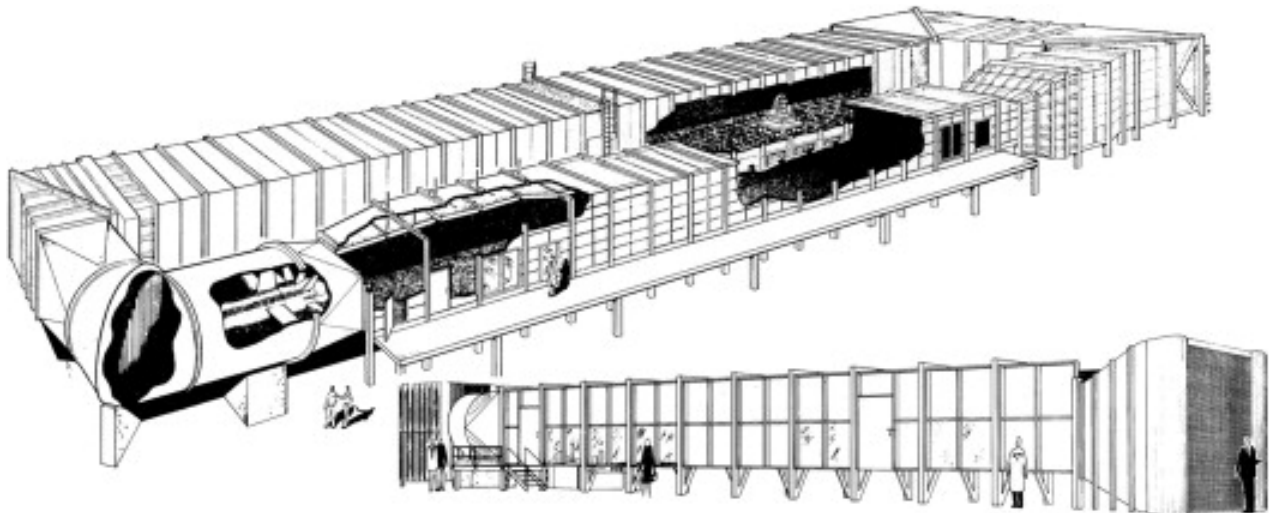


Figure 2.1: Schematics of the BLWTL

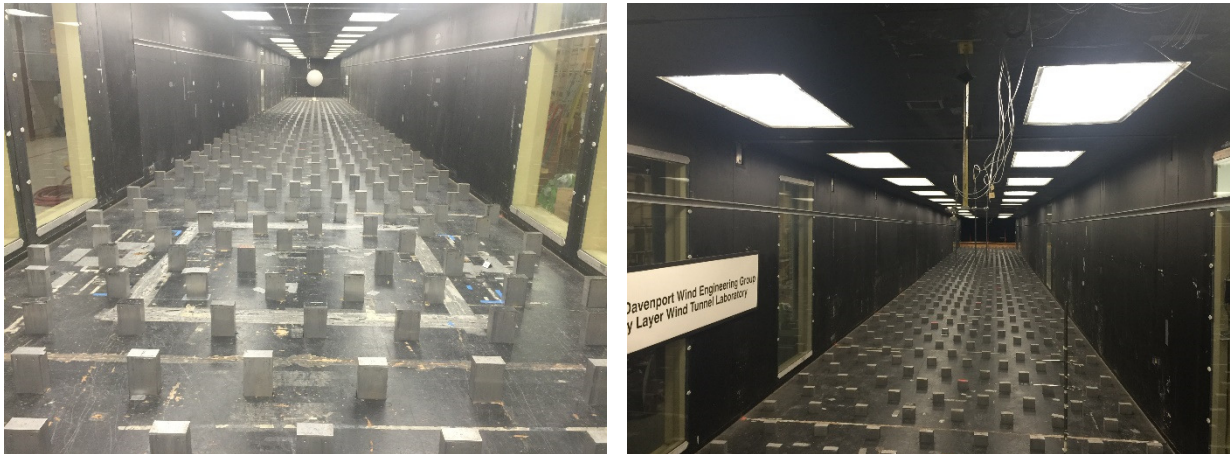


Figure 2.2: BLWTL interior views: a) roughness blocks; b) interior view of the tunnel with pitot tubes at the “gradient height.”

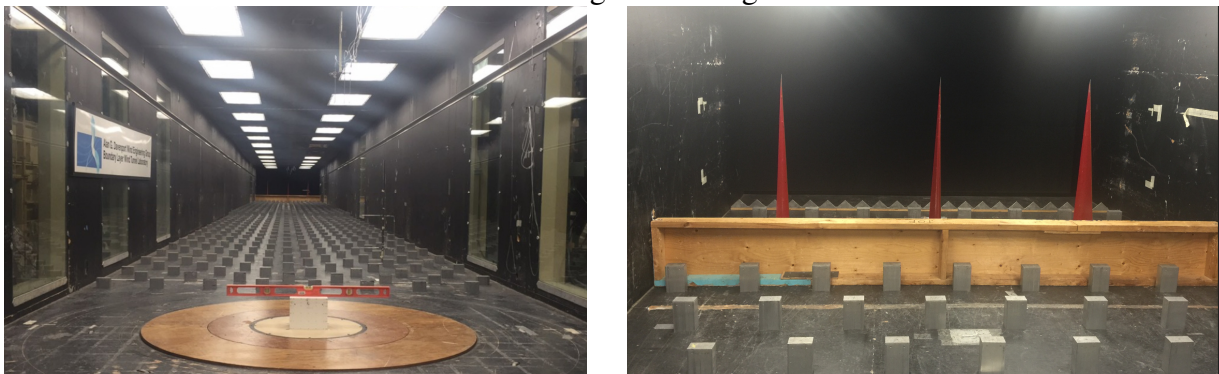


Figure 2.3: a) Typical test setup at BLWTL; b) Spires, roughness blocks and end barriers at BLWTL to generate turbulent wind flow

2.3 High-frequency pressure integration test

In this project, a high-frequency pressure integration (HFPI) test procedure was chosen to study the aerodynamics of mass-timber buildings and establish time history of wind loads. In this approach, as long as the aerodynamic replica is not changed, HFPI test gives the flexibility to perform design and analyze buildings with different construction materials, structural systems, and

functionality without test repetition. HFPI is one of the most widely used techniques to measure the positive and suction wind pressures on the surfaces of the rigid models. These models are an exact aerodynamic/shape replica of the full-scale buildings. Similitude analysis is necessary to determine the relationship between various geometric and time scales. The primary output of this type of test is the normalized pressure coefficient (C_p).

$$C_p = \frac{P - P_o}{\frac{1}{2} \rho_a V_{ref}^2} \quad 2.1$$

where P = pressure measured on the model surface; P_o = mean static pressure at reference height; ρ_a = density of air, and V_{ref} = mean wind speed at the height of the model.

The normalized C_p values can be converted to full-scale pressure coefficients using the velocity scale. For resultant force, bending moment, and torsional load calculations, the C_p values of Eq. 2.1 should be integrated over the tributary area of each pressure tap to obtain the corresponding force coefficients (C_f). Moreover, the results from HFPI will be augmented to the dynamic properties of the building in the post-test analysis to perform a performance assessment and determine the equivalent static design wind loads.

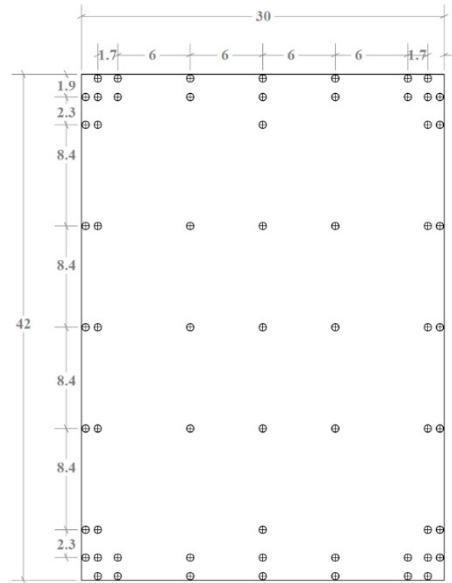
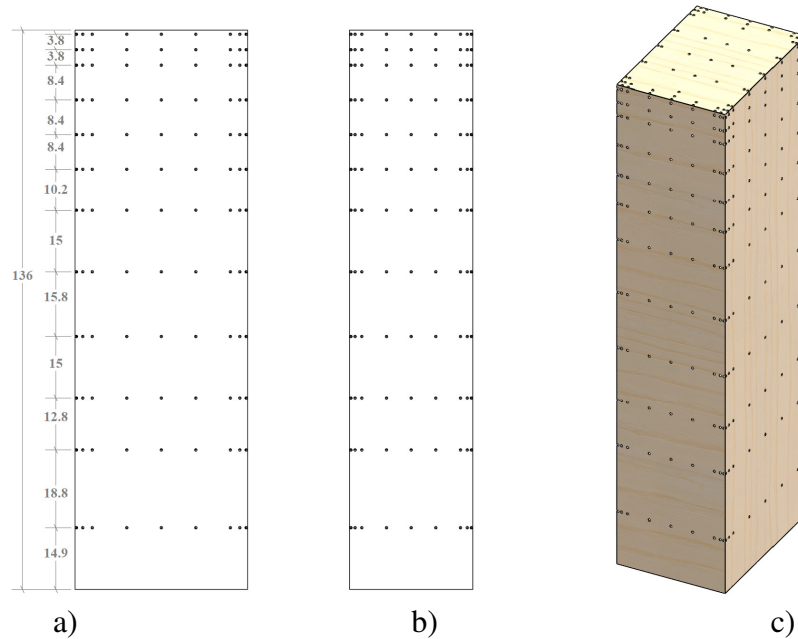
The accuracy of the measured spatial-temporal local pressure values depends on the resolution and location of the taps. Depending on the complexity of the surrounding, Dragoiescu et al. (2006) suggested the impact of the tap number and layout and in HFPI test. Traditionally, a large number of taps are used in the locations with the higher-pressure gradient. To reduce uncertainties related to pressure measurements, in this project, a computational fluid dynamics approach was used to design the spatial distribution of taps.

2.4 Building model descriptions

The wind tunnel tests were carried out on selected archetype building models of various building heights (10-, 15-, 20-, 30-, and 40-storeys) using a modular arrangement technique. The full-scale floor plan dimensions are 30m × 42m and floor-to-floor height is 3.4m. The details of the archetype selection process and models are given in the subsequent sections.

2.4.1 Tap layout design

The suggested tap layout of the test model is depicted in Figures 2.4 to 2.6. In the figures, the black dots represent the pressure taps. Figure 2.4 shows the roof pressure layout. The tap layout on the front and side elevations of the 40-storey hybrid building is presented in Figure 2.5. In Figure 2.6, all buildings considered for this test are depicted. Figure 2.5 shows five different heights having the same plan aspect ratio are tested using a modular approach. Similar taps layout is suggested for all sides of the building. In total 495 taps will be used to measure the pressure fluctuations.

**Figure 2.4:** Roof tap layout**Figure 2.5:** Pressure taps layout of the 40-storey building; a) Front view b) side view c) 3D view

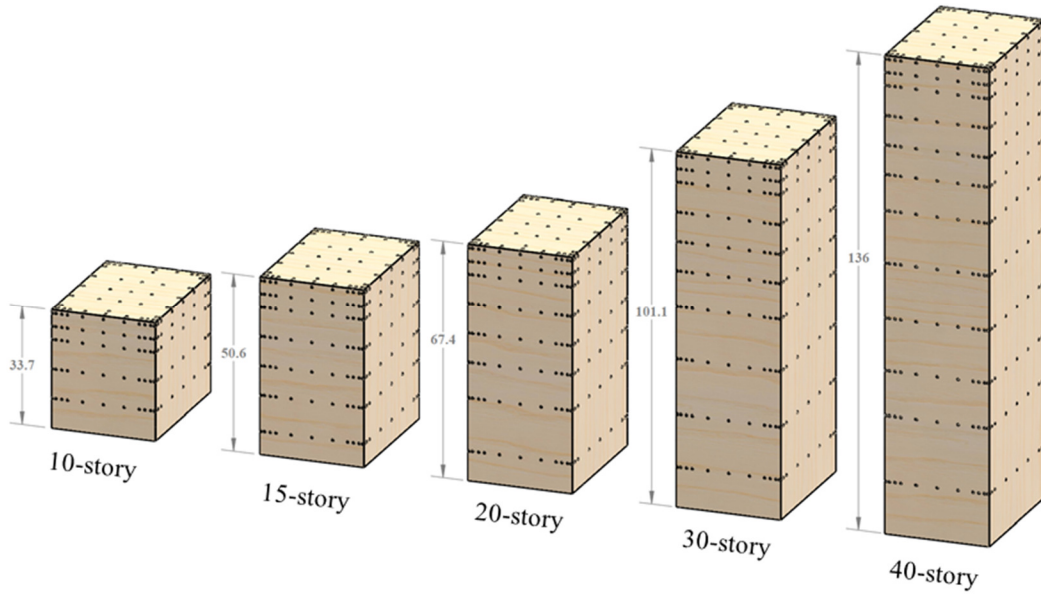


Figure 2.6: Various building heights considered for wind tunnel testing

2.4.2 Tributary areas for taps

In order to calculate the dynamic response of buildings due to wind loads, it is necessary to integrate the pressure time histories at each tap over its defined tributary area. Owing to the simplicity of the building shape and the regularity of the pressure taps layout, tributary areas were assigned easily by drawing a rectangular mesh around the tap. In this method, especially for the central taps, the right and left sides of the meshes are halfway between adjacent taps. The details of the tributary areas, meshing and floor height locations for 40-storey building are depicted in Figure 2.7.

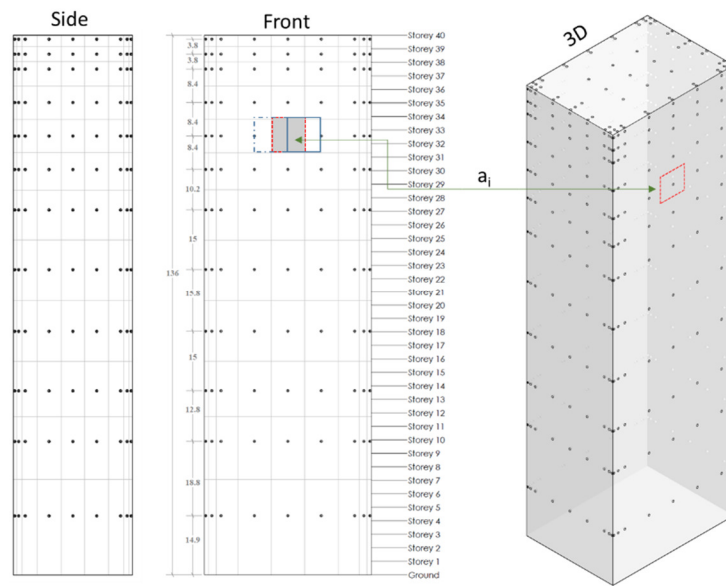


Figure 2.7: Tributary areas on the surface of the 40-storey model

2.4.3 Model manufacturing

The model drawing depicted in Figure 2.6 was submitted to the University Machine Service (UMS) of the Western University. UMS manufactured the rigid main model, the base plate, and adjustable steel tubes to perform wind tunnel testing in modular arrangement fashion. In this way, removing the modules in height will produce the required height while reducing the wind tunnel testing time and model fabrication cost. With the modular arrangement, part of the model will be buried under the turntable and strengthened with the provided steel tubes for tests lower storey tests. During manufacturing, several hundreds of pressure taps were installed on the surface of the models.

2.5 Experimental setup, instrumentation, and data acquisition

Several instruments were used to measure various flow and aerodynamic parameters. These include pressure transducers, pitot tubes, and cobra probes. In this sub-section, a summary of the instrumentations setup is provided. In HFPI, wind pressures and suctions are measured on the surfaces of the rigid models. During manufacturing, several hundreds of pressure taps were installed on the surface of the models. The first instrumentation process was to connect these tubes to the other end of pressure scanners. Each scanner consists of 16 ports, and a total of 32 scanners were used for this project. These scanners convert the measured pressure signals to an equivalent electrical signal, using the signal transduction process at a specified sampling rate. The generated electrical signals can be measured and interpreted using computerized data acquisition systems. Figure 2.8 shows the tallest rigid model and pressure measuring tubes and scanners.

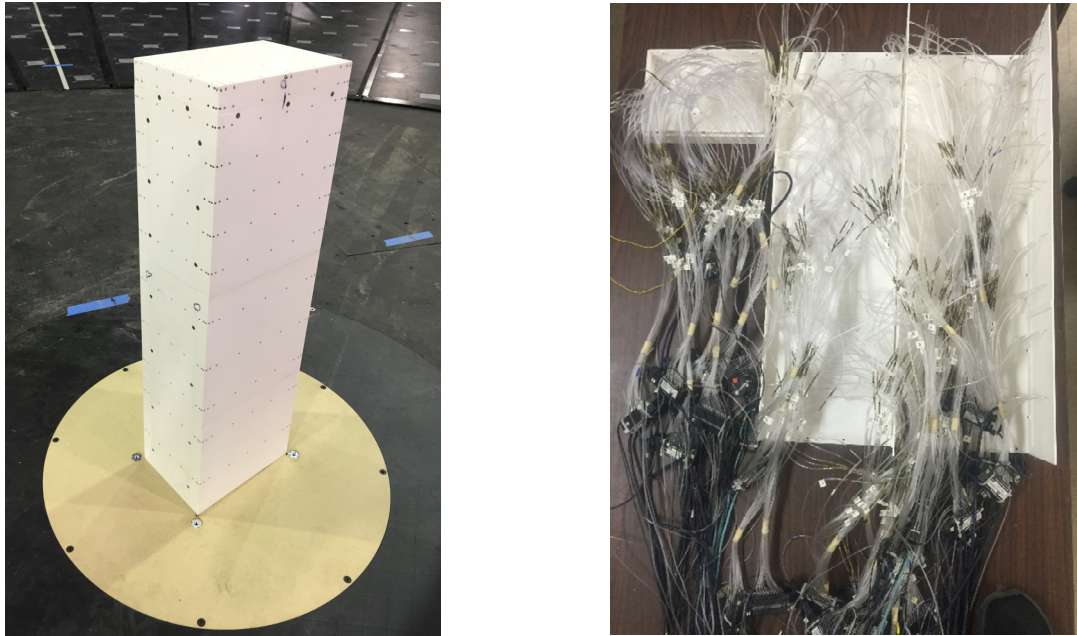


Figure 2.8: Rigid building model and instrumentations photo with pressure scanners

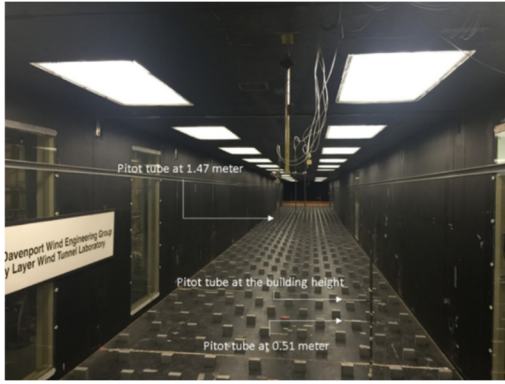


Figure 2.9: Arrangement of the pitot tubes inside the wind tunnel

Three Pitot tubes were placed to measure the time-varying dynamic pressure at building height for each test, 0.51 meters and at the gradient height (1.47 meters) (Figure 2.9). The Pitot tube at the gradient height and 0.51 meter are stationary whereas the height of the first Pitot tube varied with building height. The dynamic pressure data from these instruments will be used to calculate the pressure coefficients. Moreover, to measure the three components of velocity (U_x , U_y , U_z) and turbulence intensities (I_x , I_y , I_z) a cobra-probes were installed at the height of the building during each test.

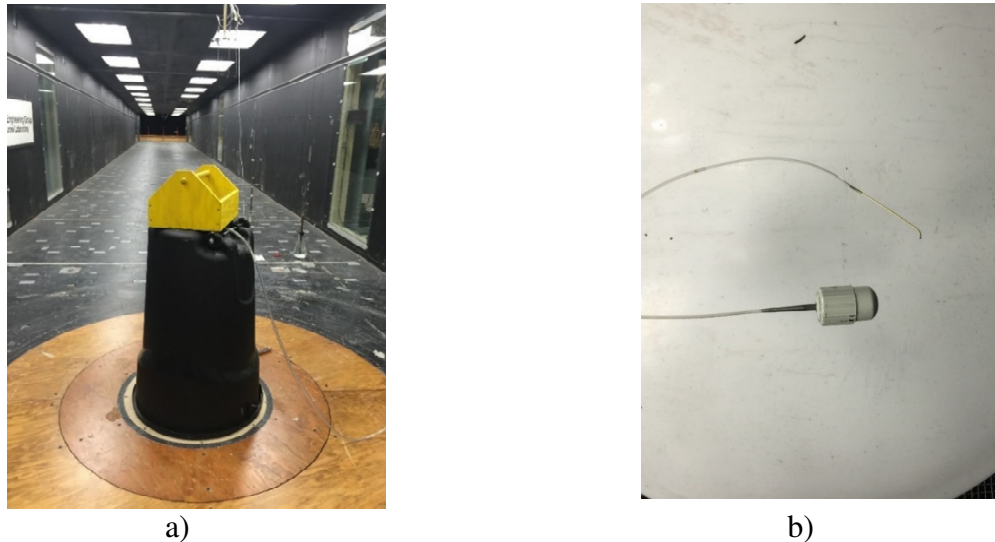


Figure 2.10: a) Bug test on the model; b) Puffer to check the pressure taps

BLWTL is equipped with National Instruments data acquisition (NIDA) to collect, control, arrange, and transfer the digitized signals from each instrument. When the instrumentation setups were finalized, two pre-tests checks were carried out, i.e., puff and bug tests. The purpose of the puff test was to check the performance of taps by manually applying pressures at each tap. In this way, it is easier to identify if there is a blockage. The second test is a bug test and was carried out to check the air tightness of the models. A constant amount of pressure was applied by covering

the building with an airtight plastic bag to check if the model is sealed acceptably. A snapshot of the bug test process and the puffer for the puff test are depicted in Figure 2.10.

After the instrumentation, data accusation setups, bug and puff tests, the models were tested under boundary layer turbulent wind flow. The test setups for 10-, 15-, 20-, 30-, and 40-storeys are shown in Figure 2.11. Table 2.1 summarizes the wind tunnel test parameters.

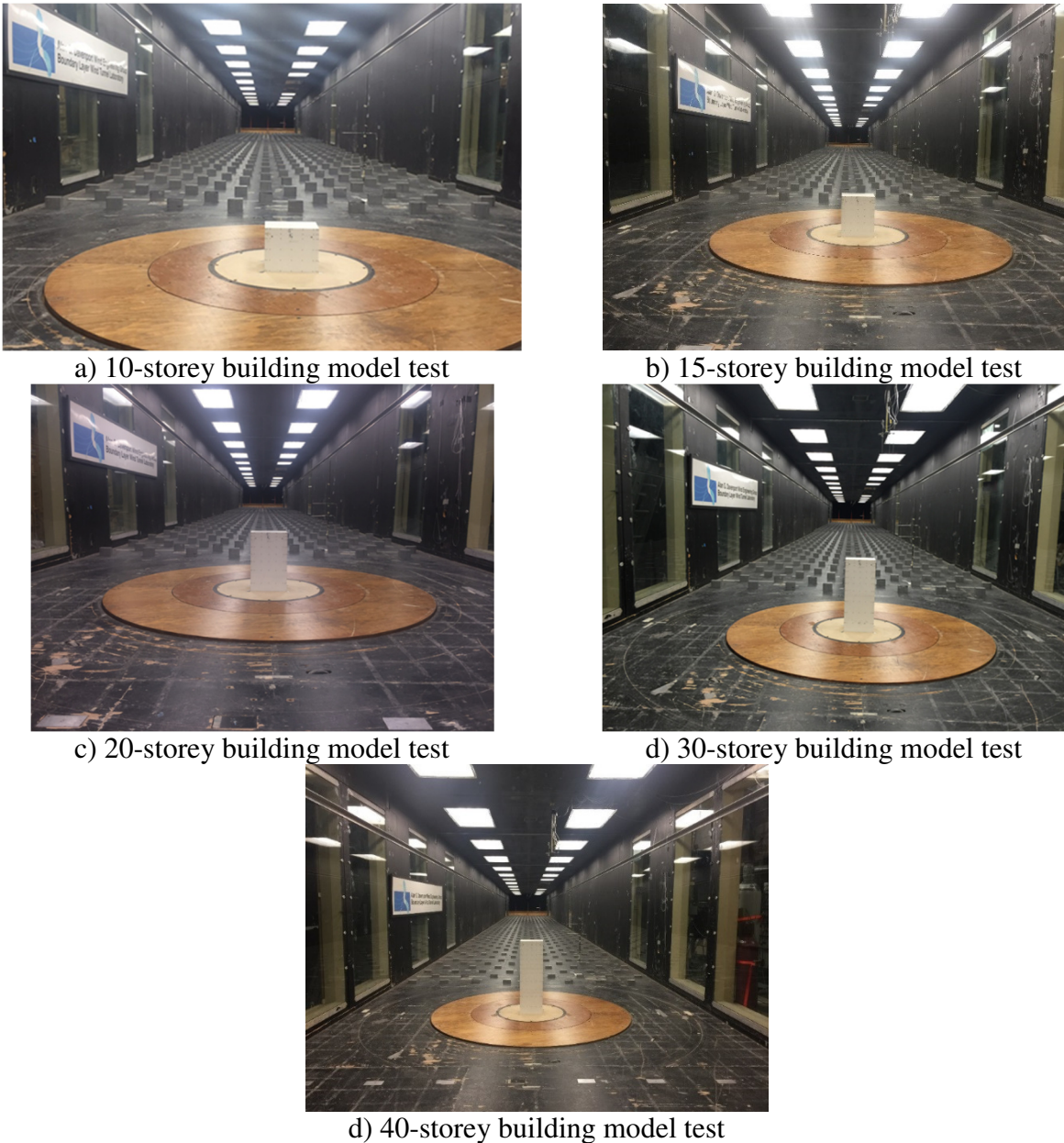


Figure 2.11: Boundary layer wind tunnel tests on the hybrid tall mass-timber building models at BLWTL

Table 2.1: Parameters of wind tunnel testing

Facility	BLWTL
Test type	High-Frequency Pressure Integration
Building heights (full-scale)	34m, 51m, 68m, 102m, 136m
Geometric scale	1:200
Test duration	2 mins
Number of taps	495 for 40 storey building
Exposure condition	Open terrain
Wind angle of attack interval	10°
Sampling frequency	400 HZ

2.6 Wind tunnel tests

This section presents the results of the wind tunnel tests. The models were tested by simulating open terrain atmospheric boundary layer flow. Measurements were taken for different wind angles of attack in 10° increments. An in-depth statistical analysis was performed to obtain and study the mean, root-mean-square, peak, correlation, and auto-covariance of the measure pressure fluctuations.

2.6.1 Boundary layer wind field simulation

A boundary layer flow corresponding to an open country terrain condition at 1:200 geometric scale was simulated inside the wind tunnel by using both passive and active control systems. Without the test model, for the purpose of calibration, cobra-probe was installed to measure the fluctuating velocity components and turbulence intensities at the model location (center of the turntable). As shown in Figure 2.12a, the profiles of mean wind velocity and longitudinal turbulence intensity are compared with the ESDU (1974) provisions. A good agreement is obtained between the ESDU (1974) profile and the measured mean velocity up to the full-scale height of 51 cm. Moreover, the power spectral density of longitudinal wind velocity time series recorded at 51 cm is plotted and compared with the ESDU (1974) provision as shown in Figure 2.12b. As shown in both figures, a good agreement is obtained both in the mean wind speed profiles and turbulence intensities. This indicates the capability of BLWTL to perform accurate aerodynamic tests of the study building models in 1:200 geometric (length) scale.

2.6.2 Experimental results

Five models having the same plan aspect ratio but differing in height were tested using the boundary layer flow profile of Figure 2.12. Simultaneous time series of pressure fluctuations were measured using the installed taps on the models. For each model, the wind angle of attack increases from 0° to 180° at 10° increment. Pressure fluctuations were digitized at the rate of 0.0025 sec (400 samples/sec). In this section, the results of selected models under critical wind angles of attack are presented for illustration purpose. The obtained results will be used to perform time history

structural analysis of full-scale buildings. For this purpose, the time series pressure fluctuations must be converted to non-dimensional pressure coefficients that vary in both space and time. Eq. 2.2 was used to calculate the time series of pressure coefficients. Average dynamic pressure (q_p) at the building height was used to normalize the measured pressure readings.

$$C_p = \frac{P(x, y, z, t) - P_o}{\frac{1}{T} \int_0^T q_p dt} \quad 2.2$$

where $P(x, y, z, t)$ = pressure reading on the surface of the aerodynamic model at time (t) using a tap located at (x, y, z) from the origin (center of the roof), P_o = static pressure, T = test duration, and q_p = dynamic pressure measured at the height of the building using the Pitot tube.

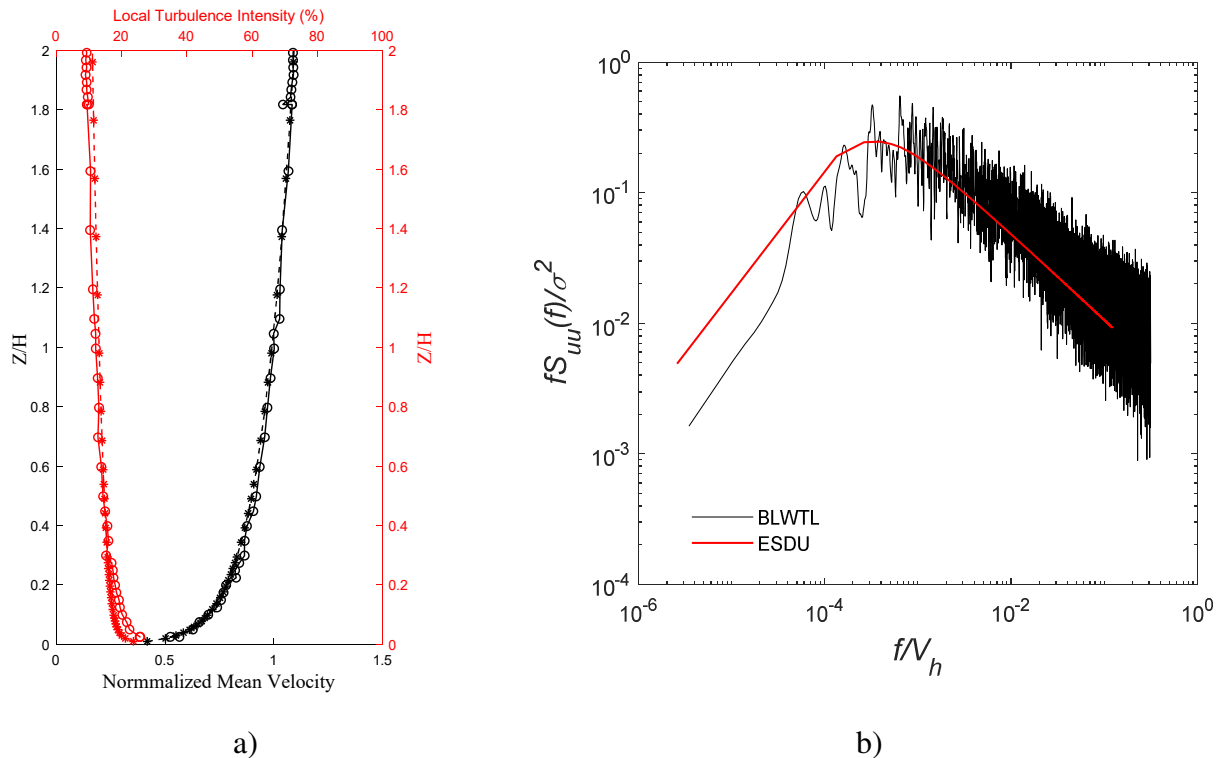


Figure 2.12: Comparison of simulated exposures with ESDU (1974) a) mean wind speed and turbulence intensity profiles; b) longitudinal wind spectra at 51 cm

For illustration purpose, few time histories of C_p results from the 0° test on the 40-storey building model for selected taps (Figure 2.13) are presented in Figure 2.14 and Figure 2.15. The pressure time series in Figure 2.14 show the chord-wise variation of C_p values. The C_p time series plot on Figure 2.14 are for pressure taps #1, #2, and #3 on the windward wall; taps #4, #5, and #6 on the side wall; and taps #7, #8, and #9 on the leeward wall. Figure 2.15 shows the variation of the C_p time series over the height of the building. The considered pressure taps in Figure 2.15 are #21, #1, #31, #41 at the edge of the windward face and taps #22, #2, #32, #42 at the front center of the windward face of the model.

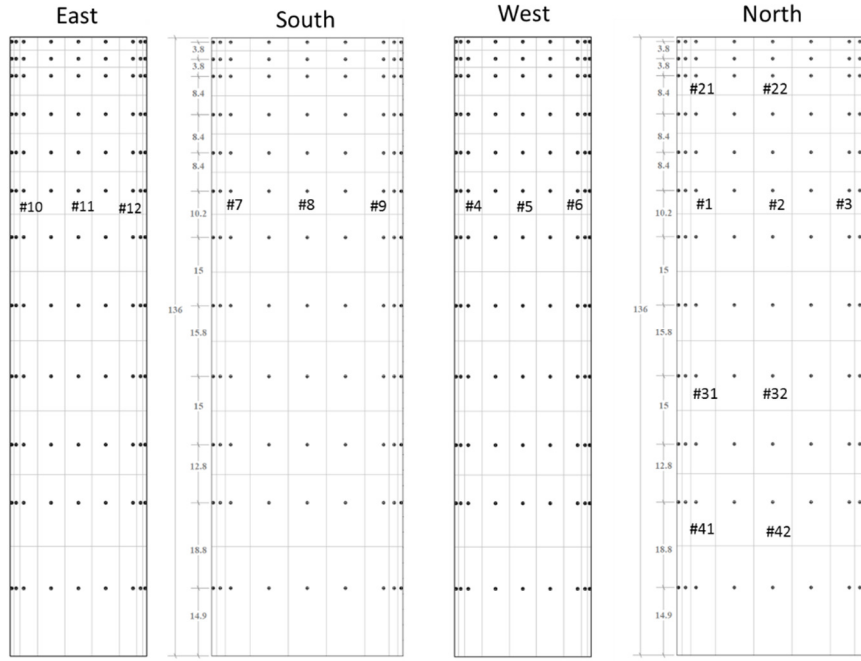


Figure 2.13: Pressure taps location on 40-storey building model

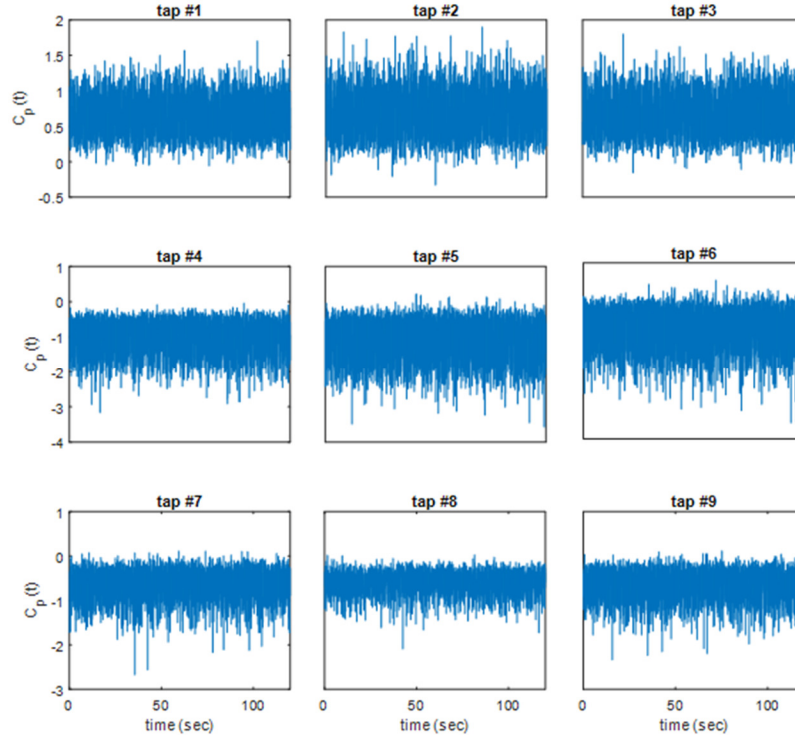


Figure 2.14: Chord-wise C_p time series variation on the 40-storey building model for the 0° angle of attack

As can be seen from Figure 2.14, the pressure taps on the windward face (#1, #2, #3) recorded positive C_p values. The recorded time series on these taps shows symmetry about the mean and the process can be considered as Gaussian. Pressure taps on the leeward and side walls recorded suction (negative pressures). Sharp pressure spikes are also observed in the time series plot. Especially edge pressure taps located in suction and wake zones (around the flow separation

points) recorded time series with multiple sharp spikes without symmetry about the mean. This indicates that the probability distribution of pressure coefficients in these regions might be non-Gaussian in nature.

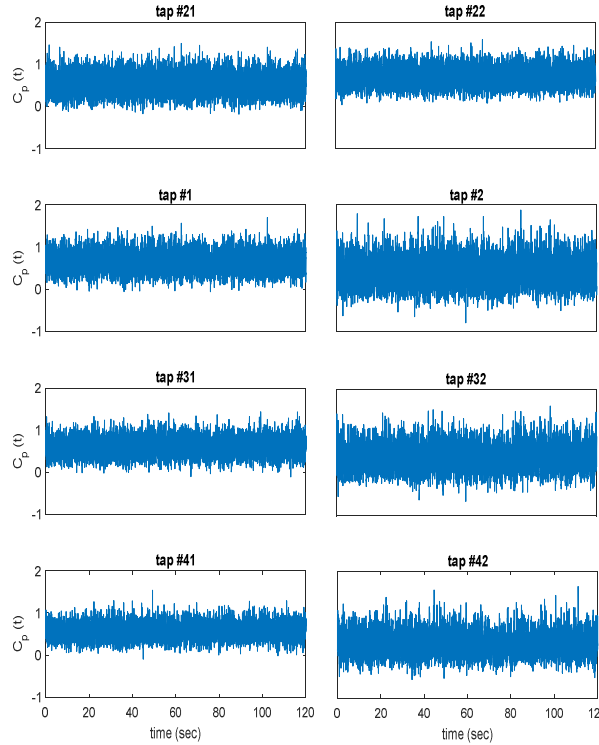


Figure 2.15: Height-wise C_p time series variations on the 40-storey building model for the 0° angle of attack

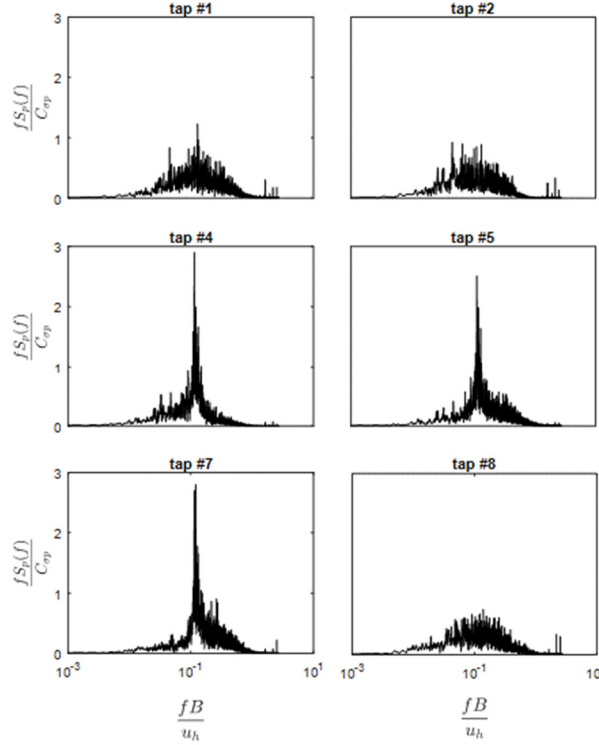


Figure 2.16: Reduced spectra plot of pressure fluctuations for selected pressure taps

Moreover, the spectral plots of the pressure time series on the side walls are dominated by vortex shedding with spectra peaks at Strouhal number ~ 0.1 as depicted in Figure 2.16. This process is a typical narrowband process characterized by a concentrated turbulent energy at a single frequency. The reduced spectral peak smaller for the pressure taps away from the leading edge. The spectral plot from the pressure tap on the leeward face is broader with a defined spectral peak. However, the spectral peak decreases significantly for tap #8. An increase in the energy content is observed at the higher frequency range after the reduced cut-off frequency = 0.15.

2.6.3 Statistics of pressure coefficients

In this section, the first four statistical moments (mean, root-mean square (rms), skewness, and kurtosis) and peak of the pressure coefficients measured over the surface of the 30-storey building model are presented. Figure 2.17 show the mean contour plots over the exterior surface of the 30-storey building when AOA = 0°. The figure depicts that, the windward (northern) wall is under positive pressure with a stagnation point around 70% of its height. However, all the other sides are under suction (negative pressure). The east and west walls (side walls) show symmetric pressure coefficient distribution. Figure 2.18 presents rms C_p distribution. The maximum rms over the front wall of the building is around 0.25. In order to check whether the probability distribution of surface pressure coefficients is Gaussian or not, we quantified the kurtosis and skewness of the obtained C_p values and plotted as contours in Figure 2.19 and Figure 2.20. Suresh Kumar and Stathopoulos (1998) suggested a margin to between a Gaussian and non-Gaussian pressure wind fields. According to their study, a wind pressure field can be called non-Gaussian if skewness and kurtosis, in absolute term, greater than 0.5 and 3.5, respectively. From this study, it can be concluded that, both the separated flow regions (side walls) and wake region should be modeled as non-Gaussian pressure field and the C_p over the front wall can be considered as Gaussian.

Mainly used for cladding element design, in this section we quantified the peak C_p values using a standard signal translation process (Sadek and Simiu 2002). Both Gamma and Gaussian probability distribution types were used as a parent probability distribution of the measured pressure signals. Extreme value I (Gumbel) distribution was used to characterize the probability of the peaks. The obtained peak pressure coefficients over the surface of the 30-storey building model are shown in Figure 2.21.

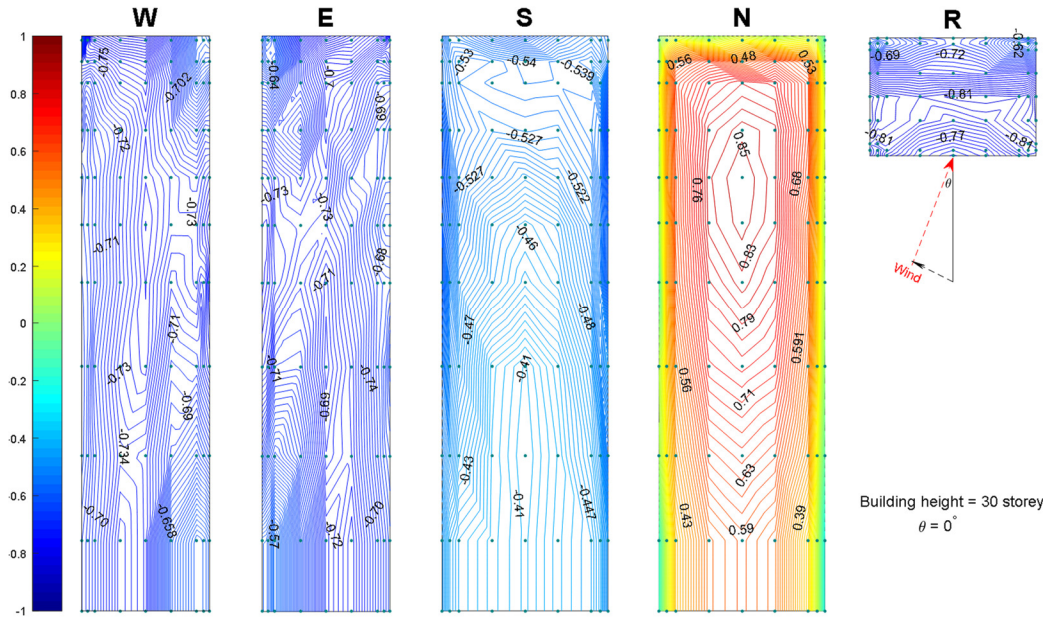


Figure 2.17: Contour plots of mean C_p for 30-storey building for AOA = 0°

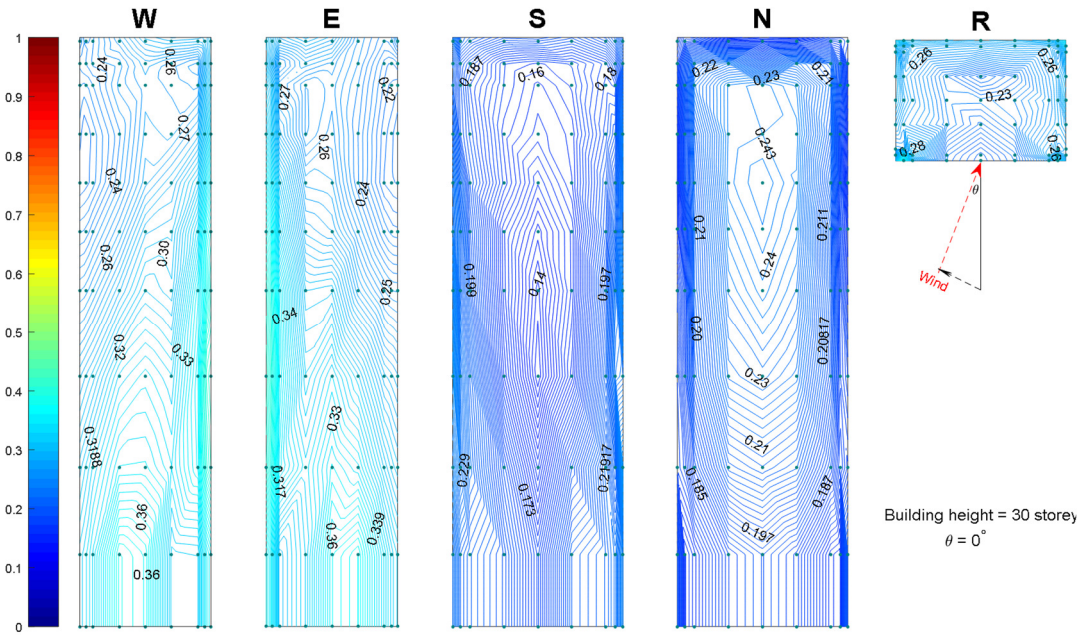


Figure 2.18: Contour plots of rms C_p for 30-storey building for AOA = 0°

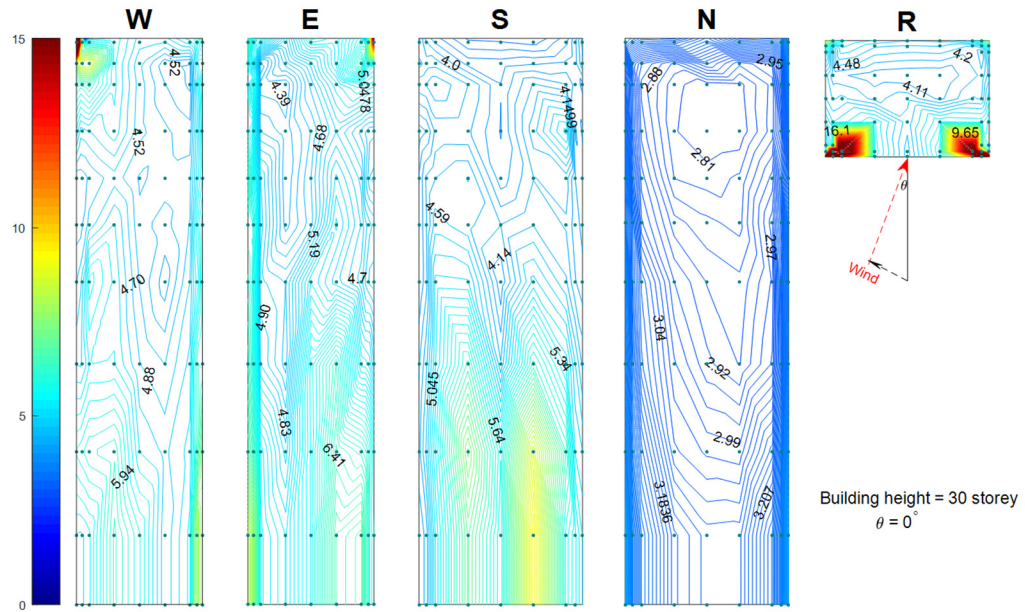


Figure 2.19: Contour plots of kurtosis C_p for 30-storey building for AOA = 0°

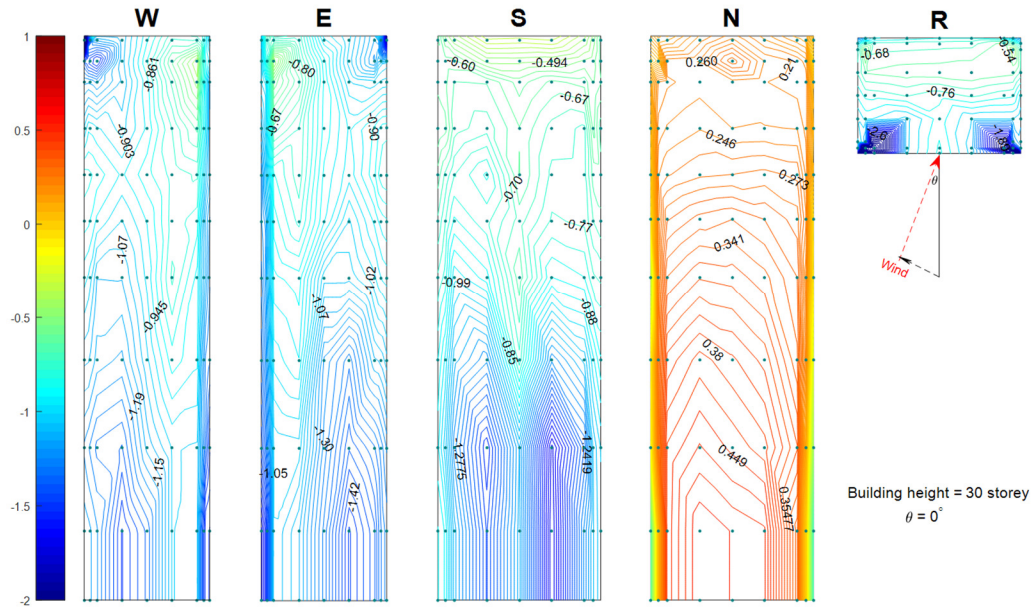


Figure 2.20: Contour plots of skewness C_p for 30-storey building for AOA = 0°

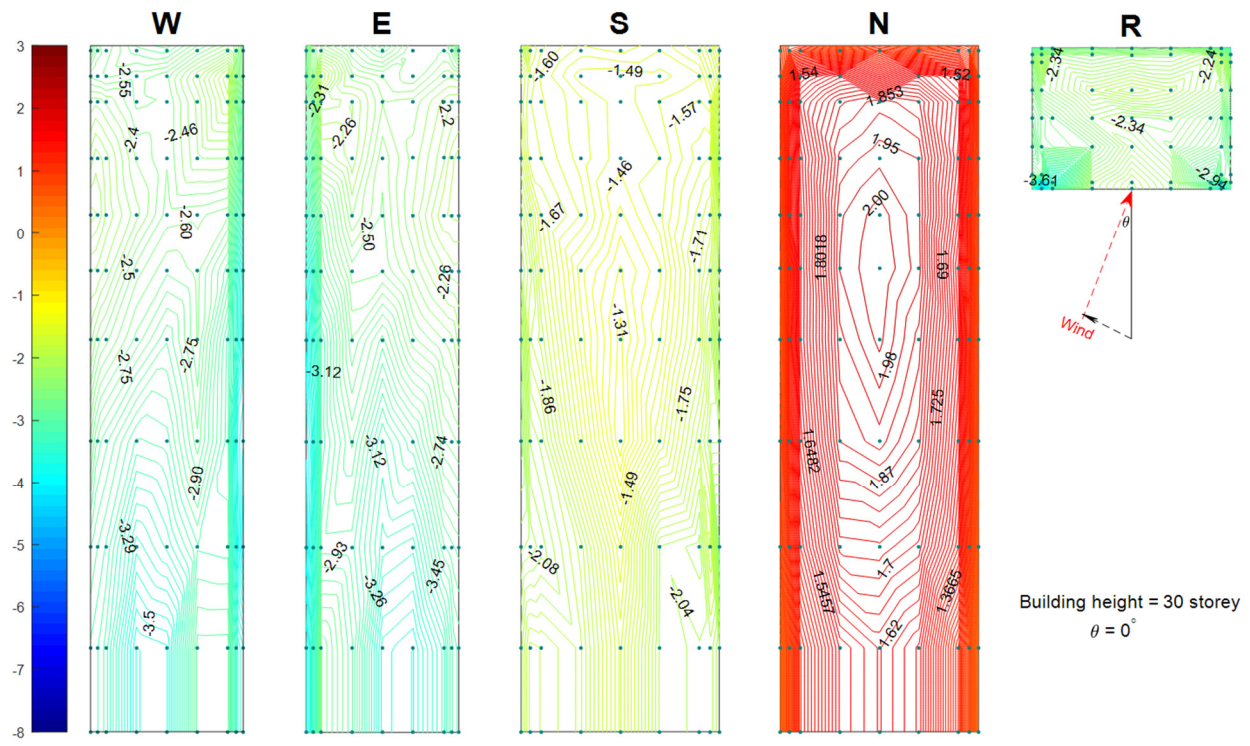


Figure 2.21: Contour plots of peak C_p for 30-storey building for AOA = 0°

Chapter 3

Wind-induced Response and Serviceability- Performance Assessment of Tall Mass-timber Buildings

This chapter presents the structural design process, wind-induced response evaluation, and serviceability performance assessment of tall of wood buildings. The chapter also provides guidelines to perform probabilistic modeling, reliability assessment, and wind load factor calibration.

3.1 Description of the studied case study mass-timber buildings

In this project, the conceptual structural system of timber-tower project that was introduced by SOM (2013) is adopted. The main reasons for selecting the SOM's timber tower system are:

- 1) the building is regular both in plan and elevation, which will allow us to compare our aerodynamic and wind response results with the provisions from building codes;
- 2) the timber tower project (SOM 2013) is developed based on an existing benchmark reinforced concrete building, which will permits us to compare the performance and dynamic properties of tall wood buildings with buildings made from conventional constructional materials; and
- 3) the details of architectural design of the building are available for public. In this project, we adopted the plan dimension and the structural system of timber tower project (SOM 2013). However, targeting the high-end condominium application, the floor-to-floor height is changed to 3.4m.

To study the effect of height and building flexibility, we considered 10- (34m), 20- (68m), 30- (102m), and 40- (136m) storey tall-wood buildings. The buildings have floor plan dimensions of $30\text{m} \times 42\text{m}$. Heavy timber products such as Glulam columns and CLT panels are used to construct both the gravity and LLRS of the buildings. Figure 3.1 show a typical floor and 3D views of the case study buildings. As shown in the figure, the shear walls and floor systems are made from CLT panels. Concrete link beams are used to couple the movements of CLT shear and core walls, resulting in a global "H" shaped LLRS. In addition to the two coupled CLT core walls, four single CLT shear walls provide uplift resistance due to the wind load from the wider face of the building.

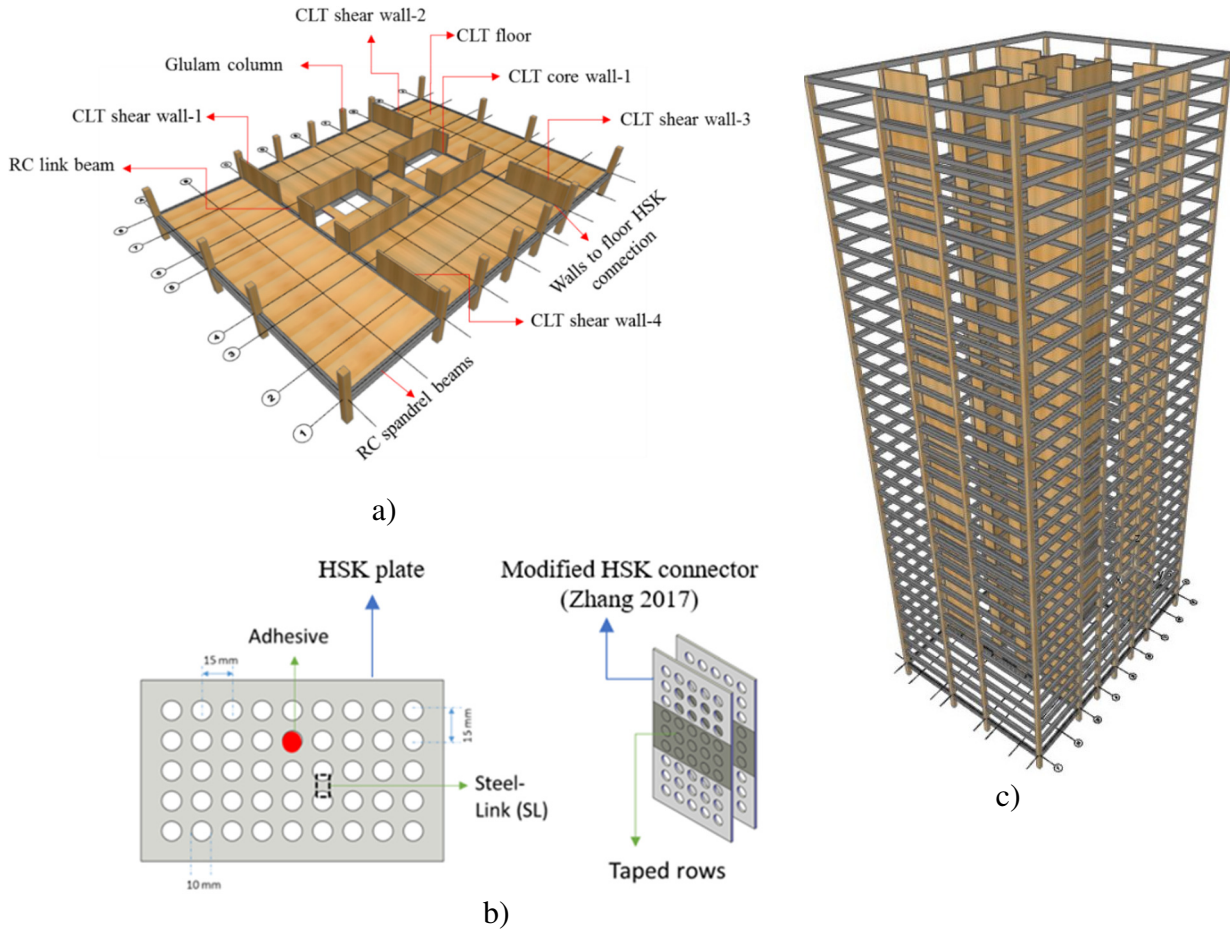


Figure 3.1: a) Typical floor plan of the case study buildings, b) HSK connector, c) 3D view of 30-storey mass timber building without floor

Glulam columns are only used at the perimeter of the building to increase the gravity load share of the interior CLT shear and core walls (Figure 3.1). The absence of interior columns increases the uplift resistance of the CLT shear and core walls. However, this strategy requires larger span floor systems. Therefore end-rotation restraint is provided by concrete spandrel perimeter beams to which could increase the floor deflection demands. Concrete elements are extended from the RC link beams to the end spandrel beams to act as a concrete joint. A modified Holz-Stahl-Komposit (HSK) system (Zhang 2017) is used to connect the CLT walls and floors systems to the concrete joints (Figure 3.1). The modified HSK system can be used as shear connector to resist storey level wind forces and hold-down connector to resist net uplift forces.

3.2 Structural design of the tall-mass timber building

The structural design of the case study buildings is carried out using the dead, live, and 50-year wind loads from NBCC (2015) provisions and design wind speed maps. The buildings are assumed to be in Toronto, Ontario. We used both the worst-gravity and worst-wind load combinations rules

of NBCC (2015) to provide adequate strength against extreme wind loads. In the following subsections, summary of the structural design process of the buildings is presented. The following are the critical steps that we followed to provide adequate resistance against wind and gravity loads.

3.2.1 Design of gravity load resisting system

Design of CLT floor usually governed by the out-of-plane bending moment demand from gravity loads or vibration control requirements. The out-of-plane bending strength of CLT floors in major strength direction and vibration demands were calculated using provisions from the updated CSAO86 (CSA 2014). We selected CLT floor based on specifications given in Structurlam (2016) design catalogue.

Another important component of gravity system is perimeter Glulam column. They are mainly designed to resist the total axial load demand from gravity loads. We calculated the parallel to the grain axial capacity of Glulam columns using provisions from the CSAO86 (CSA 2014). For this purpose, we adopted material and section properties from Structurlam (2016) design catalogue. The design process considered elastic buckling and size effects of the Glulam columns. Design iterations are performed to make variation of column size over the height of the building.

3.2.2 Design of lateral load resisting systems

The resistance to the lateral wind loads generally involves a chain load transfer from the building envelope to floor diaphragm then to coupled action of CLT shear and core walls and finally to the foundations. In general, even if wind design of building only considers the linear-elastic capacity of structural systems, at the ultimate limit state, it is expected that three stages of progressive failure mechanisms happen sequentially. First, when the specified wind load reaches the factored resistance, inelastic rotation and damage are expected to occur on the RC link beams. Subsequently, the HSK connectors will yield and damage. Finally, wood crushing could happen at the corners of the CLT walls. It is to be noted that, in this chapter, the wind load in Toronto governs the final design and wind serviceability requirements dictates the stiffness requirements of the building. Therefore, the design of LLRS is only performed for wind and gravity loads; however, for the designs in Vancouver the next chapters of this report will show the details of the seismic design.

The design of CLT walls considers the axial compression, in-plane-shear, and in-plane and out-of-plane bending moment demands. The absence of the interior columns increases the axial load demand of the shear walls, which could make the axial load a critical design demand. Hence, for all case study buildings, we conservatively estimated the initial sections of the LLSRS using the

axial load demand. Once the sections of CLT walls are identified, we checked their in-plane shear capacity against the wind induced demands. For this purpose, the in-plane shear resistance of CLT walls reported in the CLT design manual (Structurlam 2016) are adopted. Subsequently, for each single CLT shear and core wall, coupled axial load and out-of-plane moment demand were estimated and checked from the load carrying capacity and buckling resistance perspectives. The adequacy of the CLT walls was checked using the CSAO86 interaction equation (CSA 2014). This design process is iterative until satisfactory CLT shear wall thickness is achieved. The details of the design procedure are presented in the following subsections.

CLT core walls are used to provide lateral resistance to both along and across-wind loads. During wind storm, the central core walls experience high tensile and compressive stresses at their leeward and windward side corners, respectively. The maximum corner compressive stress on the leeward side of the core walls could be governing for the design of the CLT core walls. Therefore, all the core walls of the case study buildings are checked against failure due to crushing of walls due to excessive compressive stress. Details of the design equations can be found in Bezabeh et al. (2018a).

3.2.3 Design of modified HSK connectors

In this chapter, the modified HSK system (Zhang 2017) is used and designed as shear connectors and hold-downs to effectively transfer the wind loads from the shear walls to the foundations. In HSK system by few rows of the holes on the steel plates inside the wood failure of the connection system is expected to occur inside the CLT shear walls. It is found that the connection strength and ductility were governed by the capacity of the “Steel Links (SL)” between the holes on the steel plates inside the CLT element (Figure 3.1c). We considered the statistical average resistance of shear connectors and hold-downs reported in Zhang (2017). Due to the higher gravity load demands on the shear walls, during the design of hold downs, we followed a safe but conservative design approach

3.2.4 Design of RC link beams and spandrel beams

As mentioned earlier, the CLT shear and core walls are coupled using RC link beams. It is expected that the weight of the buildings increases due to the use of these beams. In the design process, we initially checked if diagonal reinforcements are needed. Therefore, the shear stress in the link beams was initially checked using the provisions of CSA A23.2-14 (CSA 2014) shear stress limit. Based on the calculations, irrespective of the height of the building, the link beams do not need diagonal reinforcement and can be designed as flexural beams. Therefore, for all case study

buildings, beams were sized to resist the maximum shear force demand transferred from the CLT walls and the flexural moment demands using design provisions of CSA A23.3-14 (CSA 2014).

All the case study buildings are designed following the above procedures. The details of the design calculations and final specifications of CLT shear, Glulam columns, RC link beams, CLT core walls, and CLT floor systems of each building are reported in the companion report of this study.

3.3 Modal analysis

To compute the dynamic properties of the case study buildings, eigenvalue (modal) analysis is performed. Figure 3.2 shows the mode shapes and building frequencies of the first three modes of the case study 40-storey mass-timber building. Since only buildings with frequency of vibration less than 1Hz are considered as dynamically active under wind loads, in this project, only the four first three modes are included in all wind response analyses. As can be seen in the figure, the first two modes are in translation, while the third mode is dominated by torsion. It is worth mentioning that, in contrast to reinforced concrete (RC) buildings, tall mass-timber buildings are lighter and more flexible.

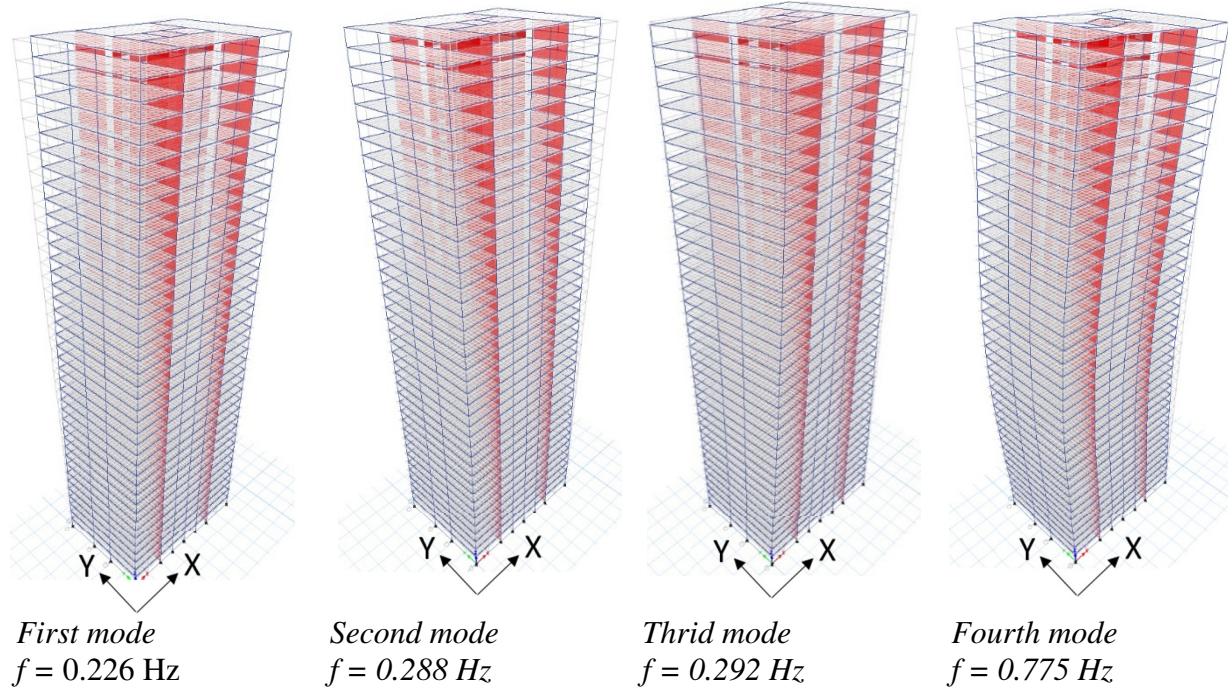
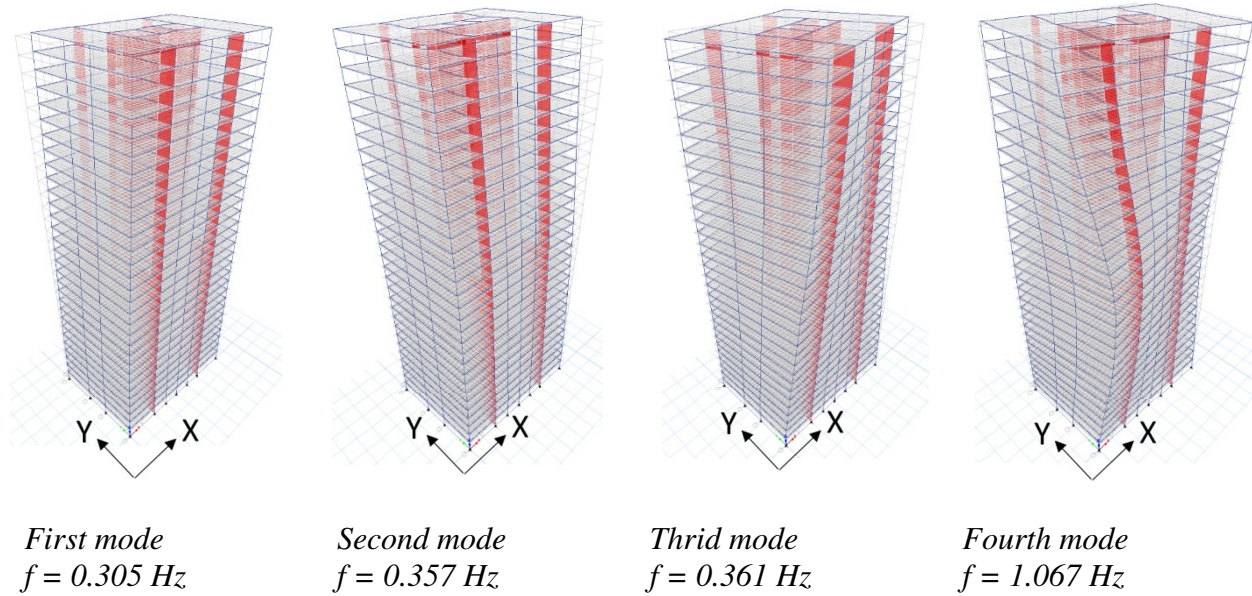
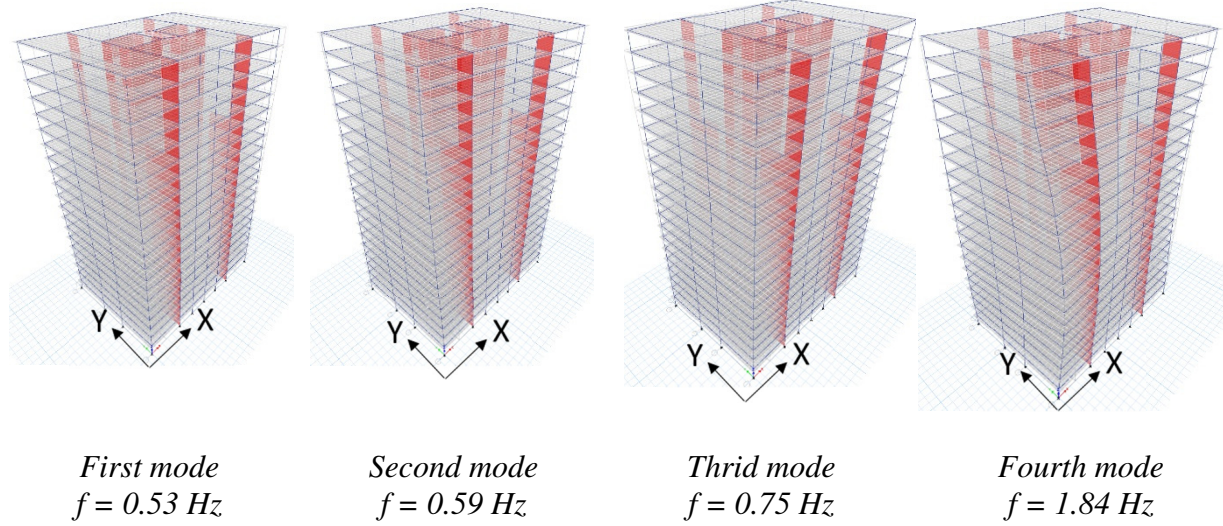
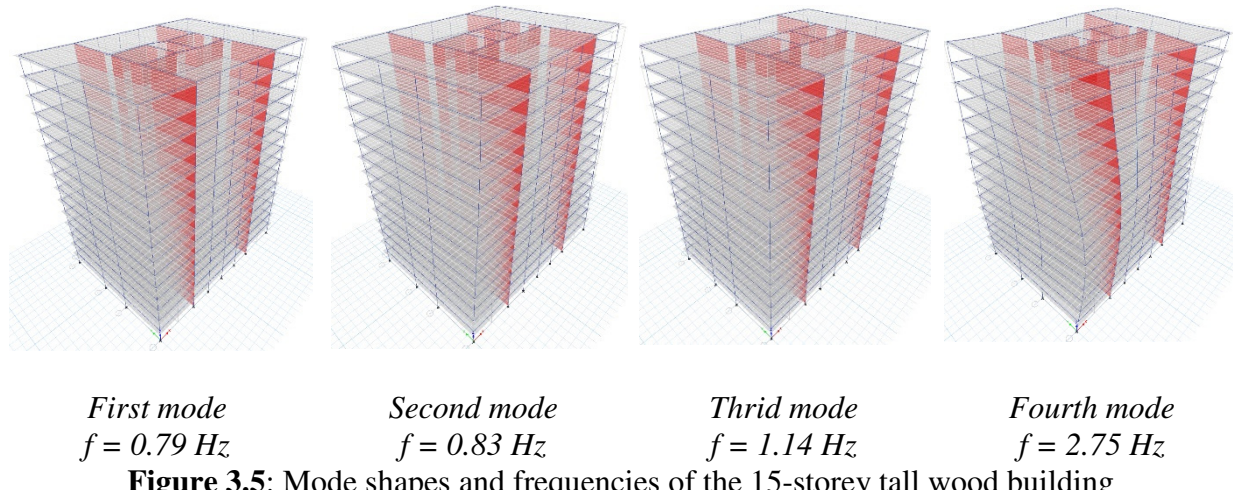


Figure 3.2: Mode shapes and frequencies of the 40-storey tall wood building

**Figure 3.3:** Mode shapes and frequencies of the 30-storey tall wood building**Figure 3.4:** Mode shapes and frequencies of the 20-storey tall wood building**Figure 3.5:** Mode shapes and frequencies of the 15-storey tall wood building

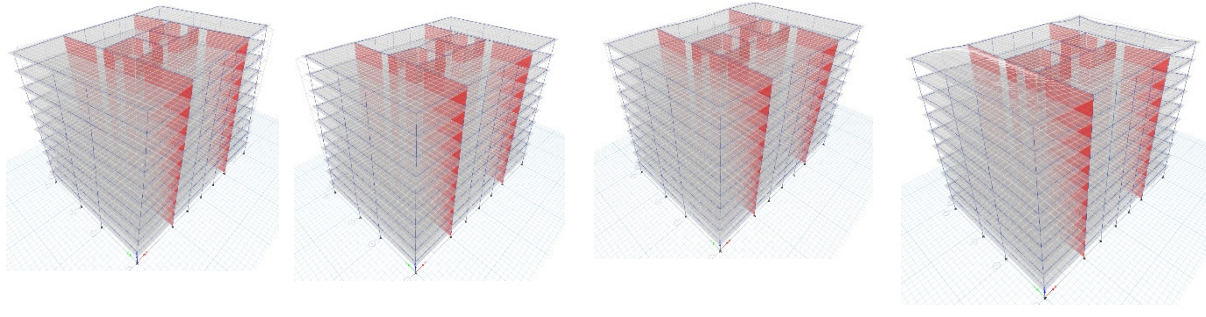


Figure 3.6: Mode shapes and frequencies of the 10-storey tall wood building

3.4 Dynamic structural analysis

Tall buildings under dynamic wind loads experience responses in the along-, across-, and torsional directions. The along-wind aerodynamic load is primarily caused by the instantaneous pressure fluctuations in the windward and leeward faces of the building, while across-wind loads are primarily due to vortex shedding. Torsional wind loads in tall buildings are due to the instantaneous asymmetry of fluctuating pressure distributions on all sides the building walls. To illustrate the nature of the obtained aerodynamic wind loads, we present the along-, across-, and torsional normalized spectra at various levels (9th, 18th, and 26th stories) of the 30-storey building. Note that the presented results are for open country exposure condition. As shown in the figure, both the along-wind and across spectra are not sensitive to height. As expected, for, the across-wind spectra featured a sharp peak at the Strouhal number = ~0.1.

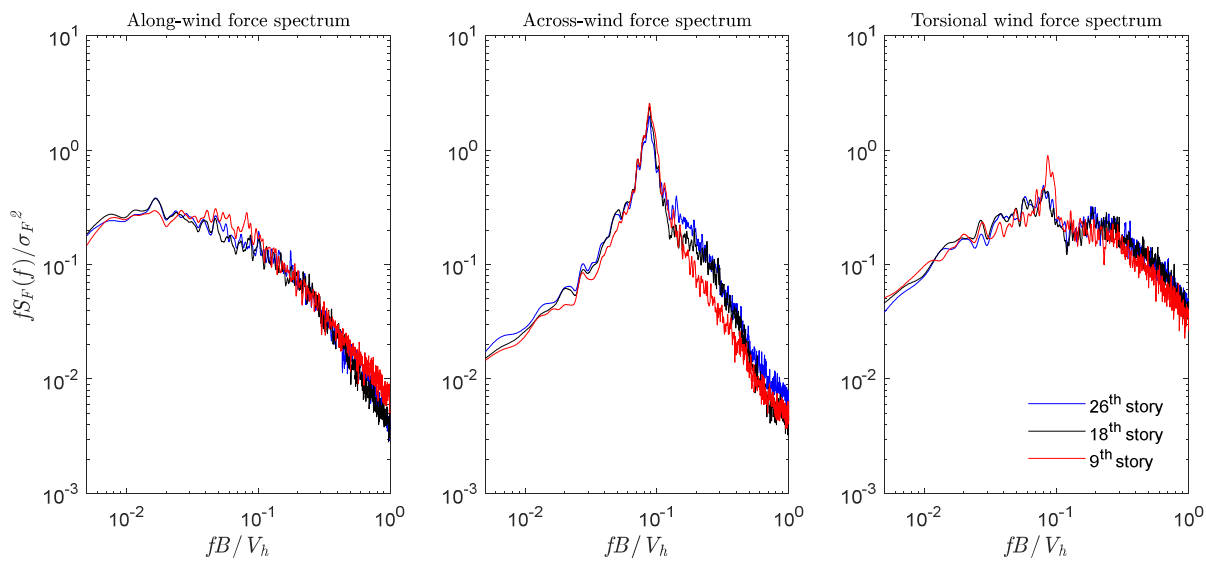


Figure 3.7: Variation of spectra for open country exposure condition (Bezabeh et al. 2018a)

The Newmark's Beta method is used to directly solve the equation of motion and obtain the response of the tall wood buildings subjected to dynamic wind loads. The displacement responses from the analysis are converted to other response parameters (shear force, bending moment, acceleration) using the modal participation factors and modal combination rules proposed by Chen and Kareem (2005). The overall predicted design shear forces contain mean, background and resonant components. The mean and background components of the design wind loads are obtained by integrating the surface pressures of the building from the aerodynamic wind tunnel test data. The resonance component is mainly due to the turbulent wind energy at the fundamental frequency of the buildings, which depends on the building's dynamic properties. A critical damping ratio of 1% is used in the calculation of the resonant component of the responses. In Bezabeh et al. (2018b), the effects of damping uncertainties are discussed within the probabilistic performance-based wind engineering framework. Readers are referred to Bezabeh et al. (2018a, b, c) for details of analysis methods, performance assessment, and reliability estimations. Although the results presented in the following sections are very brief, the details of random vibration theory, formulations, and the entire dynamic analysis results are included in Bezabeh et al. (2018a, b, c).

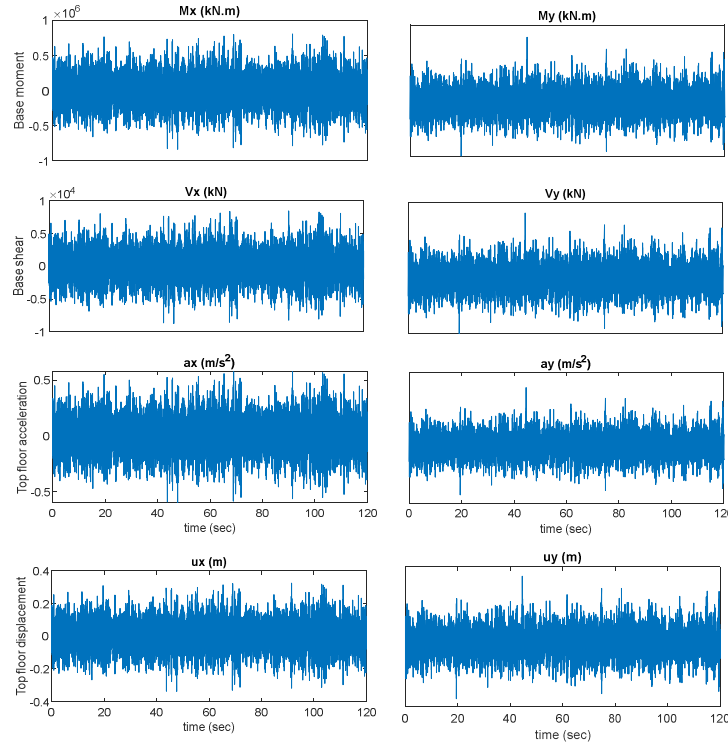


Figure 3.8: Time history response of 40-storey tall mass-timber building when AOA = 0°

When subjected to wind loads, structures with fundamental frequency less than 1 Hz responds dynamically with a significant contribution from resonance phenomena (Merrick and Bitsuamlak (2009). Therefore, the performance assessment in this chapter will only consider case study

buildings taller than 15-storey. Figure 3.8-Figure 3.11 show the time history of structural responses (base moment, base shear, top acceleration, top floor displacement) of all the case study buildings. From the plots, the responses of 40-storey are five times larger than the 10-storey building. Moreover, the recorded time histories at the base and top floors show some symmetry about the mean and look Gaussian. It should be noted that design revisions can be carried out by calculating the peak static wind loads from the presented time histories. This can be easily done using the peak factor approach reported in Davenport (1964).

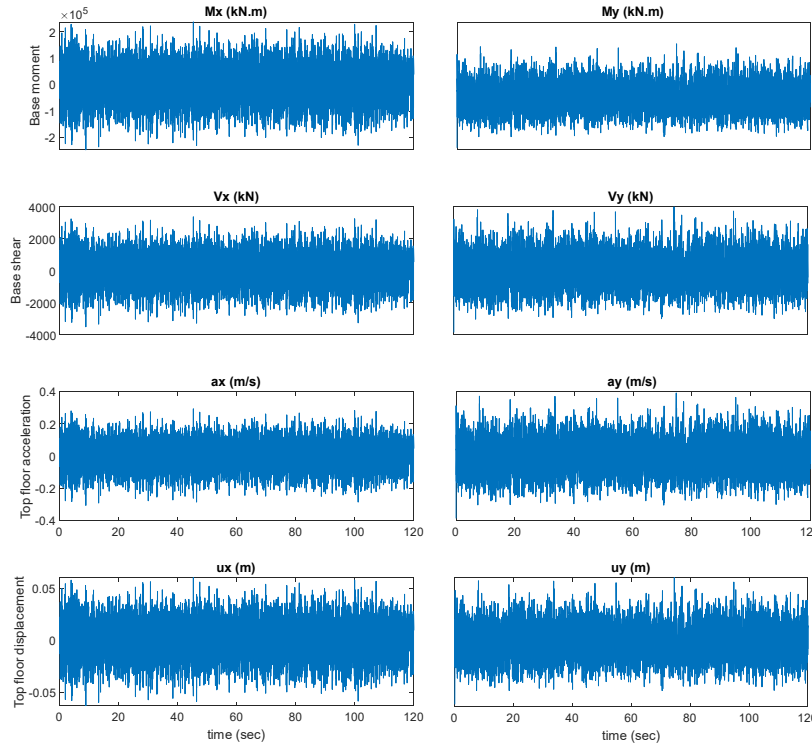


Figure 3.9: Time history response of 30-storey tall mass-timber building when $\text{AOA} = 0^\circ$

The time histories clearly show the dependence of response parameters on building height. As expected, the responses of 10- and 15-storey buildings are mainly due to the mean and background components of the wind loads; very little contribution from the resonance component. It should be noted that the presented time histories are due to the wind load approaching perpendicular to the wider face of the buildings ($\text{AOA} = 0^\circ$). Bezabeh et al. (2018a) shows that the critical wind angle of attack for a 30-storey mass-timber model with similar shape and dynamic properties is 0° . However, site-specific wind studies need to consider the variation of wind speed with directionality. In this research project, we assumed that the 10-year wind speed of city of Toronto comes in all directions with equal probability.

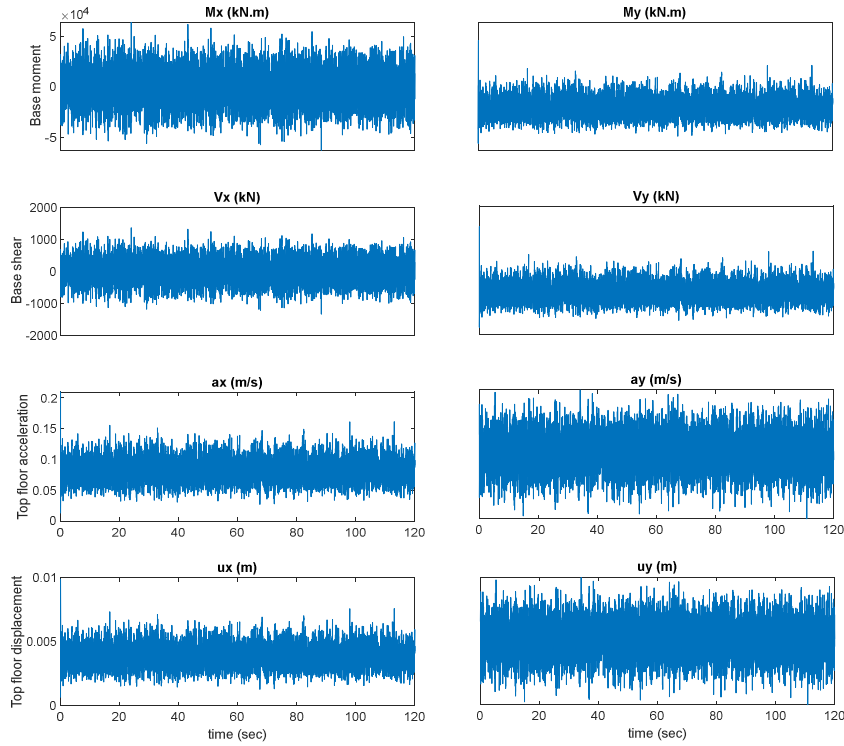


Figure 3.10: Time history response of 20-storey tall mass-timber building when AOA = 0°

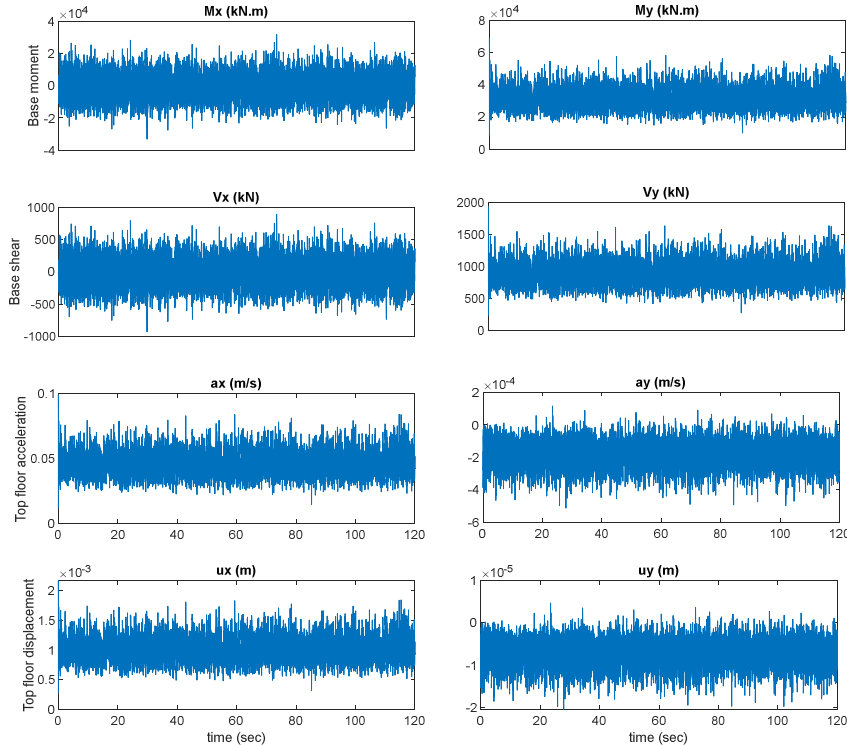


Figure 3.11: Time history response of 15-storey tall mass-timber building when AOA = 0°

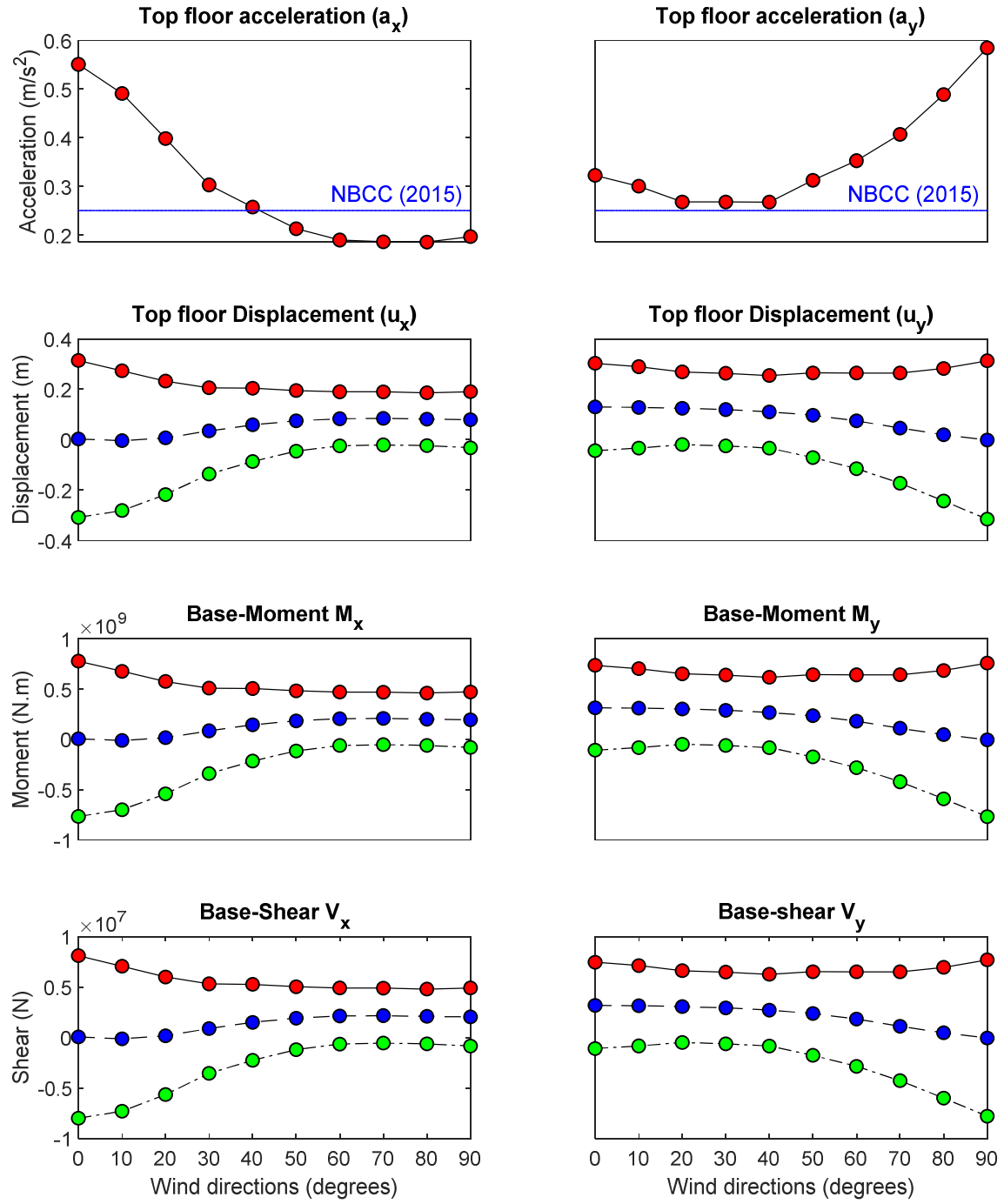


Figure 3.12: Structural response of 40-storey tall mass-timber building for various wind AOA

Figure 3.12 to Figure 3.15 show the maximum, mean, and minimum structural response for various wind angle of attack. Figure 3.12 shows the structural response of 40-storey tall-mass timber building for various wind angle of attack. As shown in the figure, the building does not satisfy the peak floor acceleration criteria of the NBCC (2015). Therefore, either passive or active supplemental damping systems are needed to reduce the peak floor acceleration of the 40-storey

building. Other response interests such as top floor peak displacement, base shear, are base moment found to be direction dependent. Similar conclusions were made for tall buildings in Warsido and Bitsuamlak (2015). The 0° and 90° AOA are the critical directions that should be considered to revise the design of the building. It worth also mentioning that 40-storey building exceeds the ($H/500$) limit of the NBCC (2015) criteria. Therefore, we recommend using either “wind bracing” or use concrete core walls to enhance the stiffness of the building.

Figure 3.13 shows the structural responses of the 30-storey tall mass-timber building. As depicted in the figure, the building satisfies the serviceability criteria of NBCC (2015) with a small safety margin. The base shear and moment responses are an order of magnitude less than the response of the 40-storey building. Additionally, the distribution of shear and moment responses with the wind angle of attack between the 40- and 30-storey buildings is quite different. This might be due to the significant variation of mode shapes and fundamental frequencies of the buildings. As expected the peak floor acceleration response of the 20- and 30-storey buildings is less than 25 milli-g (NBCC 2015). All the studied buildings except the 40-storey buildings satisfy the serviceability criteria of NBCC (2015). Therefore, from this project, it can be concluded that tall-wood buildings exceeding the height of 90 meters either need supplemental damping or “Wind bracing” through different hybridization techniques to satisfy the serviceability criteria of the 2015 NBCC.

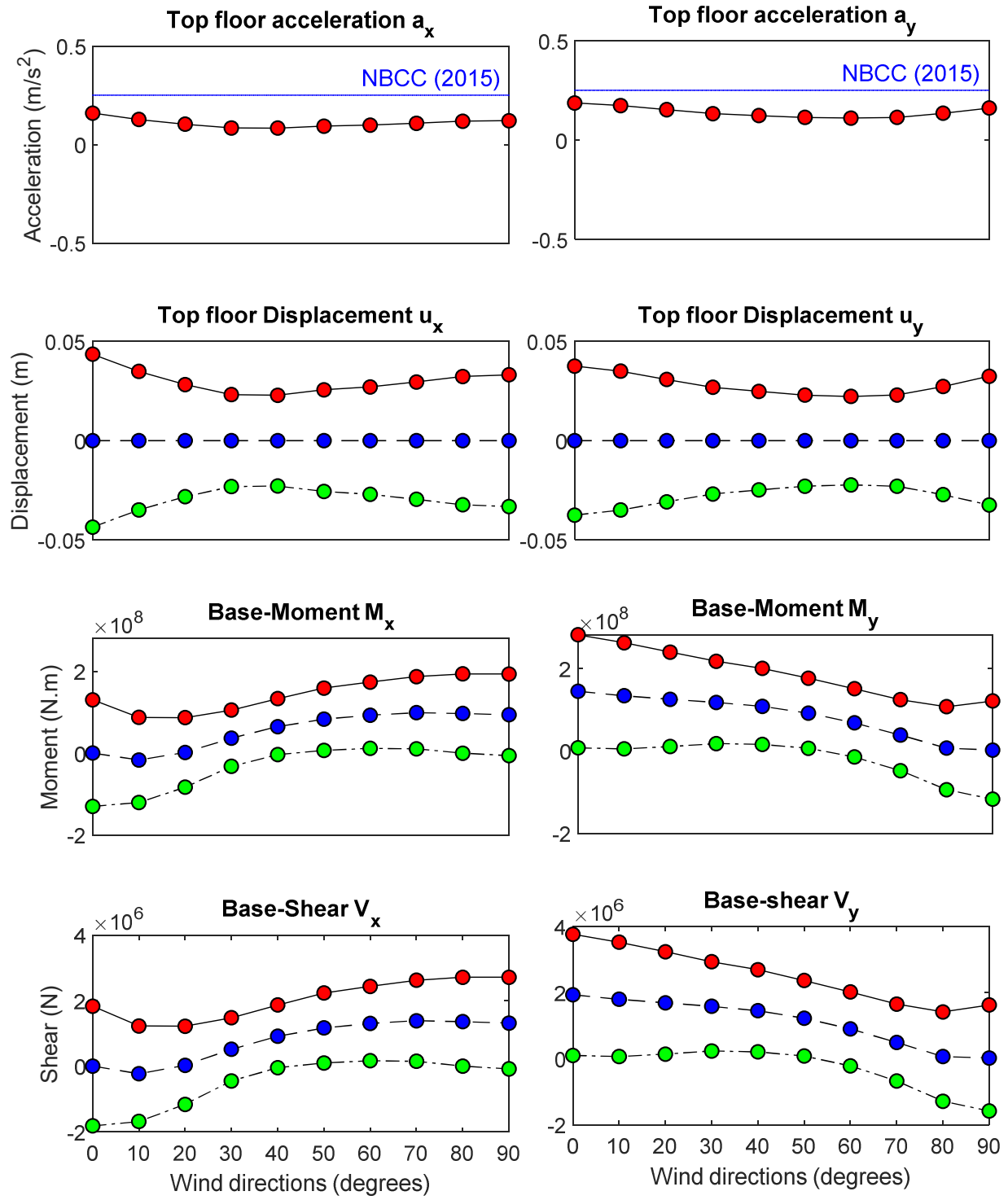


Figure 3.13: Structural response of 30-storey tall mass-timber building for various wind AOA

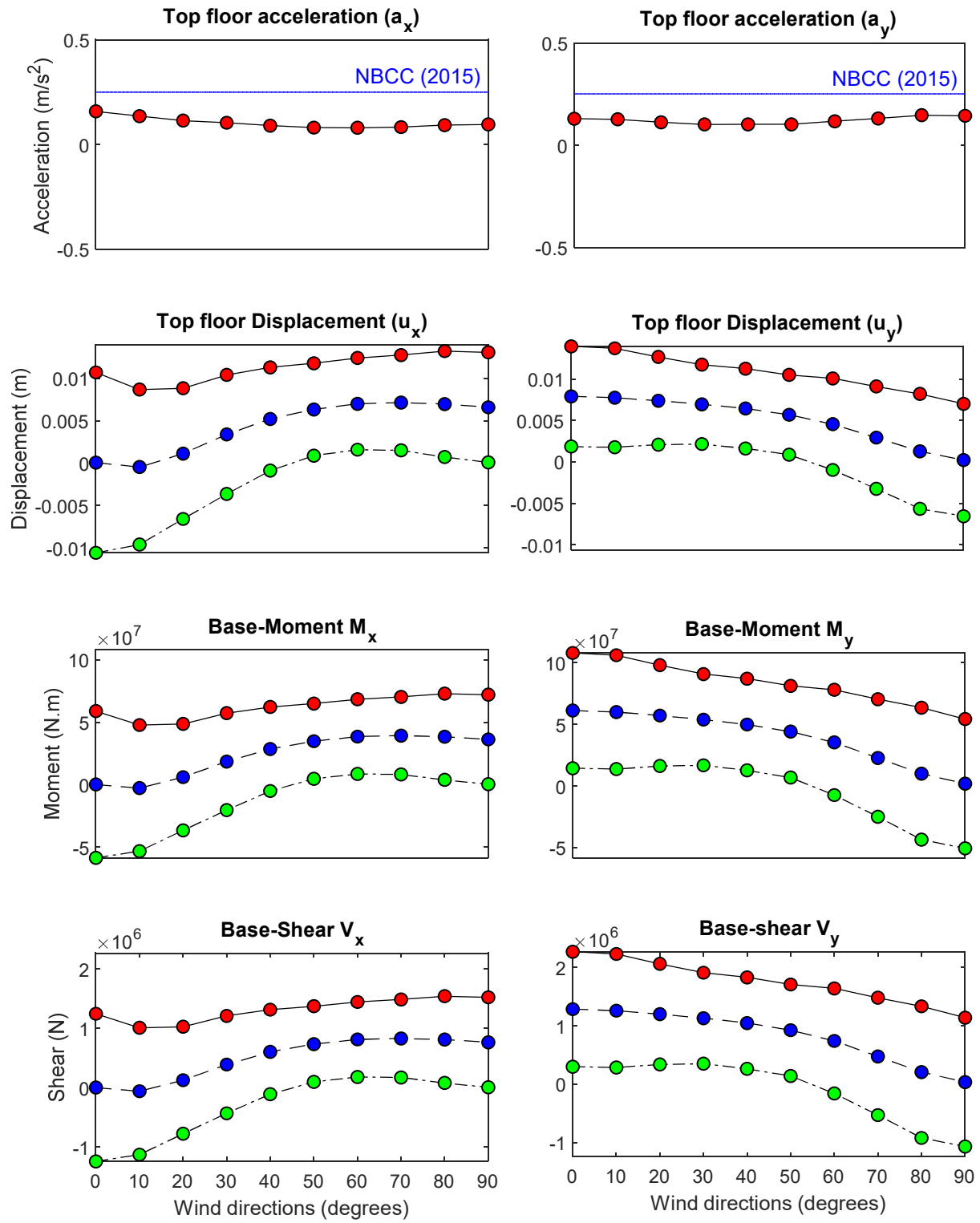


Figure 3.14: Structural response of 20-storey tall mass-timber building for various wind AOA

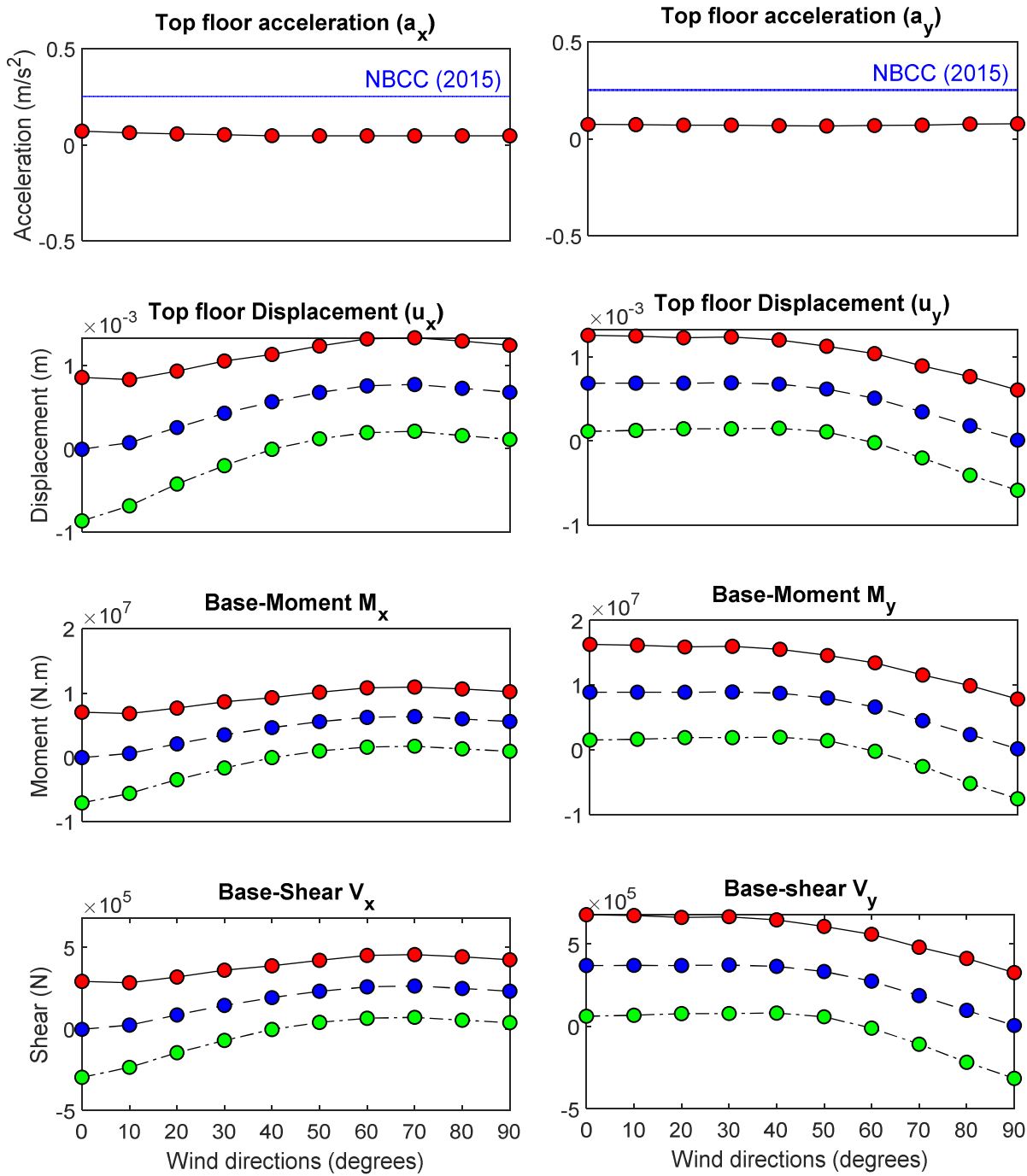


Figure 3.15: Structural response of 15-storey tall mass-timber building for various wind AOA

3.5 Preliminary load factor for serviceability design of tall mass-timber buildings

As shown in the previous sections, wood buildings taller than 20 storeys are extremely sensitive to wind-induced motions. For an assumed critical damping ratio of 1%, the 40-storey (136 meters tall) case study tall wood building did not meet the habitability criteria, and the 30-storey building satisfies the same criteria with a small safety margin. This finding implies that serviceability

criteria than ultimate strength requirements could govern the design of tall wood buildings. The 2010 edition of NBCC to perform ultimate limit state design of buildings for wind is:

$$(1.25D + 0.9D) + 1.4W + 0.5(L + S) \quad 3.1$$

where D = dead load, W = wind load, L = live load, and S = snow load.

Apart from the seismic load, the load factors in NBCC 2015 are calibrated for a target reliability index ($\beta = 3$) and life span of 50 years (Bartlett et al. 2003, Hong et al. 2010). As can be inferred from the above equation, the design wind load factor is 1.4. Considering the coefficient of variation of wind load effects ($v_w = 0.21$) and $\beta = 3$, Davenport (1983) also found the design wind load factor with the presence of dead load as 1.4. In the U.S.A., Bashor and Kareem (2009) investigated the applicability of the design wind load factor of ASCE 7-05 for flexible buildings considering uncertainties in fundamental frequency, damping, wind loads, and criteria. The authors found that the appropriate load factor to design tall and flexible building is 1.9 as opposed to the 1.6 factor suggested in ASCE 7-05. In this section, we first investigate the adequacy of the current wind load factor of NBCC 2015 for the 30-storey case study mass-timber building. Subsequently, considering the primary sources of uncertainties, we will determine the appropriate load factor considering drift as a performance indicator.

Davenport (1983) studied the relationship between structural reliability and wind loads. In the study, it was indicated that the errors in wind load effects (L) and structural capacity (R) are mainly due to multiplicative effects. Therefore, both L and R can be modeled as lognormal variates. Owing to this simplification, the probability of failure calculation (P_f) can be carried out using First Order Second Moment (FOSM) approach. The P_f and β can be obtained using the FOSM as:

$$P_f = P \left[\ln \left(\frac{R}{L} \right) \right] < 0 \quad 3.2$$

$$\beta = \frac{\ln \left[\frac{\bar{R}}{L} \sqrt{\frac{1 + v_L^2}{1 + v_R^2}} \right]}{\sqrt{\ln(1 + v_L^2) + \ln(1 + v_R^2)}} \quad 3.3$$

where v_L and v_R = coefficient of variation (COV) of wind load effects and resistance, respectively. If these COVs are less than 0.5 and are the same order of magnitude and $1/4 < v_L/v_R < 4$, then the central load factor, γ :

$$\gamma = e^{(0.55\beta v_L)} \quad 3.4$$

In the study, 15 random variables summarized in Table 3.1 were considered. The uncertainties through the Davenport Wind Loading Chain were propagated using the mean centered Monte Carlo sampling technique. The results highlighted the significant effect of uncertainties related to

critical damping ratio and wind speed on peak floor acceleration and drift responses. The inhabitability risk (failure probabilities) computed using the 1-in-10-year wind speeds, reported in Bezabeh et al. (2018c), is compared with the criteria proposed in Bashor and Kareem (2009). According to Bashor and Kareem (2009), major, moderate, and minor complaints could occur if the failure probabilities are higher than 0.54, between 0.136-0.54, and less than 0.136, respectively. These criteria are plotted together the failure probabilities using patch area varying in the color code. As shown in the Figure, a major complaint could occur when the 30-storey tall mass-timber building subjected to the 1-in-10-year wind speeds orthogonal to the broader face of the building. However, a further increase in critical damping ratio beyond 5% could reduce the peak floor acceleration and the failure probabilities. When the wind angle of attack is 90°, a slight increase in damping (e.g., from 0.5% to 2 %) significantly improved the performance. These results indicate that the failure probabilities are mostly dependent on the critical damping ratio (ξ). Therefore, the load factors in designing mass-timber buildings should reflect this effect.

Table 3.1: Parameters of random variables (adopted from Bezabeh et al. 2018b)

Source of uncertainty	Mean	COV	Distribution type	Citation
Observation and analysis of wind speed	1	0.025	Normal	Minciarelli et al. (2001)
Conversion factors between different averaging times	1	0.05	Normal	Minciarelli et al. (2001)
Characterization of the mean wind speed profile	1	0.05	Normal	Bashor et al. (2005)
Wind speed from ASCE 7-10	Wind speed map	0.07	Normal	Bernardini et al. (2014)
Aerodynamic errors during wind tunnel testing	1	0.05	Normal	Minciarelli et al. (2001)
Approximations during pressure integration	1	0.05	Normal	-
Accuracy of similitude concept in the wind tunnel testing	1	0.05	Normal	Minciarelli et al. (2001)
Building frequency	Eigenvalue analysis	0.01	Lognormal	Bashor et al. (2005)
Critical damping ratio	0.25%,0.5%,1%1.5%, 3%, 5%	0.3	Lognormal	Bashor et al. (2005)
Habitability criteria	25milli-g	0.2	Lognormal	Bashor et al. (2005) and NBCC (2010)
Deflection criteria	H/500	0.1	Lognormal	NBCC (2010)

Bezabeh et al. (2018b) investigated the effect of uncertainties using probabilistic performance-based wind engineering framework. In Bezabeh et al. (2018b), the considered source of uncertainties are:

- Stochastic nature of the wind field
- Wind tunnel test procedures
- Structural properties
- Performance criteria

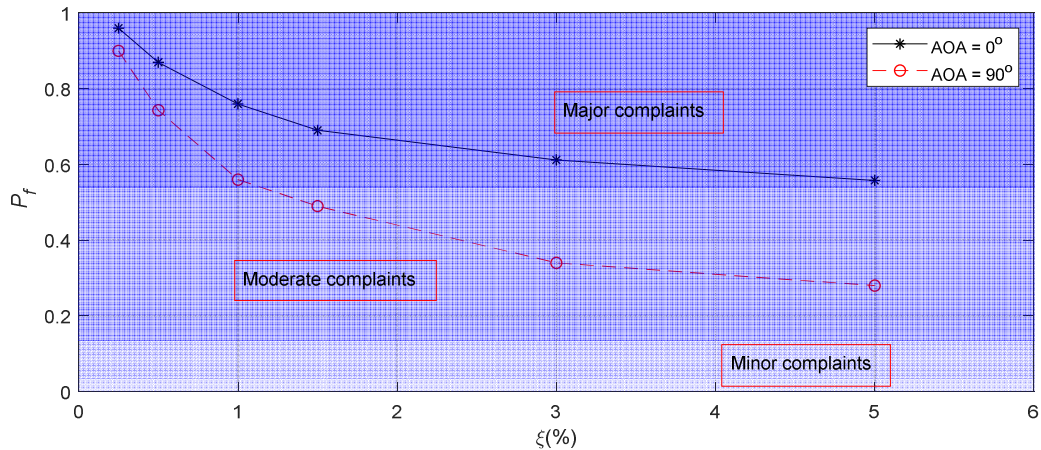


Figure 3.16: Variation of failure probability with a critical damping ratio

Considering the uncertainties presented in Table 3.1, for tall wood buildings, the estimated COV of wind load effects is 0.34. Since the previous section indicated the domino effect of serviceability requirements, a target $\beta = 2.5$ as recommended in Davenport (1983) should be used to calculate the central load factor. For $v_L = 0.34$ and $\beta = 2.5$, the required central load factor to perform the design of tall wood buildings satisfying the deflection limit state is 1.61.

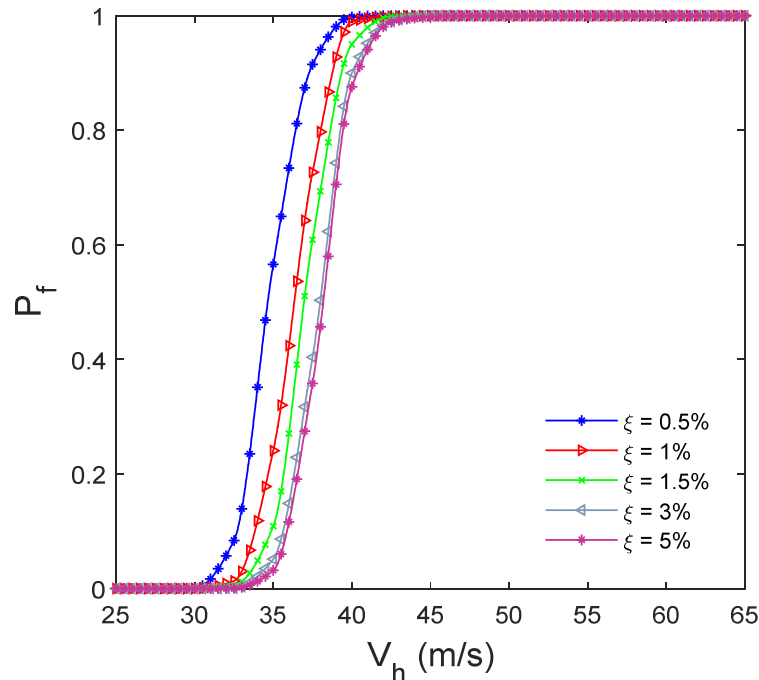


Figure 3.17: Fragility curves for deflection limit state suburban exposure case when $\text{AOA} = 0^\circ$ (Bezabeh et al. 2018b)

In Bezabeh et al. (2018b), for 1-in-50-year wind speed, fragility curves of drift responses were developed (Figure 3.17). These plots indicate the probability of exceeding the NBCC-2015 drift requirement (building height/500) when a 30-storey mass-timber building designed using a load

factor of 1.4 is subjected to design-based wind load. Note that the design load factor = 1.4 do not explicitly account for uncertainties in damping and structural properties of the wood. As shown in Figure 3.17, the failure probability is dependent not only on the COV but on the assumed mean critical damping ratio as well. Therefore, we extracted the failure probabilities to calculate the actual load factors. The calculated actual central load factors indicate the performance of the design based on the current load factors, not necessarily accurately but approximately.

The corresponding central load factors for wind AOA = 0° are 1.51, 1.46, 1.31, 1.25, 1.07 for critical damping ratios of 5%, 3%, 1.5%, 1%, and 0.5%, respectively. This result indicates that if the critical damping ratio of the building is more than 3%, the current load factor could be satisfactory. However, for low damped tall mass-timber buildings, we recommend the use of $\gamma = 1.6$, which could give extra safety for highly damped mass-timber buildings.

Part II: Earthquake Load

Chapter 4

Archetype Development and Seismic Design

4.1 Archetype building

The seismic force modification factors, for the RC-timber hybrid building, are developed for a set of structural configurations and seismic energy dissipation mechanisms (Figure 4.1). Each one of these structural arrangements is called index archetype configurations. The archetype buildings were selected following the FEMA's P695 guidelines (FEMA 2009). Development of the index archetypical configurations considers two basic elements:

- The first is related to characterizing the structural configurations (FEMA 2009). The extent of the representative structural configurations has to be developed by considering: occupancy and use of the building, elevation and plan configuration, building height, structural component type, seismic design category, and gravity load.
- The second is related to the description of the seismic force resisting systems (SFRSs) to capture the likely degradation and collapse mechanisms. This entails capturing the SFRS's: strength and stiffness; inelastic deformation capacity; and seismic design category.

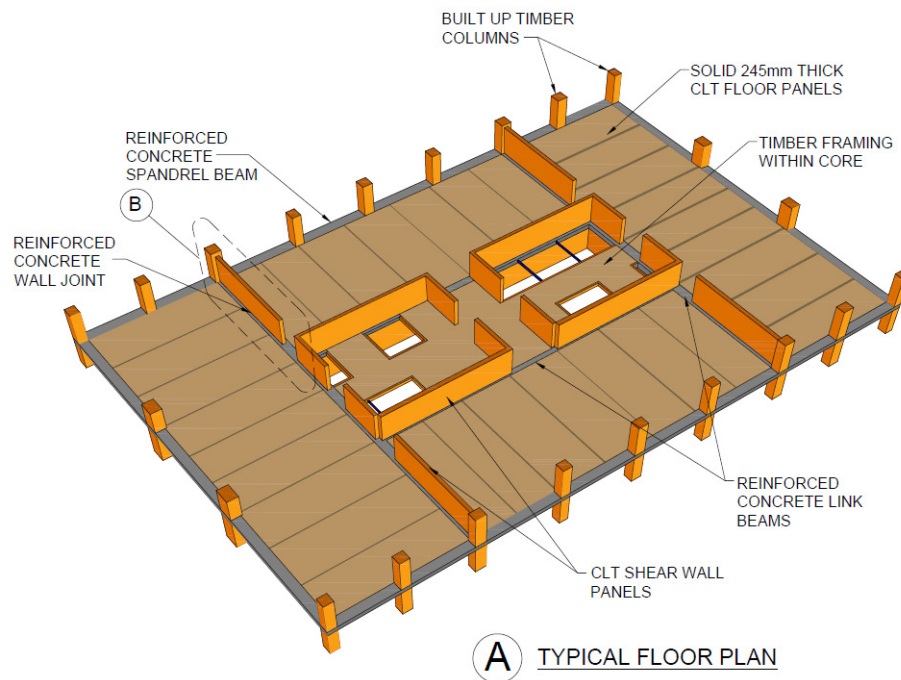


Figure 4.1: Lateral force resisting system: gravity columns and shear walls layout

In this project, the archetype buildings are selected considering different range of *building height*, *structural configurations*, and *seismic energy dissipation mechanism*.

- **Lateral force resisting system configurations:** The seismic force resisting system layout consists of coupled and uncoupled central CLT core walls, with perimeter glulam columns (Figure 4.1). The archetype has a plan dimension of 28.7 m × 40.7 m.
- **Building Height:** A total of three building heights were considered (Figure 4.2). 10-storey uncoupled shear walls, and 15- and 20-storey coupled shear wall buildings. The buildings are denoted as 10S-U, 15S-C, and 20S-C, respectively.

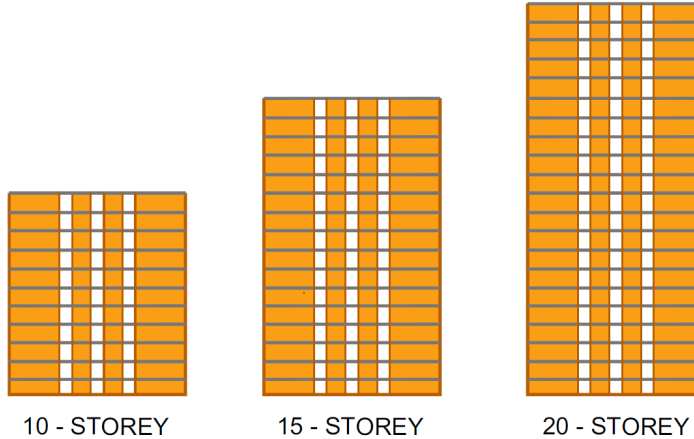


Figure 4.2: 10-, 15- and 20-storey hybrid mass-timber buildings

- **Seismic force modification factors:** An overstrength factor $R_o = 1.5$ is used for all buildings. The ductility factor R_d used are: for 10S-U building, $R_d = 2$ and 3; For 15S-C $R_d = 2$; and for 20S-C buildings, $R_d = 2, 3$ and 4.
- **Seismic energy dissipation mechanism:** In timber structures, the ductility and seismic energy dissipation are maintained through the connections. Hence in this study, with the intent of achieving ductile systems, two types of energy dissipation mechanism are proposed. The first category of archetypes is uncoupled wall systems. In these systems, the primary energy dissipation mechanism is through yielding of the wall-to-wall planer connections and the hold-downs (e.g. Izzi *et al.* 2018; Zhang *et al.* 2018; Chen and Chui 2017; Pei *et al.* 2016; Tesfamariam *et al.* 2015). The second one is coupled wall systems using RC coupling beams (link beams). In these systems, the link beams provide a ductile mechanism by acting like a fuse protecting the CLT wall assemblies. Once the link beams degrade under a cyclic loads, the hold downs and shear connections start to yield. Finally, when these shear connections fail, a collapse of a structure is instantaneous.

4.2 Seismic design

The concrete jointed system composed of CLT floor panels, concrete joints that provide rigid support to the floor panels, periphery glulam columns, and central CLT core walls. The CLT floors, if provided with sufficient panel to panel and panel to vertical members connection detail, will act as a rigid diaphragm (Izzi *et al.* 2018, SOM 2013). The lateral stiffness is attributed mainly to the core and shear walls. In addition to the lateral loads, the core walls also carry a significant portion of the gravity loads. CLT walls act as a rigid body that can undergo translation or sliding, overturning and a combination of thereof (Casagrande *et al.* 2018, Izzi *et al.* 2018, Gavric *et al.* 2013). The CLT wall are designed following CSA 086 (CSA 2014) and capacity design principles.

4.3 Numerical modeling and analysis considerations

Three-dimensional (3-D) ETABS (2016) models are developed for each of the index archetype buildings to perform and quantify both linear static and dynamic action effects resulting from the different loading scenario (Figure 4.4).

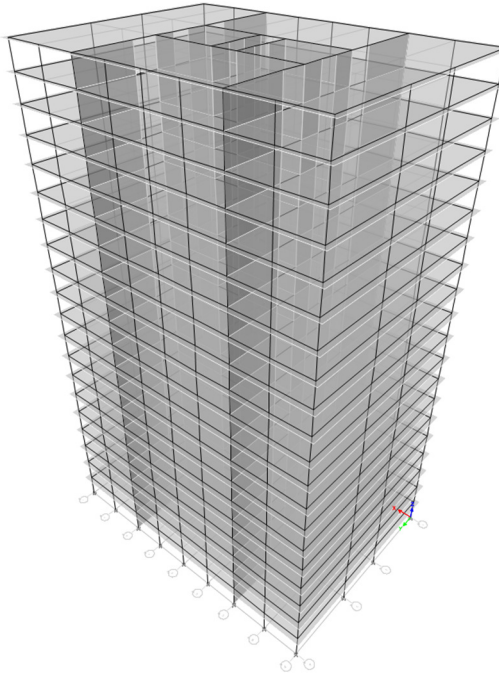


Figure 4.3: Structural model representations of 20S-C building in ETABS

The following assumptions were considered in the numerical modeling:

- The CLT shear walls are modeled with thin-shell finite elements. CLT is a layered material with discrete properties across each of the alternating layers, i.e., anisotropic material. The CLT is modeled with equivalent single cross-section an isotropic material properties assigned by incorporating stiffness modification in the primary stiffness directions.
- CSA O86 (CSA 2014) limits the aspect ratio (height to length ratio) of CLT shear walls to be varying from 1:1 to 4:1 to have the desired type of energy dissipation. However, in

in the finite element modeling, the wall panels are modeled with a single panel and the flexibility that inherently exists between wall panel connections is not considered. In the nonlinear modeling, however, the wall-to-wall panel connections are modeled.

- The glulam columns, concrete- spandrels, joints, and link beams are modeled with line elements.
- Fixed supports are assigned at the base of the glulam columns and the CLT walls. In reality, the connections provided have some level of flexibility. But for the preliminary design assuming fixity lead to a conservative design.
- Table 4.1 summarizes the material properties used along the CLT panels, glulam columns, and concrete joints.

Table 4.1: Material properties

Material	Weight (kN/m ³)	Modulus of elasticity, E (MPa)	Poisson's Ratio, v	Remark
CLT floor panel	6.0	9652	0.44	
CLT shear wall	6.0	9652	0.44	The E value is adapted for both flexural and axial stiffness of the material.
Glulam column	6.0	9652	0.44	
Concrete beam	24.5	24,647.5	0.2	

- The CLT floor panels are designed as a one-way slab system spanning between the central wall systems and periphery framings. Further, the concrete joints over the central walls and the spandrel beams around the periphery are designed to provide a fixed support to the CLT. With these assumptions, the CLT floors are designed with 245 mm thickness. The CLT panels are modeled as a membrane thus neglecting it's out of plane stiffness. As discussed in the previous section, by providing adequate connection details between the CLT floor panels as well as the CLT floor panels to vertical members, the entire floor system can act as connected by approximately a rigid diaphragm.
- Considering the building is going to serve as an apartment or office building, a specified live load of 2.4 kN/m² is adopted according to NBCC 2015. Moreover, to account the weight of floor finishes and partition load, a superimposed additional load of 2.8 kN/m². Further, no snow loading is considered for the site taken is in Vancouver.
- The seismic mass source is evaluated by taking 100% of the dead loads.
- The archetype buildings are grouped under Normal Importance Category of building according to NBCC (2015). Therefore the associated Importance Factor = 1.
- The building was assumed to be located in Vancouver, located 49.243129 latitude and -123.125298 longitude, and hence according to NBCC 2015, 2% in 50 years probability of exceedance uniform hazard spectrum is adopted as shown in Figure 4.4.
- The site Soil Class is assumed to be Class C (very dense soil or soft rock with average shear wave velocity, V_{s30} 450 m/s) according to NBCC (2015) site class classification.
- Earthquake accelerations in only the two principal orthogonal axes are considered.
- To combine the modal contributions to the total base shear, complete quadratic combination (CQC) is implemented.
- Accidental eccentricity is accounted in by taking it to be equal to $\pm 10\%$ of the orthogonal dimension to the seismic action.

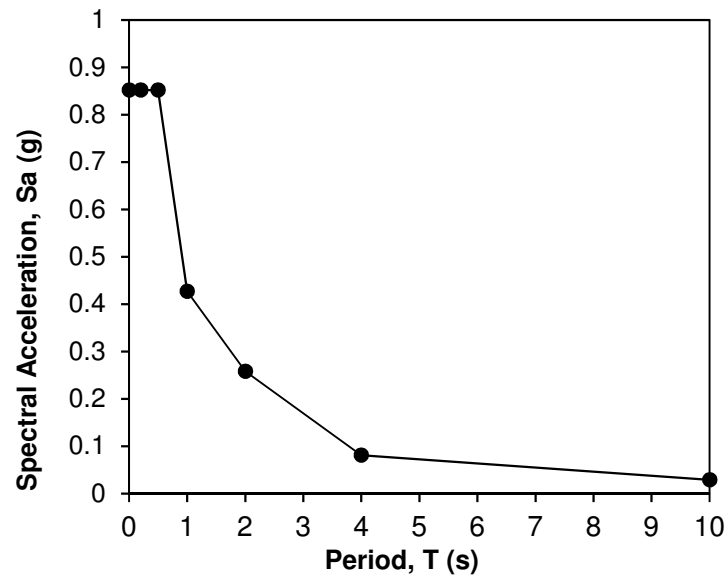


Figure 4.4: 5% damped response spectrum for Vancouver

Chapter 5

OpenSees Numerical Model

5.1 Introduction

A perspective representation of the building is depicted in Figure 5.1. The floor plan for the section callout A is shown in Figure 4.1. The slabs are a one-way CLT panels system supported by the concrete joints running along the perimeter of the buildings and the central core wall system.

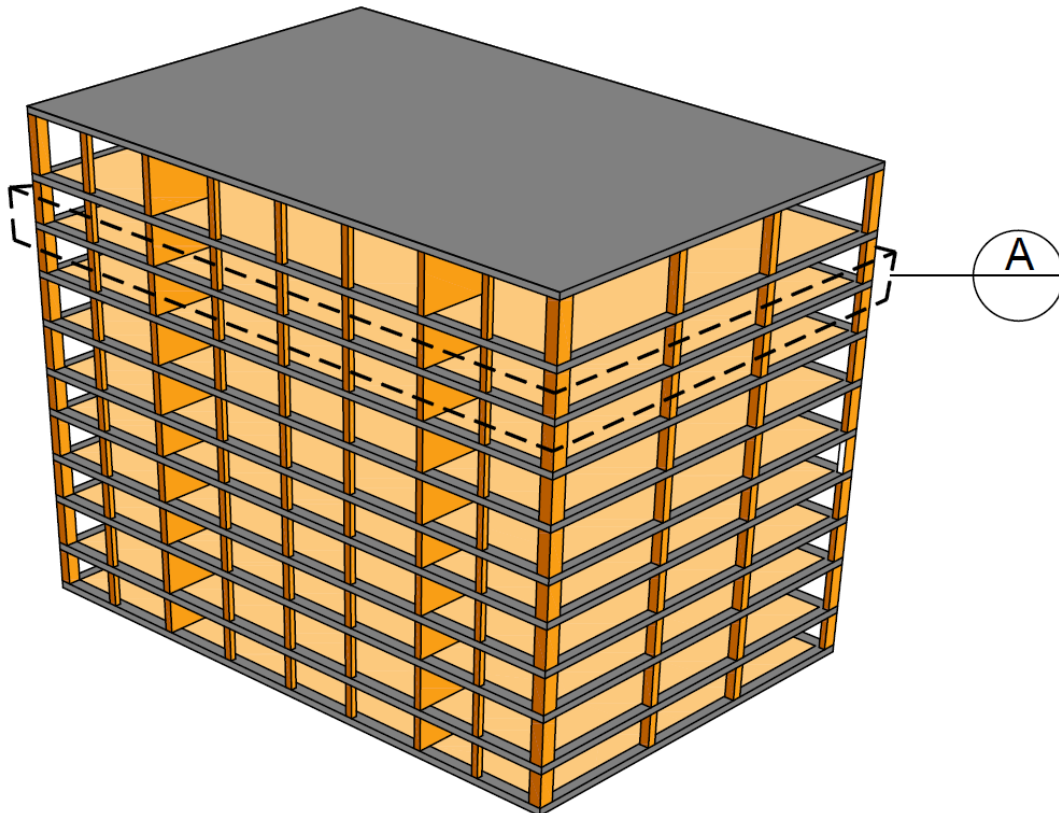


Figure 5.1: Perspective view of the 10-storey uncoupled (10S-U) hybrid building

Numerical modeling was carried out in the Open System for Earthquake Engineering Simulation (OpenSees) finite element framework (Mazzoni *et al.* 2006). A three-scale modeling approach was adopted:

1. Modeling the single elements and connections of the system, also calibrating with experimental results where necessary.
2. Formulating the numerical model for the CLT wall system (Figure 5.2). Component level modeling and calibrations were performed first for each element, i.e., CLT wall connections, CLT wall panels and reinforced-concrete link beams. Subsequently, these components were assembled to achieve the desired system-level property.

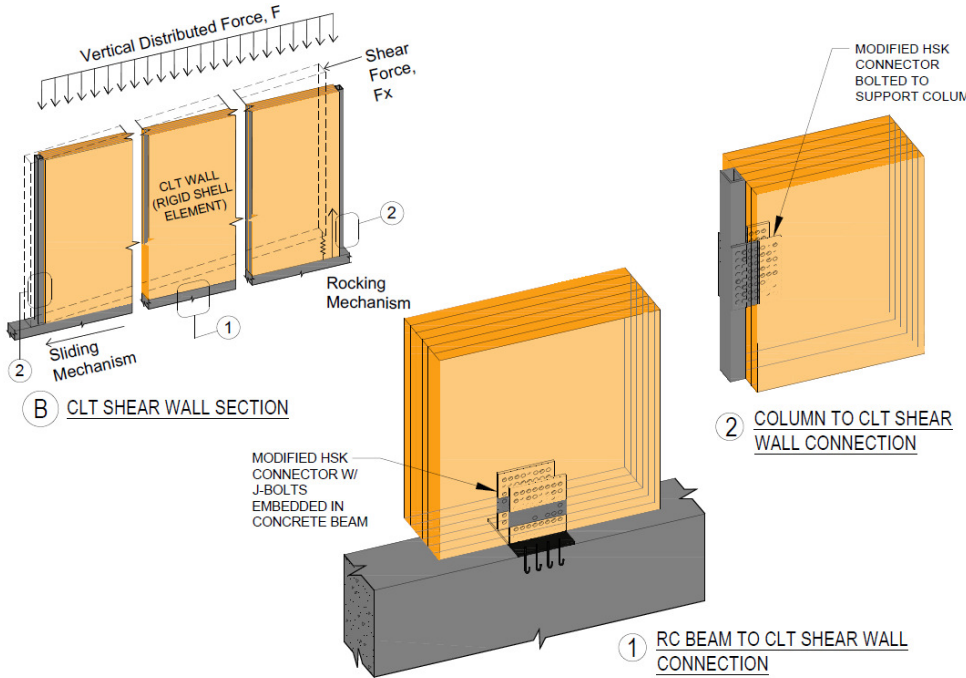


Figure 5.2: CLT shear wall assembly and connection detailing

3. Assembling all component models to form the global system. The elements required are (Figure 5.2): CLT wall shear connections, hold downs, CLT wall 2D elements, and reinforced concrete coupling beams. For the 3D OpenSees model, shell elements, frame elements and zero-length springs are used for the CLT walls, beam-columns and connections respectively. A representation of the shell and frame elements of the 3D OpenSees model is shown in Figure 5.3 for the 10-storey uncoupled (10S-U) building.

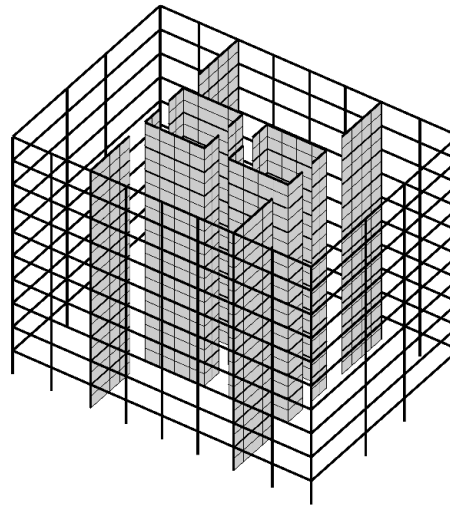


Figure 5.3: Structural model representation in OpenSees

The following subsections illustrates both the component and system level modeling and calibration procedures.

5.1 CLT wall connections

For mass timber buildings located in high seismicity areas, increased connection ductility is required to contribute to energy dissipation in the case of strong seismic events. The modified HSK connection (Figure 5.4) (Zhang 2017; Zhang *et al.* 2018) has high strength and ductility, which are appropriate for use in high-rise timber and hybrid timber buildings.

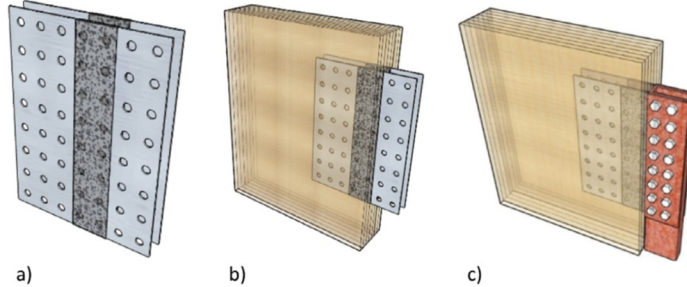


Figure 5.4: Modified HSK connection (Zhang 2017): a) Perforated steel plate with taped rows; b) Plates embedded and adhesively connected to CLT; c) Connection to stiff structural element

Experimental results reported in Zhang *et al.* (2018) are used to calibrate the shear and hold-down connections numerical models. For the un-coupled system, the HSK connections are the primary inelastic elements participating in the inelastic mechanism of the lateral system. For the coupled system, the modified HSK connections respond as secondary fuse-elements and they are expected to yield in succession with the reinforced concrete link-beams. For the connections, macro-models calibrated to the experimental results are used to represent the connection behavior. Consequently, zero-length elements are used with the calibrated connection properties in OpenSees. The zero-length element OpenSees command is:

```
element zeroLength $eleTag $iNode $jNode -mat $matTag1 $matTag2 ... -dir $dir1 $dir2 ...<-doRayleigh $rFlag>
<-orient $x1 $x2 $x3 $yp1 $yp2 $yp3>
```

\$eleTag	unique element object tag
\$iNode \$jNode	end nodes
\$matTag1 \$matTag2 ...	tags associated with previously-defined UniaxialMaterials
\$dir1 \$dir2 ...	material directions: 1,2,3 - translation along local x,y,z axes, respectively; 4,5,6 - rotation about local x,y,z axes, respectively
\$x1 \$x2 \$x3	vector components in global coordinates defining local x-axis (optional)
\$yp1 \$yp2 \$yp3	vector components in global coordinates defining vector yp which lies in the local x-y plane for the element. (optional)
\$rFlag	optional, default = 0 rFlag = 0 NO RAYLEIGH DAMPING (default) rFlag = 1 include Rayleigh damping

Failure from low-cycle fatigue of the perforated steel plate eventually manifests in an abrupt manner (Zhang *et al.* 2018). The OpenSees Ibarra-Medina-Krawinkler (IMK) *Bilin uniaxial material* (Ibarra *et al.* 2005) is used to calibrate the connections experimental results. The IMK material model includes both in-cycle and cyclic deterioration capabilities. This makes it ideal for collapse simulation studies. The connection failure observed in the experimental results can be reproduced by the IMK model, thus allowing for force-redistribution and collapse mechanism formation in the system. The OpenSees command for the IMK *Bilin uniaxial material* model is:

uniaxialMaterial Bilin \$matTag \$K0 \$as_Plus \$as_Neg \$My_Plus \$My_Neg \$Lamda_S \$Lamda_C \$Lamda_A \$Lamda_K \$c_S \$c_C \$c_A \$c_K \$theta_p_Plus \$theta_p_Neg \$theta_pc_Plus \$theta_pc_Neg \$Res_Pos \$Res_Neg \$theta_u_Plus \$theta_u_Neg \$D_Plus \$D_Neg <\$nFactor>	
\$matTag	integer tag identifying material
\$K0	elastic stiffness
\$as_Plus	strain hardening ratio for positive loading direction
\$as_Neg	strain hardening ratio for negative loading direction
\$My_Plus	effective yield strength for positive loading direction
\$My_Neg	effective yield strength for negative loading direction (negative value)
\$Lamda_S	Cyclic deterioration parameter for strength deterioration
\$Lamda_C	Cyclic deterioration parameter for post-capping strength deterioration
\$Lamda_A	Cyclic deterioration parameter for acceleration reloading stiffness deterioration (is not a deterioration mode for a component with Bilinear hysteretic response).
\$Lamda_K	Cyclic deterioration parameter for unloading stiffness deterioration
\$c_S	rate of strength deterioration. The default value is 1.0.
\$c_C	rate of post-capping strength deterioration. The default value is 1.0.
\$c_A	rate of accelerated reloading deterioration. The default value is 1.0.
\$c_K	rate of unloading stiffness deterioration. The default value is 1.0.
\$theta_p_Plus	pre-capping rotation for positive loading direction (often noted as plastic rotation capacity)
\$theta_p_Neg	pre-capping rotation for negative loading direction (often noted as plastic rotation capacity) (positive value)
\$theta_pc_Plus	post-capping rotation for positive loading direction
\$theta_pc_Neg	post-capping rotation for negative loading direction (positive value)
\$Res_Pos	residual strength ratio for positive loading direction
\$Res_Neg	residual strength ratio for negative loading direction (positive value)
\$theta_u_Plus	ultimate rotation capacity for positive loading direction
\$theta_u_Neg	ultimate rotation capacity for negative loading direction (positive value)
\$D_Plus	rate of cyclic deterioration in the positive loading direction (this parameter is used to create assymetric hysteretic behavior for the case of a composite beam). For symmetric hysteretic response use 1.0.
\$D_Neg	rate of cyclic deterioration in the negative loading direction (this parameter is used to create assymetric hysteretic behavior for the case of a composite beam). For symmetric hysteretic response use 1.0.
\$nFactor	elastic stiffness amplification factor, mainly for use with concentrated plastic hinge elements (optional, default = 0).

The *Bilin uniaxial material* calibration parameters are summarized in Table 5.1 and the results are depicted in Figure 5.5.

Table 5.1: Calibration parameters of *IMK Bilin uniaxial material* for connection with 11 shear links and 2 covered rows

Number of shear links	F _y kN	E kN/mm	b
11 SLs	26.3	40.0	0.012
23 SLs	52.2	108.7	0.024

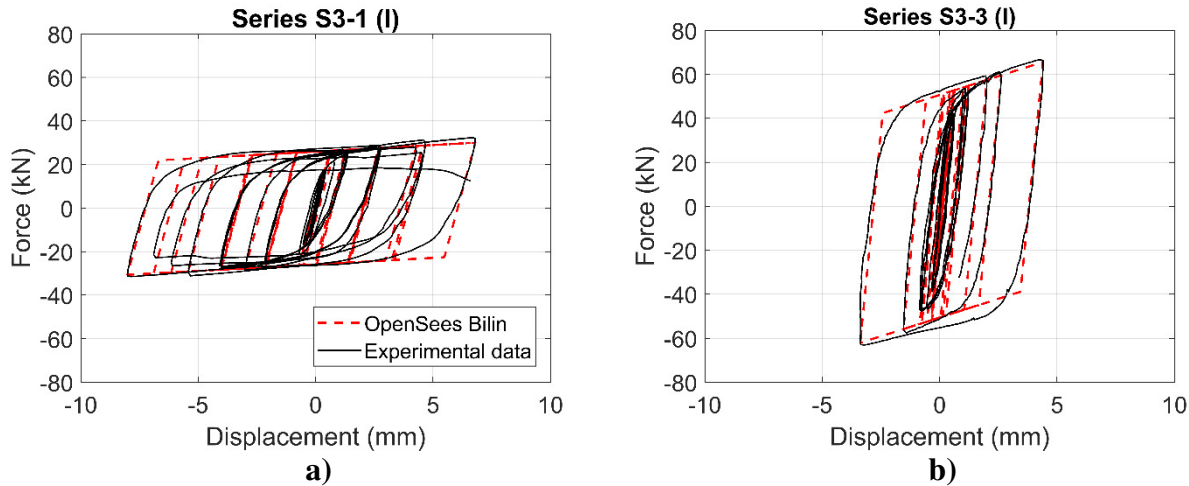


Figure 5.5: Calibrated modified HSK connection: a) with 11 shear links and 2 taped rows; b) with 23 shear links and 1 taped row

5.2 Hold downs

In simulating the hold-downs, the contact between the CLT wall and the ground or between the CLT wall and the RC beam below has to be explicitly accounted for. This is accomplished by introducing an elastic no-tension (ENT) element spring in OpenSees (Figure 5.6). The OpenSees command for the ENT uniaxial material is:

```
uniaxialMaterial ENT $matTag $E
$matTag           integer tag identifying material
$E               tangent
```

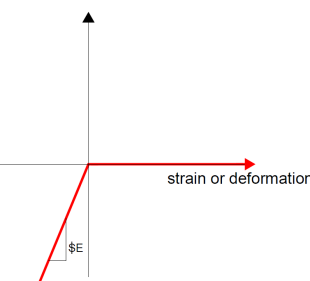


Figure 5.6: OpenSees elastic-no tension (ENT) material (<http://opensees.berkeley.edu>)

Large elastic stiffness value is assigned to the ENT spring under compression to capture the contact between the CLT wall and the base (ground or the lower floor beam). The ENT spring works in parallel with the hold-down connection (Figure 5.7). The parallel spring formulation is implemented in OpenSees with the following command:

```
uniaxialMaterial Parallel $matTag $tag1 $tag2 ... <-factors $fact1 $fact2 ...>
$matTag           integer tag identifying material
$tag1 $tag2 ...   identification tags of materials making up the material model
$fact1 $fact2 ... factors to create a linear combination of the specified materials. Factors can be negative
                     to subtract one material from another. (optional, default = 1.0)
```

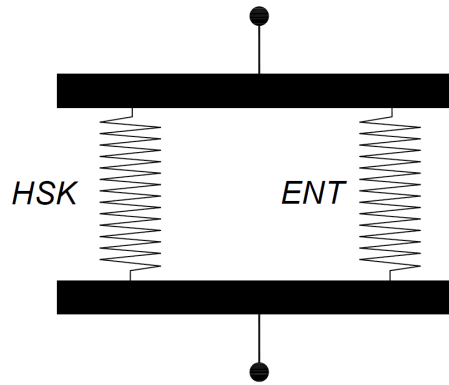


Figure 5.7: In-parallel formulation of the Steel02 and ENT uniaxial material models for hold-down simulation

The friction force at the contact between the CLT wall and the floor or the RC beam is assumed to be negligible and is not accounted for. This is a reasonable assumption, since the friction force magnitude has not been found to considerably contribute to overall wall response (Izzy *et al.*, 2018).

5.3 Shear connections

Given that the system is designed to respond inelastically in rocking, the horizontal deformation (slippage) of the walls is not considered in the inelastic mechanism, and consequently the shear connections are capacity-designed. This is in accordance with the Canadian seismic code, wherein only the rocking and the in-between shear of adjacent CLT walls is allowed as the primary inelastic mechanism (Canadian Wood Council, 2017). The capacity design is usually carried out for the maximum probable forces of the hold-downs in the un-coupled system and the maximum probable forces of the link beams and the hold-downs in the coupled system. In the present study the conservative upper limit is considered for the capacity lateral forces. According to the formulation:

$$F_{cd} = \frac{F_{el}}{1.3} \quad 5.1$$

where F_{cd} = base shear force used for the capacity design and F_{el} is the elastic base shear from the response-spectrum analysis. In the OpenSees model, elastic uniaxial springs with large elastic stiffness are used to model the shear connections between the CLT walls and the RC beams.

5.4 Modelling CLT wall panels

The CLT wall panel possesses high elastic stiffness, and it essentially behaves as a rigid body during in-plane response. Consequently the CLT wall panels are modelled with elastic elements. Its simulation in the numerical model is accomplished by utilizing 2D-geometry shell elements. The shell element of OpenSees is used that accounts for both in-plane and out-of-plane response in a 3D modelling domain. The command for this element is:

```
element ShellMITC4 $eleTag $iNode $jNode $kNode $lNode $secTag
$eleTag unique element object tag
$iNode $jNode $kNode $lNode four nodes defining element boundaries, input in counter-
clockwise order around the element.
$secTag tag associated with previously-defined
SectionForceDeformation object.
Currently must be either a PlateFiberSection, or
ElasticMembranePlateSection
```

For the material model of the CLT wall, the elastic orthotropic multi-axial material of OpenSees is utilized, with effective Young's modulus and Poisson's ratio values (Table 4.1). This simplification of the orthotropic material is deemed reasonable.

5.5 System-level behavior

By assembling all elements, with their respective behaviors as described in the previous paragraphs, the 3D Opensees model is created. This model is used to conduct incremental dynamic analysis (IDA) for the purpose of deriving the system's collapse fragility curves for all archetype buildings considered in this study.

5.5.1 Wall meshing

A convergence study conducted for both individual walls and the whole structural system showed that a shell element discretization of four by two elements for the long walls in both horizontal directions is adequate for the purposes of representing the wall element response and assisting in the connectivity of all other elements (i.e. connections and RC beams). More specifically, an eigenvalue analyses conducted for a wall mesh of 8 by 4 elements and a wall mesh of 4 by 2 elements showed similar results (approximately 1% difference in all of the first three structural periods).

5.5.2 CLT floors

The CLT floor panels are considered to provide full rigidity in the in-plane deformation of the floors. Thus a rigid diaphragm constraint is assumed to account for a rigid-body motion of all structural elements at the floor elevations and for the floor in-plane degrees of freedom. The rigid diaphragm command in OpenSees is:

```
rigidDiaphragm $perpDirn $masterNodeTag $slaveNodeTag1 $slaveNodeTag2 ...
$eleTag unique element object tag
$iNode $jNode $kNode $lNode four nodes defining element boundaries, input in counter-clockwise order
$secTag tag associated with previously-defined SectionForceDeformation object.
Currently must be either a PlateFiberSection, or ElasticMembranePlateSection
```

5.5.3 Beam-to-wall interface

In addition to the rigid diaphragms, additional constraints are required at the interfaces of the walls with the corresponding RC beams. Modified HSK connectors are utilized to provide for wall stability in out-of-plane translational and rotational motion. These connections are expected to provide resistance for small-amplitude (serviceability) earthquake excitation, based on their elastic stiffness. For rare strong-motion excitations, the modified HSK contributions can be neglected as most of horizontal resistance is provided by the in-plane resistance of the perpendicular wall connections. Given the relative flexibility and the small contribution of the wall weak axis to the total response, a reasonable assumption is to consider the out-of-plane connections as completely rigid (e.g. Fairhurst, 2014).

Furthermore, an assumption has to be made regarding the friction resistance at the interface. Previous studies have shown that this resistance is not considerable and that it does not add much to the total system resistance. Consequently, it is conservatively neglected in the present study. Hence, only vertical springs with infinite stiffness in compression and zero stiffness in tension are used between the interface nodes to account for the motion constraint that the lower walls impose on the upper walls. The ENT uniaxial material is used for this purpose, as described in a previous paragraph.

5.5.4 Wall-to-wall interface

In this system, two types of wall-to-wall vertical interfaces are present. The first is the in-plane walls vertical interface, which is dictated by the commercial CLT panel dimensions, the allowable limit for single wall panel aspect ratio and by transferability and constructability constraints. The second type is the vertical interface between a CLT wall panel and a perpendicular CLT wall panel

that form the central core. The connection between perpendicular walls is one of the least studied in the literature, due to the fact that it is difficult to come up with a connection that transfers shear force from a wall to the perpendicular plane.

For both interfaces, the capping beam connecting the wall panels with the corresponding upper or lower floor panels, functions as a binding element that restrains the relative deformations in the vertical wall interfaces. As a result, and for the sake of simplicity, the vertical wall interfaces were considered as completely rigid in the present study. This assumption can be justified by the binding action of the capping RC beams that restrain the different wall panels to move together, in a rigid body sense. Casagrande *et al.* (2018) show that this can also be the case when the shear connections provided at these interfaces are very strong and rigid.

5.5.5 Modeling of reinforced concrete link beams in the coupled-wall system

The reinforced concrete link beams that couple the CLT walls are the main fuse elements in the coupled-system and they are the first members to yield in the case of a strong seismic event. Hence, in the present study, they are designed as the weakest elements, providing most of the building's ductility, with due consideration given in modeling their inelastic response.

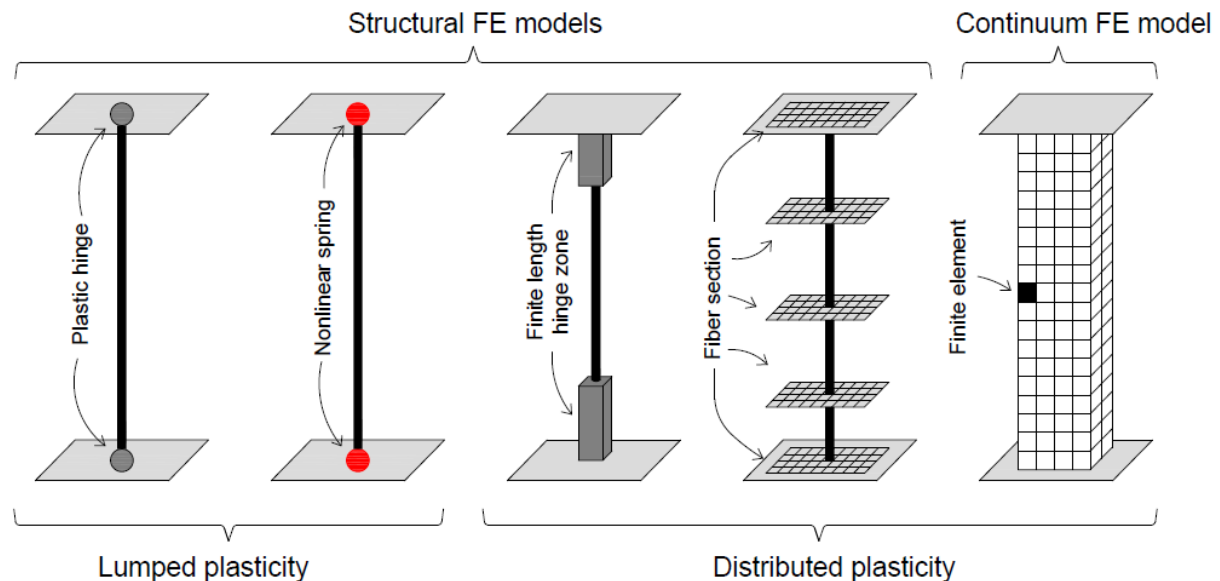


Figure 5.8: Frame element modeling alternatives (Astroza *et al.*, 2015)

Given the element lengths and cross-sections obtained from design, the link beams are assumed to bear negligible shear deformation and can consequently be regarded as responding according to the Euler-Bernoulli beam theory. Given this assumption, either distributed or lumped plasticity models can be used for modeling purposes. Lumped-plasticity models (or macro-models) present a more abstract simulation approach, wherein all member-plasticity is concentrated at particular

points of the line-element that are expected to bear the largest inelastic deformations. In a coupling beam element, these points are the end points of the beam. Nonlinear springs are assigned at these points, and their moment-rotation inelastic relationships are based on calibration with experimental results. Lumped-plasticity modeling is advantageous in terms of computational efficiency and is capable of simulating degradation and instability phenomena, given that calibration with experiments up to failure has taken place. On the other hand, inelastic spring properties are obtained from experimental results in a statistical sense, and the subtle interactions at the cross-section level as well as the moment-axial force interaction are not explicitly accounted for. Figure 5.8 presents the several modeling options for frame elements.

There are many research studies focusing on the calibration of numerical macro-models to experimental results for reinforced concrete beam-columns. In the present study, the modeling procedure follows the research studies conducted at the Stanford University (Haselton *et al.*, 2008; Lignos and Krawinkler, 2012) that utilize the Ibarra-Medina-Krawinkler (IMK) deterioration model (Ibarra *et al.*, 2005). More specifically, the IMK peak-oriented model that has been calibrated to more than 250 reinforced concrete beam-column test specimens is adopted. The parameters of the IMK peak-oriented model are derived from the equations developed by Haselton *et al.* (2008).

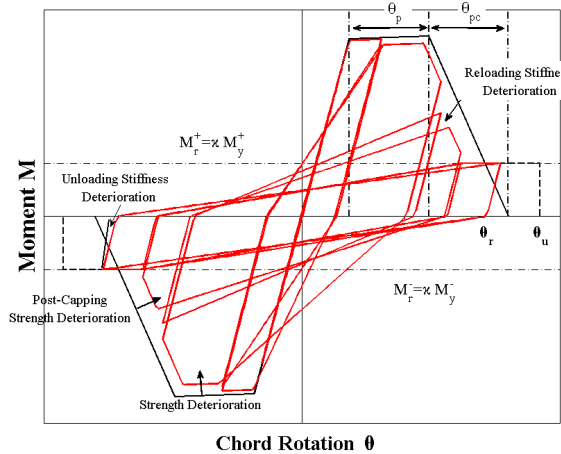


Figure 5.9: Modified Ibarra-Medina-Krawinkler peak-oriented model
[\(<http://opensees.berkeley.edu>\)](http://opensees.berkeley.edu)

Figure 5.9 shows the monotonic backbone and the cyclic response of the IMK peak-oriented material along with the strength and stiffness deterioration modes. As the model includes both static (backbone curve negative slope) and cyclic deterioration capabilities, all major forms of deterioration are captured and thus the collapse capacity of the building subjected to large seismic

forces can be reliably assessed. The IMK peak-oriented uniaxial material command, takes the following form:

```
uniaxialMaterial ModIMKPeakOriented $matTag $K0 $as_Plus $as_Neg $My_Plus $My_Neg $Lamda_S
$Lamda_C $Lamda_A $Lamda_K $c_S $c_C $c_A $c_K $theta_p_Plus $theta_p_Neg $theta_pc_Plus
$theta_pc_Neg $Res_Pos $Res_Neg $theta_u_Plus $theta_u_Neg $D_Plus $D_Neg
```

\$matTag	integer tag identifying material
\$K0	elastic stiffness
\$as_Plus	strain hardening ratio for positive loading direction
\$as_Neg	strain hardening ratio for negative loading direction
\$My_Plus	effective yield strength for positive loading direction
\$My_Neg	effective yield strength for negative loading direction (negative value)
\$Lamda_S	Cyclic deterioration parameter for strength deterioration [$E_t = \text{Lamda}_S * M_y$, see Lignos and Krawinkler (2011); set Lamda_S = 0 to disable this mode of deterioration]
\$Lamda_C	Cyclic deterioration parameter for post-capping strength deterioration [$E_t = \text{Lamda}_C * M_y$, see Lignos and Krawinkler (2011); set Lamda_C = 0 to disable this mode of deterioration]
\$Lamda_A	Cyclic deterioration parameter for accelerated reloading stiffness deterioration [$E_t = \text{Lamda}_A * M_y$, see Lignos and Krawinkler (2011); set Lamda_A = 0 to disable this mode of deterioration]
\$Lamda_K	Cyclic deterioration parameter for unloading stiffness deterioration [$E_t = \text{Lamda}_K * M_y$, see Lignos and Krawinkler (2011); set Lamda_K = 0 to disable this mode of deterioration]
\$c_S	rate of strength deterioration. The default value is 1.0.
\$c_C	rate of post-capping strength deterioration. The default value is 1.0.
\$c_A	rate of accelerated reloading deterioration. The default value is 1.0
\$theta_p_Plus	pre-capping rotation for positive loading direction (often noted as plastic rotation capacity)
\$theta_p_Neg	pre-capping rotation for negative loading direction (often noted as plastic rotation capacity) (must be defined as a positive value)
\$theta_pc_Plus	post-capping rotation for positive loading direction
\$theta_pc_Neg	post-capping rotation for negative loading direction (must be defined as a positive value)
\$Res_Pos	residual strength ratio for positive loading direction
\$Res_Neg	residual strength ratio for negative loading direction (must be defined as a positive value)
\$theta_u_Plus	ultimate rotation capacity for positive loading direction
\$theta_u_Neg	ultimate rotation capacity for negative loading direction (must be defined as a positive value)
\$D_Plus	rate of cyclic deterioration in the positive loading direction (this parameter is used to create asymmetric hysteretic behavior for the case of a composite beam). For symmetric hysteretic response use 1.0.
\$D_Neg	rate of cyclic deterioration in the negative loading direction (this parameter is used to create asymmetric hysteretic behavior for the case of a composite beam). For symmetric hysteretic response use 1.0.

Chapter 6 Overstrength and Ductility Factors using Static Pushover Analysis

The overstrength R_o and ductility R_d related force reduction factor of the archetype buildings are developed following FEMA P695 (FEMA 2009). The National Earthquake Hazards Reduction Program (NEHRP) (FEMA 2004) and NBCC (2015) define seismic performance factors that reduce the elastic design loads of structures. For new structure, the FEMA P695 (FEMA 2009) report provides a guideline in the Quantification of Building Seismic Performance Factors, i.e., overstrength factor (denoted as Ω_o) and ductility factor (denoted as R) (Figure 6.1). The NBCC 2015 splits the R factors into R_d and R_o (Figure 6.2).

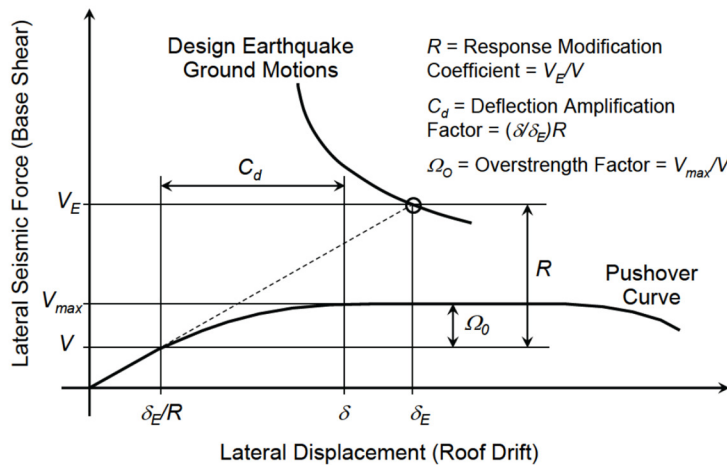


Figure 6.1: Illustration of seismic performance factors (R , Ω_o , and C_d) (from FEMA P695)

Using Figure 6.1 as a reference, the equations used to derive Ω_o and R , are:

$$\Omega_o = \frac{V_{max}}{V} \quad 6.1$$

$$R = \frac{V_E}{V} \quad 6.2$$

where V_E = force level that would be developed in the seismic-force-resisting system, if the system remained entirely linearly elastic for design-based earthquake ground motions (GMs); V_{max} = actual, maximum strength of the fully-yielded system; and V = design seismic base shear. The deflection amplification factor (C_d) is given as:

$$C_d = \frac{\delta}{\delta_E} R \quad 6.3$$

where δ_E/R = drift at the design shear force, and δ = drift when the system is subject to the design-based earthquake GM.

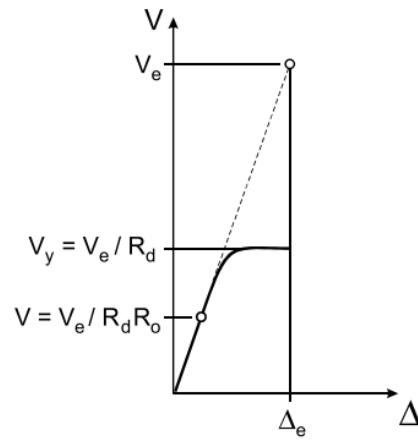


Figure 6.2: Ductility and force reduction factors of NBCC 2005 (Mitchell et al. 2003)

6.1 Capacity (pushover) curves

Pushover analyses are used to trace the system behavior up to collapse. For this system, collapse is considered to have taken place at 5% maximum inter-storey drift ratio (MISDR). This is a conservative estimate corresponding to gravity system failure for RC wall systems (e.g. Kim and Foutch, 2007; Dabaghi *et al.*, 2019).

6.1.1 Pushover of uncoupled system

In the uncoupled system, the CLT walls rock at their base and seismic energy is dissipated through the hold downs. The hold downs at the base of the building yield first, followed by the hold downs at the 1st floor. Figure 6.3 shows pushover curves for the 10S-U building: $R_d = 2$ and 3 . For $R_d = 3$, the gravity loads in combination with the reduced seismic loads lead to a reduced tensile demand in the hold-down connections. As a result, small connections are used for the hold downs. The nonlinearity in the SPO curve is largely from elastic energy dissipation due to wall rocking. On the other hand, the larger seismic demands in the $R_d = 2$ case lead to the design of larger connections, having increased energy dissipation capacity.

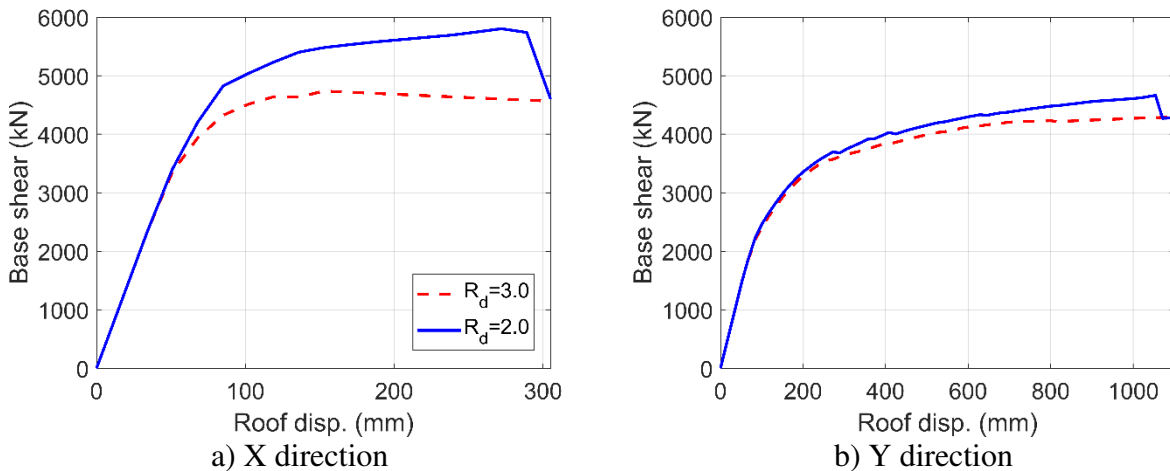


Figure 6.3: Pushover analysis for the 10-storey uncoupled (10S-U) building: $R_d = 2$ and 3

6.1.2 Pushover of coupled system

The coupled system response is based on the successive yielding of two different element types, the RC link-beams (LBs) and the hold-down connections. The collapse limit state is defined at MISDR = 5%, similarly to the uncoupled system. Figure 6.4 and Figure 6.5 show the SPO curves for 15S-C (for $R_d = 2$) and 20S-C ($R_d = 2, 3$ and 4), respectively.

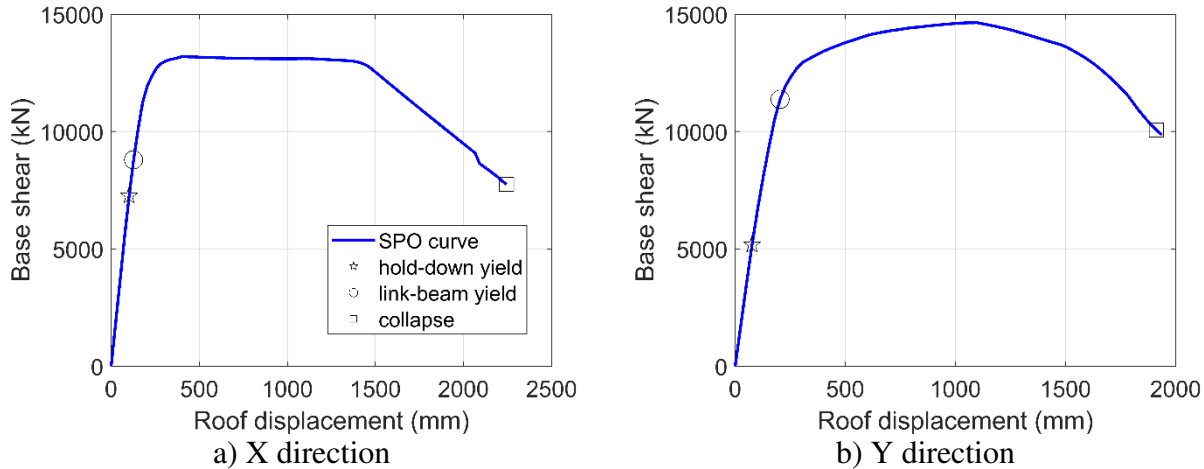


Figure 6.4: Pushover analysis for the 15-storey coupled (15S-C) building: $R_d = 2$

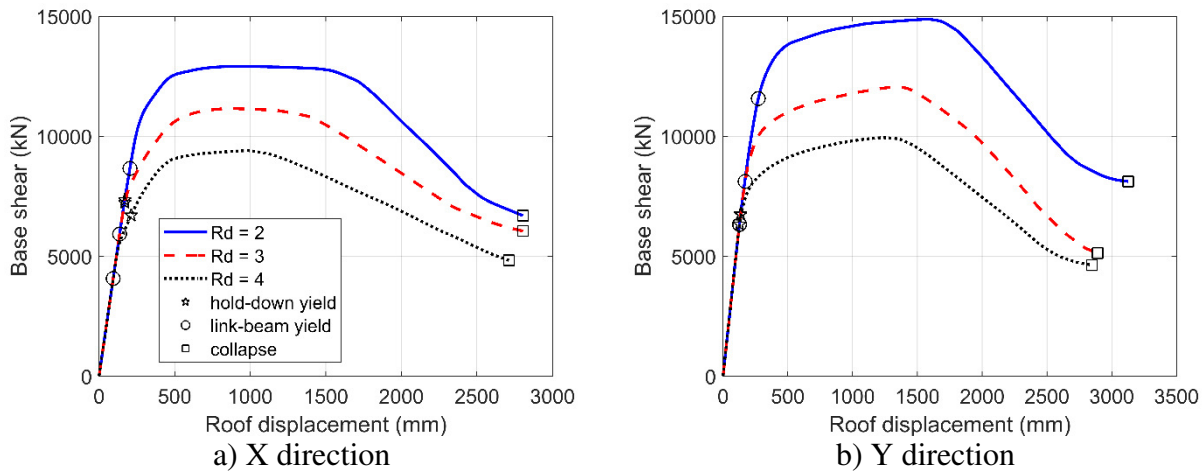


Figure 6.5: Pushover analysis for the 20-storey coupled (20S-C) building: $R_d = 2, 3$ and 4

The LBs are designed to simultaneously yield at all stories for the design earthquake demand. Figure 6.6 shows the progress of LB damage for all storeys as a function of building drift ratio ($\theta_{\text{building}} = \text{roof drift} / \text{building height}$). As is illustrated in Figure 6.6, the LBs yield almost simultaneously during the SPO analysis. After yielding, the plastic mechanism progresses non-uniformly, with the lowermost and the uppermost stories reaching their capacities first. Finally, for the 20S-U, the global collapse which corresponds to an ISDR = 5% is accompanied by the failure (drop to zero capacity) of the uppermost storeys' LBs.

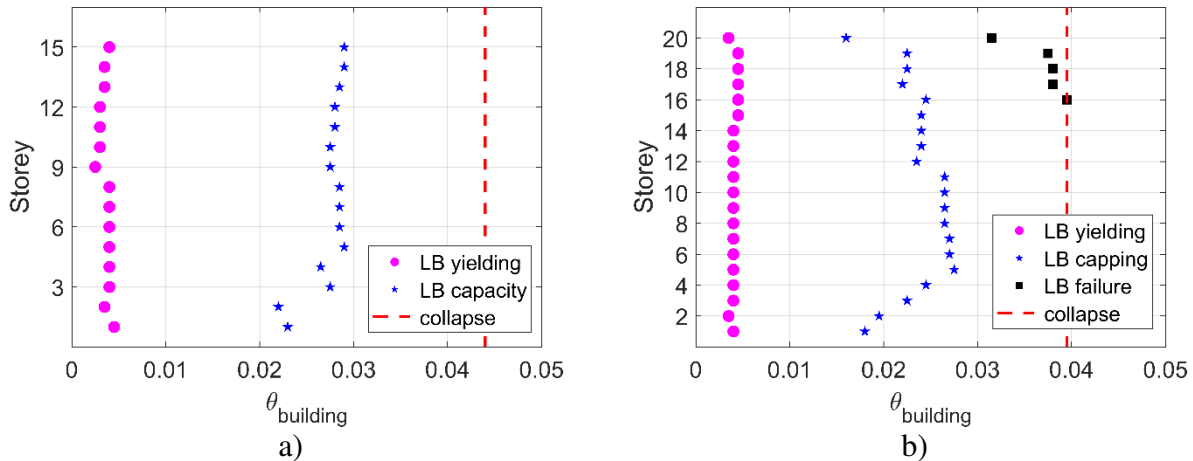


Figure 6.6: Sequence of link-beam (LB) damage in SPO for the coupled system; a) LB backbone; b) 15S-C with $R_d = 2.0$; and c) 20S-C with $R_d = 2.0$

6.2 Static pushover to IDA (SPO2IDA)

Using static pushover to IDA (SPO2IDA) (Vamvatsikos and Cornell, 2006) procedure, the pushover curves shown in Figures 6.5 and 6.6 can be used for preliminary collapse risk estimation of the building. In SPO2IDA, the median and percentile IDA curves are related to the parameters and shape of the static-pushover curve, by assuming a quad-linear pushover curve with distinct elastic, hardening, post-capping and residual branches. The SPO2IDA results for 10S-U buildings are presented in Figure 6.7 (for $R_d = 2$) and Figure 6.8 (for $R_d = 3$). The SPO2IDA results for 15S-C is presented in Figure 6.9 (for $R_d = 2$). The SPO2IDA results for 20S-C Figures 6.10 to 13, for $R_d = 2, 3$, and 4 , respectively.

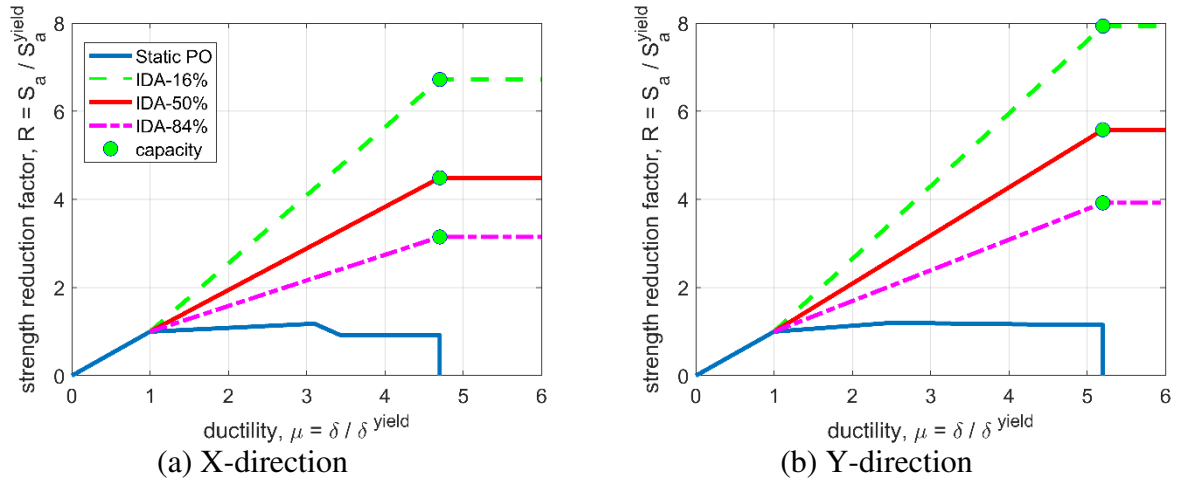
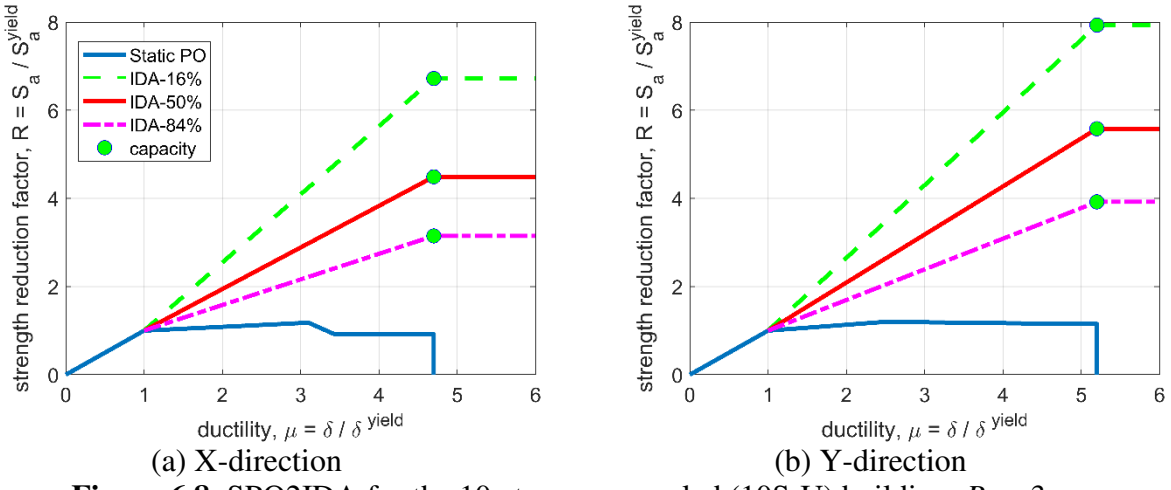
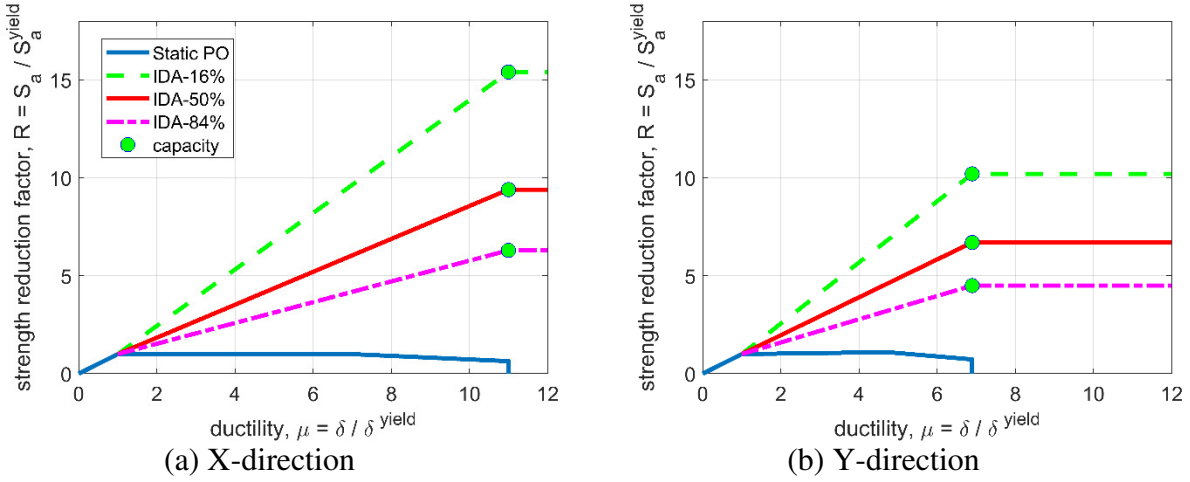
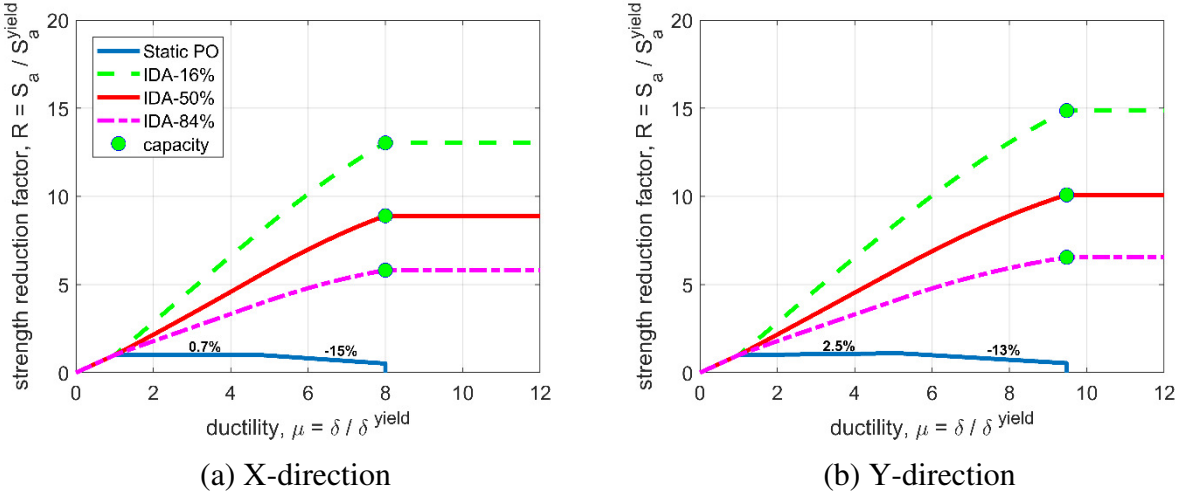
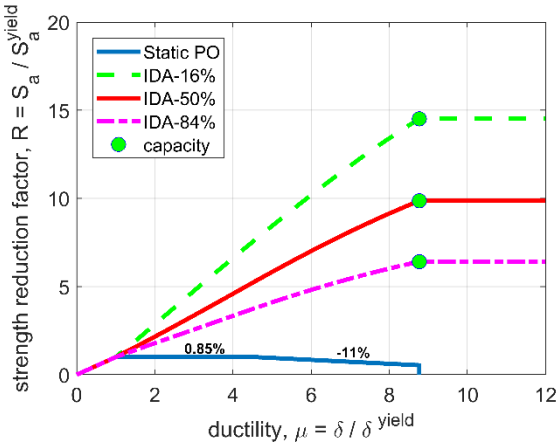
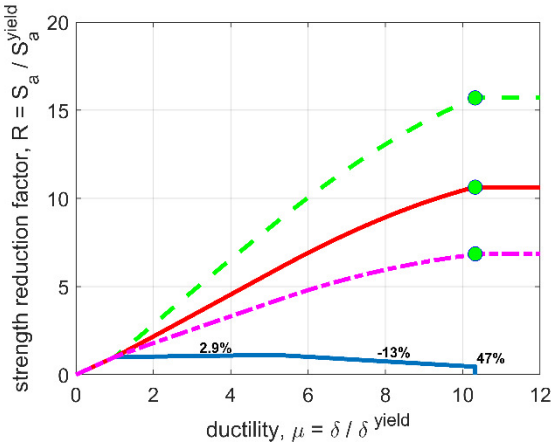


Figure 6.7: SPO2IDA for the 10-storey uncoupled (10S-U) building: $R_d = 2$

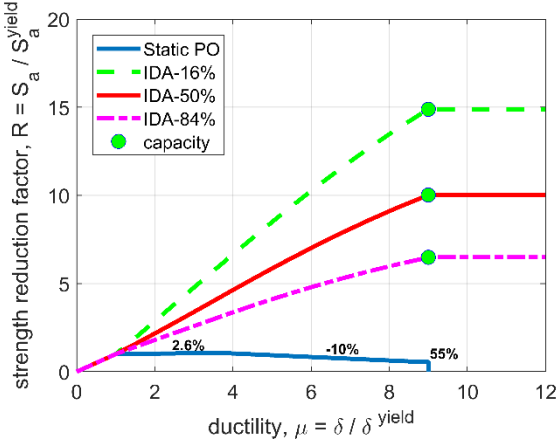
**Figure 6.8:** SPO2IDA for the 10-storey uncoupled (10S-U) building: $R_d = 3$ **Figure 6.9:** SPO2IDA for the 15-storey coupled (15S-C) building: $R_d = 2$ **Figure 6.10:** SPO2IDA for the 20-storey coupled (20S-C) building: $R_d = 2$



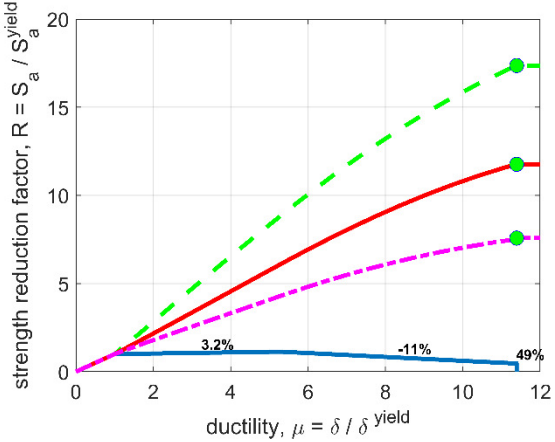
(a) X-direction



(b) Y-direction

Figure 6.11: SPO2IDA for the 20-storey coupled (20S-C) building: $R_d = 3$ 

(a) X-direction



(b) Y-direction

Figure 6.12: SPO2IDA for the 20-storey coupled (20S-C) building: $R_d = 4$

In SPO2IDA, instead of spectral acceleration, we have a normalized intensity factor by R. This is equal to the applied spectral acceleration normalized by the spectral acceleration value corresponding to yield. The definition of the R factor is similar as in the force-based design (FBD) procedure. In the FBD method, the R factor corresponds to the reduction in the linear-elastic demand, based on the available ductility in the system. Similarly, in SPO2IDA, the R factor is the ratio of the seismic intensity to the intensity leading to yielding of the (already defined) system.

Table 6.1: preliminary CMR values of the 10- and 20-storey building based on SPO2IDA

Building ID	R_d	$R_{50\%}$	$CMR_{SPO2IDA}$
10S-U	2	4.5	2.25
	3	5.5	1.83
15S-C	2	6.7	3.35
20S-C	2	8.9	4.45
	3	9.9	3.29
	4	10.0	2.51

The approximate collapse margin ratio values from SPO2IDA are obtained as:

$$CMR_{SPO2IDA} = \frac{R_{50\%}}{R_d} \quad 6.4$$

where $R_{50\%}$ = median collapse curve from the SPO2IDA analysis and R_d = ductility factor used in the design. The over-strength factor R_o is largely included in the yield force value of the trilinear approximation used in the SPO2IDA analysis and as a result it is not included in the denominator of Eq. 6.4. Table 6.1 summarizes the preliminary CMR values obtained from the SPO2IDA results presented in Figures 6.7 to 6.12. In Table 6.1, the $R_{50\%}$ and CMR values illustrated correspond to the most critical among the two horizontal directions.

Figures 6.13 to 6.15, respectively, show the ISDR profiles along building height for the 10S-U, 15S-C and the 20S-C buildings corresponding to SPO first yield (hold-down yield at the first floor) and collapse (ISDR = 5%). The 10S-U and 15S-C building response is dominated by bending deformations, i.e. the ISDR increases from bottom to top. With the addition of the link-beams in the 20S-C building, the interaction between wall bending and shear response leads to an ISDR profile attaining maximum values at the mid-stories.

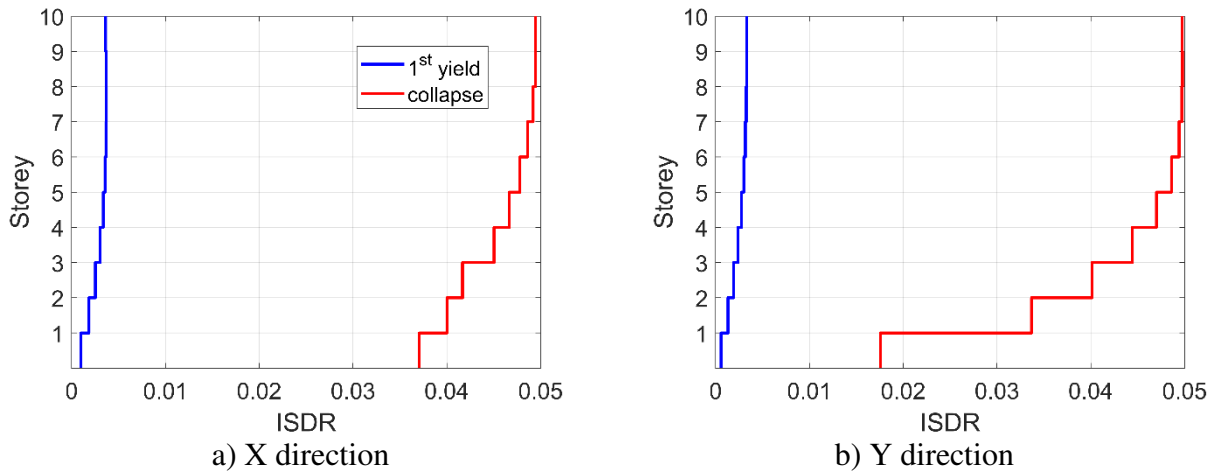


Figure 6.13: ISDRs for the 10-storey uncoupled (10S-U) building: $R_d = 2$

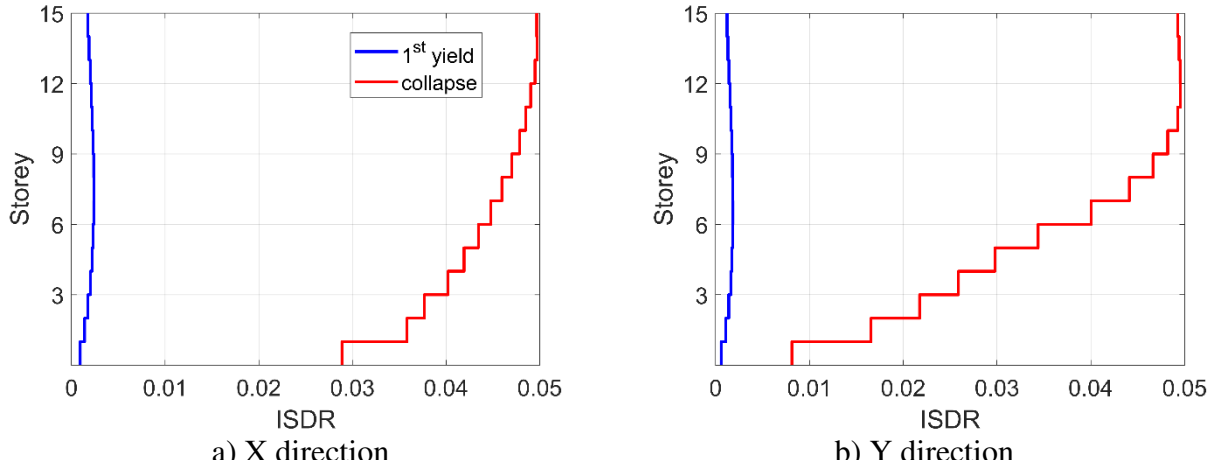


Figure 6.14: ISDRs for the 15-storey-coupled (15S-C) building: $R_d = 2$

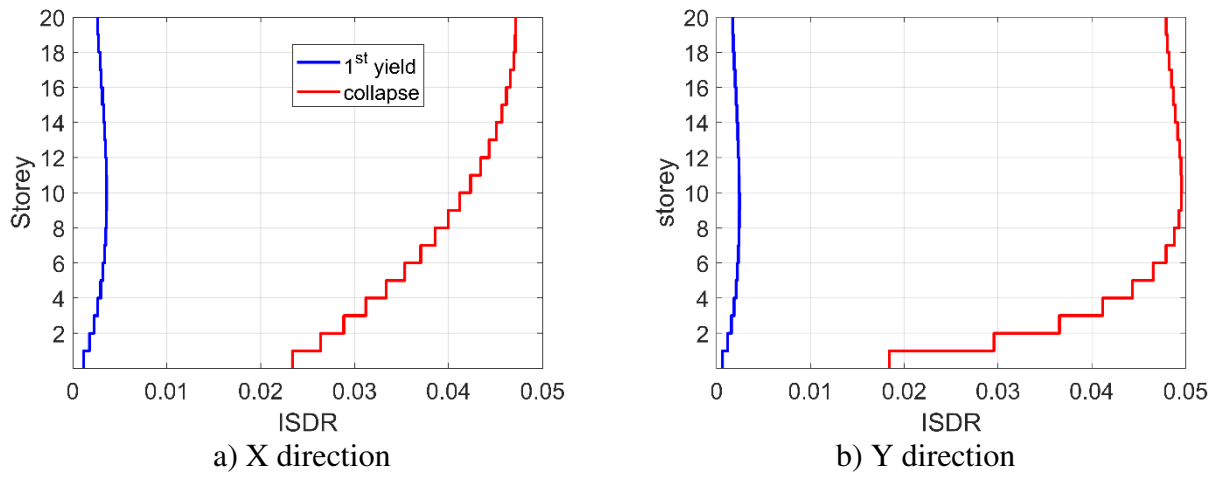


Figure 6.15: ISDRs for the 20-storey-coupled (20S-C) building: $R_d = 2$

Chapter 7 Seismic Hazard for Vancouver and Ground Motion Selection

7.1 Introduction

Canada is a large country with diverse seismic hazards – active crustal and subduction earthquakes in the west versus stable continental intraplate earthquakes in the east. Historically, different types of earthquakes contributed to earthquake disasters in Canada (Cassidy et al., 2010). In western Canada, historical records/experiences of major seismicity are limited due to a short history of human settlements. Major earthquakes include the 1918 (M6.9) and 1946 (M7.3) earthquakes in Vancouver Island, and the 2001 (M6.8) Nisqually earthquake in Washington (Cassidy et al., 2010). One of the major concerns is the Cascadia subduction event in Pacific Northwest, which can result in a magnitude exceeding 9. Figure 7.1 shows regional seismicity in south-western British Columbia, exhibiting four different contributing seismic sources: *shallow crustal events* on Vancouver Island and underneath Vancouver, *deep inslab earthquakes* in Puget Sound and underneath Seattle, offshore events west of Vancouver Island, and *mega-thrust subduction interface events* from the Cascadia subduction zone (indicated by grey line segments). Among these, crustal, inslab, and interface earthquakes contribute most significantly to site-specific seismic hazards in south-western British Columbia (Halchuk et al., 2016). Hence, Greater Vancouver, which is vital to the stable economic growth in south-western British Columbia, is situated in a high seismic region in Canada and seismic risk to existing building stock is a major concern.

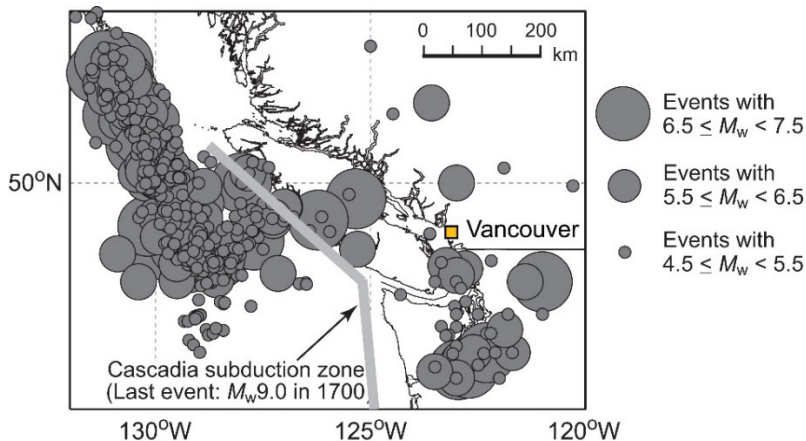


Figure 7.1: Regional seismicity in south-western British Columbia, Canada

The Geological Survey of Canada (GSC) produces national seismic hazard maps of Canada for seismic design provisions of the National Building Code of Canada (Atkinson and Adams, 2013;

Humar, 2015). The current seismic hazard maps are the 5th generation. The input seismic hazard model parameters, such as seismic source models, regional seismicity models, and ground motion (GM) models, are provided by Halchuk et al. (2014), and the computed site-specific seismic hazard values at eight return period levels are provided by Halchuk et al. (2015, 2016). The calculated values are for the reference site condition, which is represented by the average shear-wave velocity in the uppermost 30 m (V_{s30}) of 450 m/s. Although seismic hazard values at 10-km grid locations across the entire Canada are available, the current publicly accessible databases of the seismic hazard values and maps are not sufficient for performing advanced seismic analyses and risk assessments of buildings and infrastructure. For instance, detailed selection of GM records is necessary by reflecting seismic disaggregation information to conduct a series of nonlinear dynamic analyses (Goda and Atkinson, 2011), whereas quantitative seismic loss estimation can be facilitated by the use of synthetic earthquake catalogs (Tesfamariam and Goda, 2015). To enable such advanced earthquake engineering applications, an in-house probabilistic seismic hazard analysis (PSHA) tool is developed based on the 2015 GSC seismic hazard model. This chapter describes the key features of the implementation of the 2015 GSC seismic hazard model and the main results of the developed tool. The results are compared with the seismic hazard values provided by Halchuk et al. (2015, 2016).

In developing seismic fragility models of a building via nonlinear dynamic analysis, it is important to select a suitable set of GM records that reflect seismic environments of the region. GM records can be selected in various ways. One of the standard approaches for GM record selection is to identify a suite of GM records, response spectra of which match with a target response spectrum at a site of interest. A popular choice in defining the target response spectrum is the conditional mean spectrum (CMS; see Baker [2011]), which is a modified uniform hazard spectrum (UHS) that is usually derived for seismic building code purposes (e.g. Halchuk et al., 2014, 2015). More specifically, the CMS is obtained by conditioning that the response spectral ordinates of the UHS and the CMS match at the anchor vibration period and by accounting for correlations of response spectral ordinates at different vibration periods. For the case of multiple major seismic sources contributing to the overall seismic hazard (like a situation for Vancouver), multiple target CMS need to be considered and GM records need to be selected from suitable GM record pools that possess key features of the seismic sources (e.g. magnitude, frequency content, and duration). The number of records selected from individual record pools should also reflect the proportions of seismic hazard contributions from these seismic sources; event-type specific hazard contributions can be obtained via seismic disaggregation. Such a multiple-event-based CMS record selection method has been developed by Goda and Atkinson (2011), and has been successfully implemented

for several studies/investigations of developing seismic fragility functions for buildings (e.g. Tesfamariam and Goda, 2015).

This chapter summarizes a GM record selection procedure that is adopted for four tall wood-concrete hybrid buildings in Vancouver, which have different storey numbers and structural configurations. The building models 10S-U and 15S-U are based on uncoupled structural systems, where the central core shear walls made of cross-laminated-timber (CLT) are disconnected, whereas the building models 15S-C and 20S-C couple the CLT shear walls through reinforced concrete link. The main building characteristics of the four buildings are summarized in Table 7.1. Because of structural flexibility of the building systems, the first-mode vibration periods, which are typically considered as the anchor vibration period in deriving the CMS, are relatively long, ranging from 2.5 s to 5.5 s. The first three fundamental $T_1 - T_3$ is used for the record selection and scaling for seismic performance assessment. In addition, the limiting vibration periods T_{min} and T_{max} are defined for each storey class such that the first three vibration periods fall within the specified range. This range is used when response spectrum matching of candidate records with the target response spectrum is carried out (see Section 7.2). The three modal shapes are shown in Figures 7.2a and 7.2b for the 10-storey uncoupled and 20-storey-coupled buildings, respectively.

Table 7.1: First three fundamental periods of four buildings

Building ID	Building	Mode 1 (sec)	Mode 2 (sec)	Mode 3 (sec)	T_1 (sec)	[T_{min} , T_{max}] (sec)
10S-U	10-storey (Uncoupled)	2.71	1.89	1.48	2.5	[0.1, 5]
15S-C	15-storey (Coupled)	2.71	1.98	1.90	2.5	[0.1, 5]
20S-C	20-storey (Coupled)	3.56	2.78	2.61	3.5	[0.1, 5]

The record selection method that is implemented in this study is an improved version of the multiple-event-based CMS record selection method of Goda and Atkinson (2011). The major extended components of the method include:

- The underlying seismic hazard model is based on the 2015 version of the national seismic hazard model of Canada (Halchuk et al., 2014, 2015). An in-house PSHA tool has been developed using MATLAB. It can reproduce the seismic hazard values at sites in south-western British Columbia with approximately 5% differences or less. The PSHA tool produces detailed seismic disaggregation results, which are not available from the GSC at the time of this writing, and thus facilitates the implementation of the multiple-event-based CMS record selection method.
- GM records of interest for this study are those of mainshock-aftershock sequences. Therefore, selected GM records can be employed to quantify the effects of repeated earthquake load sequences on seismic performances of buildings by developing seismic fragility models using real mainshock-aftershock record sequences (e.g. Tesfamariam and Goda, 2015). The record selection of the mainshock-aftershock sequences is carried out by focusing upon mainshock records within the sequences by matching the key features of the target response spectra.

- To establish larger GM record pools of real mainshock-aftershock sequences that are originated from different earthquake types, a database that was considered by Tesfamariam and Goda (2015) has been expanded by including all mainshock-aftershock sequence data from the PEER-NGA database (172 sequences rather than a limited suite of 75 sequences, as considered by Goda and Taylor (2012)) and by including the new data from the 2016 Kumamoto Japan earthquake sequences (Goda et al., 2016). The expanded database of the real mainshock-aftershock records contains: 172 sequences from the PEER-NGA database, 531 sequences from the Japanese K-NET, KiK-net, and SK-net (KKiKSK) databases, and 28 sequences for the 2016 Kumamoto earthquakes from the Japanese K-NET and KiK-net databases – in total, there are 731 sequences, in comparison with the 606 sequences as previously considered in Tesfamariam and Goda (2015).

In the following, main steps of the multiple-event-based CMS record selection for real mainshock-aftershock sequences are described by considering the four wood-concrete hybrid buildings located in Vancouver. The coordinate location of Vancouver is [49.266°N, 123.150°W], and the surface ground condition for this site is the reference ground condition (i.e. Site Class C) as in the 2015 national seismic hazard maps of Canada, which is represented by the average shear-wave velocity in the uppermost 30 m of $V_{s30} = 450$ m/s.

7.2 Seismic hazard in Vancouver

The multiple-event-based CMS GM selection requires detailed information of seismic hazard characteristics of contributing sources. The necessary inputs in defining the target CMS and in selecting an appropriate set of GM records are the UHS corresponding to a return period level (e.g. 1 in 2500 years) and the seismic disaggregation results. The latter is employed to specify plausible earthquake scenarios in terms of mean magnitude and mean distance and to estimate proportions of seismic hazard contributions from different types of earthquakes. Although the site-specific UHS values at numerous locations in Canada are available from Halchuk et al. (2014, 2015; see Figure 7.2), detailed seismic disaggregation results are generally unavailable. The seismic hazard values provided by the GSC are UHS values for peak ground velocity (PGV), peak ground acceleration (PGA), and 5%-damped pseudo-spectral accelerations (SA) at periods of 0.05, 0.1, 0.2, 0.3, 0.5, 1, 2, 5, and 10 seconds at six return periods (TR) of 100, 225, 476, 1000, 2000, and 2475 years. For the seismic building code purposes, UHS values corresponding to the return period of 2475 years are adopted.

The in-house PSHA tool is based on Monte Carlo simulations (Atkinson and Goda, 2013), and implements all major components of the national seismic hazard model as described in Halchuk et al. (2014). The differences of the calculated seismic hazard values can result from differences in how numerical evaluations are performed – the in-house tool evaluates seismic hazard integration via Monte Carlo simulations by utilizing a synthetic earthquake catalog, whereas the GSC seismic

hazard tool uses numerical integration by discretizing main variables of seismic hazard analysis (e.g. earthquake magnitude, spatial source zone, and GM prediction variability). For the in-house PSHA tool, the length of the synthetic earthquake catalog is set to 50 million years. At the return period of 2475 years, the differences of the UHS values between the GSC and the in-house simulations are less than 2%.

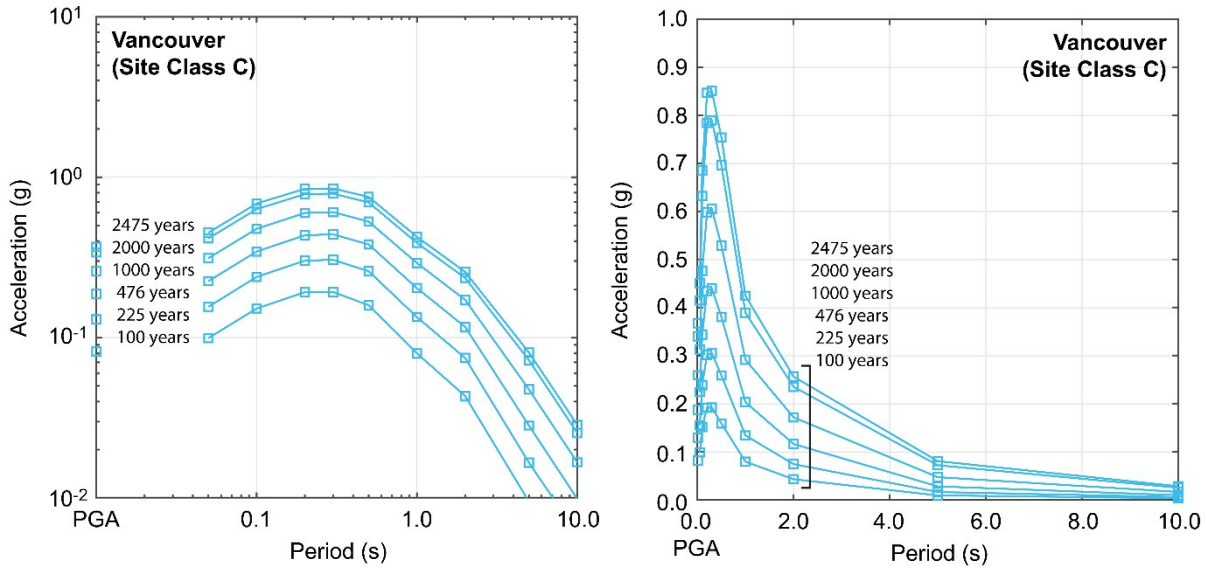


Figure 7.2: Uniform hazard spectra for Vancouver (Halchuk et al., 2014, 2015)

To evaluate the accuracy of the in-house PSHA tool and investigate the seismic hazard contributions from different sources, seismic hazard curves for three types of earthquakes, i.e. crustal, interface, and inslab, are obtained from the in-house PSHA tool, and are compared with the seismic hazard values provided by Halchuk et al. (2016). Figure 7.3 shows such comparisons for PGA and SA at 0.2, 1, 2, 5, and 10 s. It can be observed that at short vibration periods (PGA and SA at 0.2 s), dominant seismic sources are inslab and crustal events. With the increase in vibration period, seismic contributions of the interface events (mainly due to the M8.5+ Cascadia subduction events) increase drastically (particularly between 2 s and 5 s). In Figure 7.3, it is also noticed that at the return periods less than 500 years (i.e. annual probability greater than 0.002) the interface hazard values for the in-house tool deviate from those for the GSC's results. The interface hazard values at these return period levels are mainly contributed by the Explorer Interface Source and the Winona Thrust Fault Source (as defined in Halchuk et al., 2014), which are modeled as finite-fault seismic sources rupturing typically in M7 events at farther distances from Vancouver. The latter source cuts cross the boundary of seismic hazard calculations (i.e. 400 km radius from a site of interest) adopted by the GSC, and it is unclear how such a hazard boundary is implemented in the GSC seismic hazard model. In the in-house seismic hazard model, all events that originate from the Winona Thrust Fault Source are included in the calculations (even if epicentral distances

are greater than 400 km) and some discrepancy in the calculated hazard values is expected. It is noteworthy that these differences do not affect overall seismic hazard values at the long return period levels for Vancouver because these are distant seismic events (although magnitudes are relatively large).

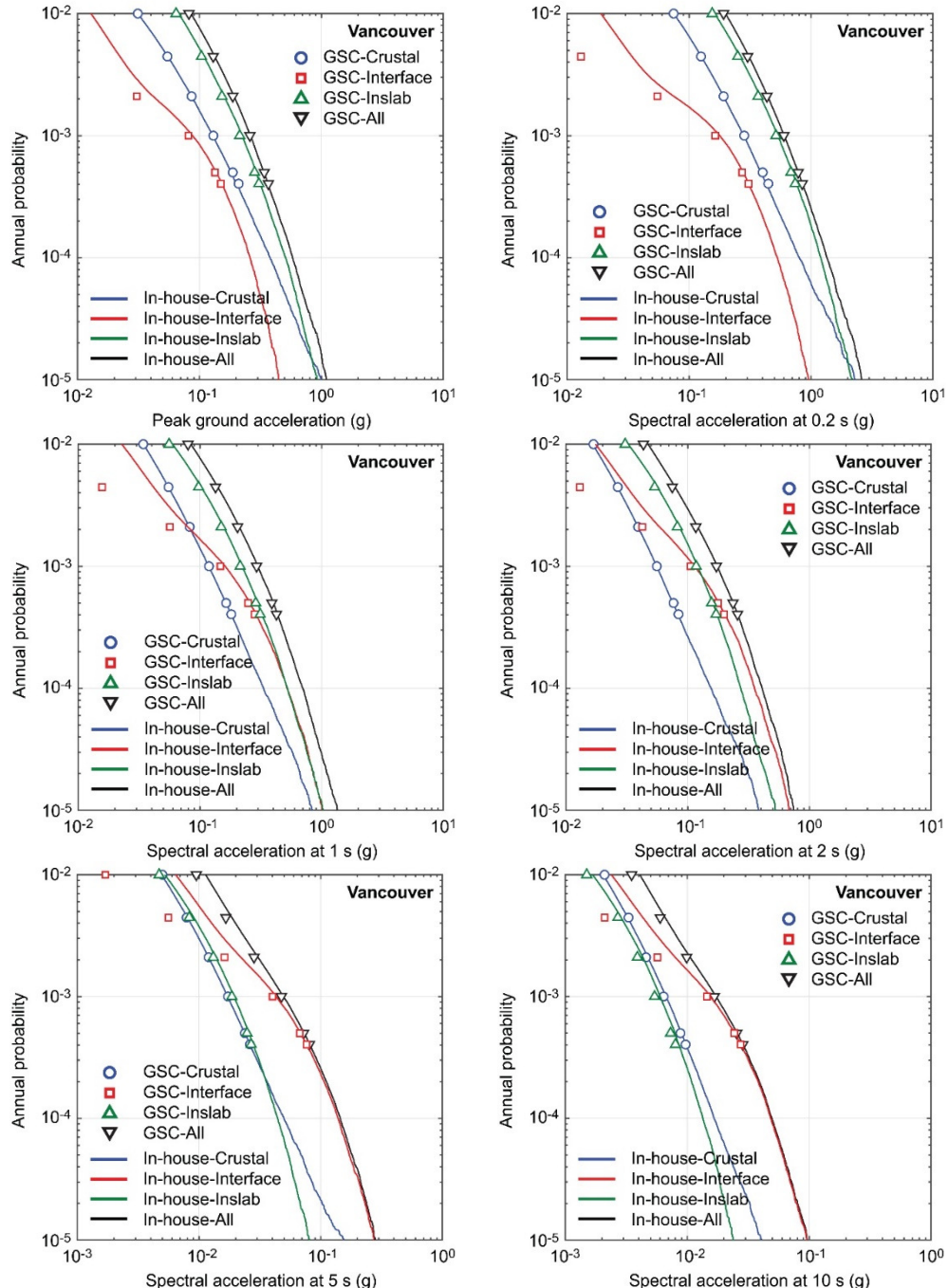


Figure 7.3: Seismic hazard curves for Vancouver by distinguishing three contributing seismic sources

Using the simulated seismic hazard values, seismic disaggregation can be performed (Atkinson and Goda, 2013). The results for spectral acceleration at 2 and 5 seconds are shown in Figure 7.4. It is noted that the vibration periods of 2 and 5 seconds are most relevant for the four hybrid

buildings listed in Table 7.1. The seismic disaggregation is performed by considering 5000 data that closely match the UHS values of interest. The seismic disaggregation results distinguish earthquake event types – i.e. crustal, interface, and inslab events, which have distinct characteristics in terms of earthquake magnitude and distance. This means that different scenario characteristics should be used for the record selection. It is also important to note that the proportions of seismic hazard contributions for SA at $T = 2$ s and for SA at $T = 5$ s differ significantly. For SA at $T = 2$ s (and shorter vibration periods), both inslab and interface earthquakes have dominant influence on the calculated seismic hazards, whereas for SA at $T = 5$ s, interface events become single dominant source (more than 85% contributions). This drastic change is due to the characteristics of GM models for inslab and interface earthquakes (Atkinson and Adams, 2013), where GMs for inslab events generally lack low-frequency spectral content while those for interface events maintain rich spectral content in the low-frequency range. The consideration of the most recent seismic hazard model facilitates the incorporation of the up-to-date knowledge in the record selection process (and thus this effect is included in the developed seismic fragility models).

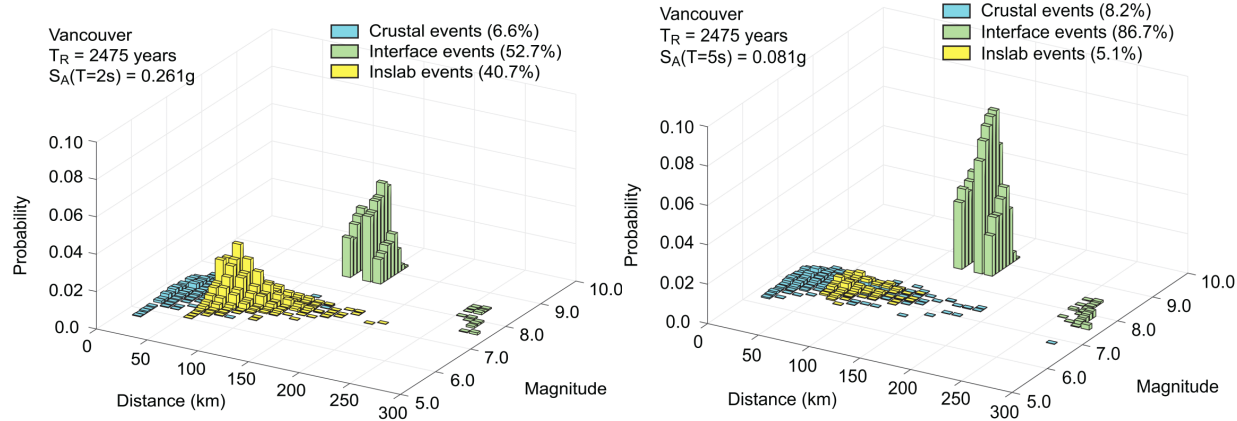


Figure 7.4: Seismic disaggregation for Vancouver – $TR = 2475$ years and for $SA(T = 2\text{ s})$ and $SA(T = 5\text{ s})$

7.3 Ground motion database for real mainshock-aftershock records

The input GM records for the four structural models of the tall wood-concrete hybrid buildings are for mainshock-aftershock sequences. To meet such requirements, an expanded GM database for the real mainshock-aftershock sequences is developed. The compiled database is based on the previous databases of Goda and Taylor (2012) and Goda et al. (2015) (see also Tesfamariam and Goda [2015]), and is expanded by including 97 records from the 1999 Chi-Chi earthquake sequence that were excluded in Goda and Taylor (2012) and 28 records from the 2016 Kumamoto earthquake sequence (Goda et al., 2016), resulting in 731 sequences.

Figure 7.5 shows the magnitude-distance distributions of the mainshocks and major aftershocks of the newly compiled database by distinguishing earthquake types, whereas Figure 7.6 shows a histogram of average shear-wave velocity at recording sites. Among the 731 sequences, 266, 340, and 125 sequences are classified as shallow crustal, mega-thrust interface, and deep inslab events, respectively. By inspecting record features of the mainshocks and major aftershock records in Figure 7.5, it is observed that the magnitudes of the major aftershocks are typically smaller than those of the mainshocks (as empirically evidenced in Bath's law; see Shchervakov et al. [2013]). The interface records that are contained in the database are based on the two recent major subduction earthquakes, i.e. M8.3 2003 Tokachi earthquake and M9.0 2011 Tohoku earthquake in Japan. It is also noteworthy that all subduction earthquake records (either inslab or interface) are from Japan. In this sense, other global subduction records, such as Chile and New Zealand, are not included. The issue related to possible dominant influence of GM records from Japan may be mitigated when actual record selection is conducted using the multiple-event-based CMS method. This is because the target CMS for different earthquake types are derived from the detailed PSHA results and their amplitudes as well as frequency content are based on the current knowledge of regional seismicity and GM characteristics that are deemed to be applicable to south-western British Columbia. Nonetheless, it is important to be cautious about the potential bias due to the fact that GM databases are not directly based on those for south-western British Columbia.

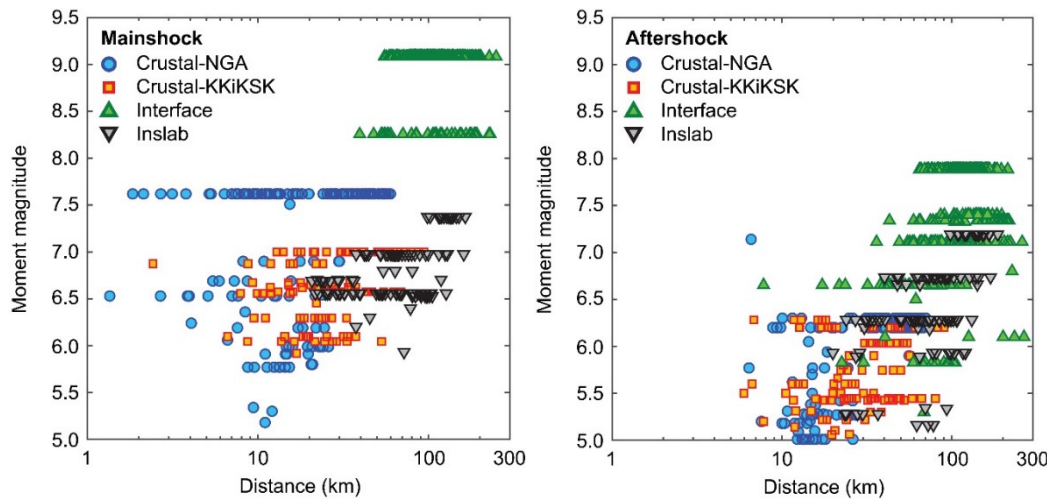


Figure 7.5: Magnitude–distance distribution of mainshock records and major aftershock records of the GM database

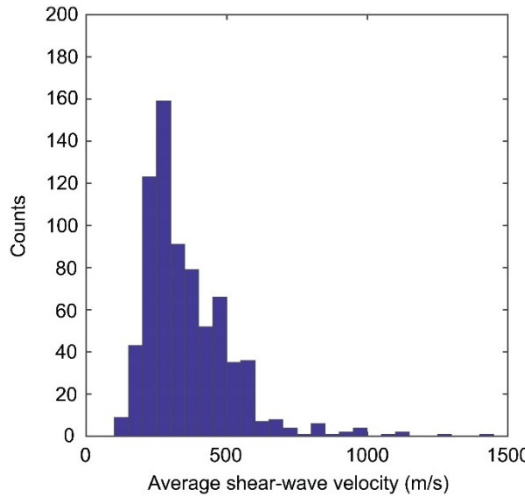


Figure 7.6: Histogram of average shear-wave velocity at recording sites of the GM database

7.4 Record selection of mainshock-aftershock sequence records for tall wood-concrete hybrid structural systems

Based on the updated regional seismic hazard information and the mainshock-aftershock GM record database, the multiple-event-based CMS record selection is conducted for the four hybrid structures. This is implemented as follows:

- The return period TR and the number of GM record sequences N are selected to be 2475 years and 50, respectively. It is noted that each sequence contains two horizontal components.
- For each structural system, firstly the anchor vibration period TA is selected based on the first-mode vibration period and the availability of seismic hazard information from PSHA (see Table 7.1). TA is set to the closest tenth decimal value. In addition, by taking into account vibration periods corresponding to higher modes, the vibration period range for matching the response spectral values of candidate records and the target response spectrum, T_{\min} and T_{\max} , are selected. The selected values of $[T_{\min}, T_{\max}]$ for the four structural systems are also indicated in Table 7.1.
- Next, mean earthquake scenarios in terms of magnitude and distance and seismic hazard contributions for three earthquake types are obtained from the detailed PSHA results for Vancouver (e.g. Figures 7.3 to 7.6). When the seismic hazard information at TA is not directly available, PSHA results are interpolated based on results at two adjacent vibration periods (i.e. for the 10S-U, 15S-C, and 20S-C models, PSHA results at $T = 2$ and 5 s are used).
- Using the hazard information and GM models used for the PSHA calculations (see Atkinson and Adams [2013] and Halchuk et al. [2014]), CMS are obtained for three earthquake types.
- For each earthquake type, the required number of GM records is calculated by considering N as well as seismic hazard contribution from the seismic disaggregation result (e.g. for N = 50 and TA = 5 s, 4, 43, and 3 sequences are selected for crustal, interface, and inslab events; see Figure 7.4). Subsequently, the fitness of candidate GM record sequences is evaluated by computing the sum of differences of the response spectral ordinates and the target response spectrum over the vibration period range between T_{\min} and T_{\max} in logarithmic scale, and records that have the smaller total logarithmic differences are selected. It is noted that the record selection of candidate records is carried out based on the geometric mean of the two horizontal components of the mainshock record. In matching response spectral ordinates, the record amplitude scaling at the anchor vibration period up to a factor of 5 is permitted (i.e.

excessive record scaling is prohibited). This procedure is repeated for all three earthquake types.

To demonstrate the above-mentioned record selection procedure, the comparisons of the UHS for TR = 2475 years and three CMS for crustal, interface, and inslab events are shown in Figure 7.7. In the figures, the anchor vibration periods are indicated with vertical broken lines, and 16th and 84th percentile CMS are also included. An important observation is that response spectral shapes of the three CMS are different, particularly for interface events having richer low-frequency spectral content, compared with the other two.

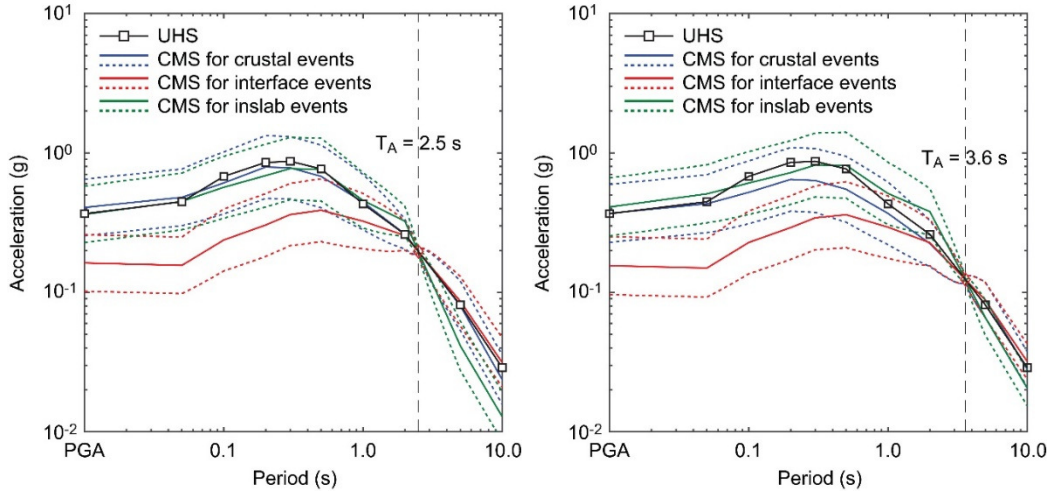


Figure 7.7: Comparison of uniform hazard spectrum and conditional mean spectra for crustal, interface, and inslab records

Subsequently, record selection is performed using the target CMS and the compiled GM database for real mainshock-aftershock sequences. In Figures 7.8 and 7.9 comparisons of the response spectra of the selected records (mainshocks) and the target CMS (together with the 16th and 84th percentile CMS) are presented for T = 2.5 s (used for the 10S-U and 15S-C) and T = 3.6 s (used for 20S-C), respectively. The comparisons for all event types as well as individual event types are included. The vibration period range $T_{\min} = 0.1$ s and $T_{\max} = 5.0$ s considered for computing the fitness of candidate records is also indicated in the figures. Overall, the match of the selected records to the target CMS are satisfactory within the vibration period range between T_{\min} and T_{\max} .

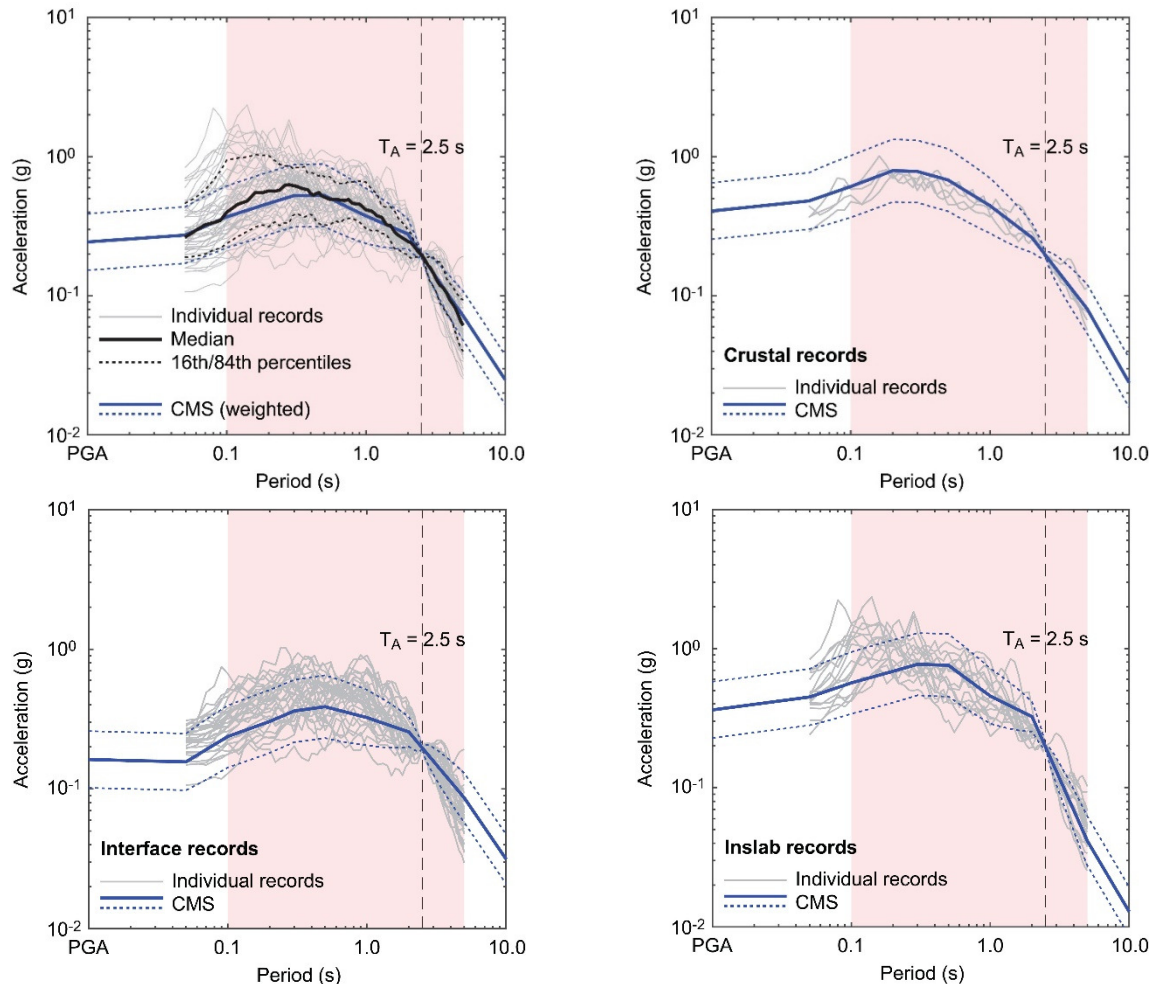


Figure 7.8: Comparison of the response spectra of the selected records with the target response spectrum for $T = 2.5$ s

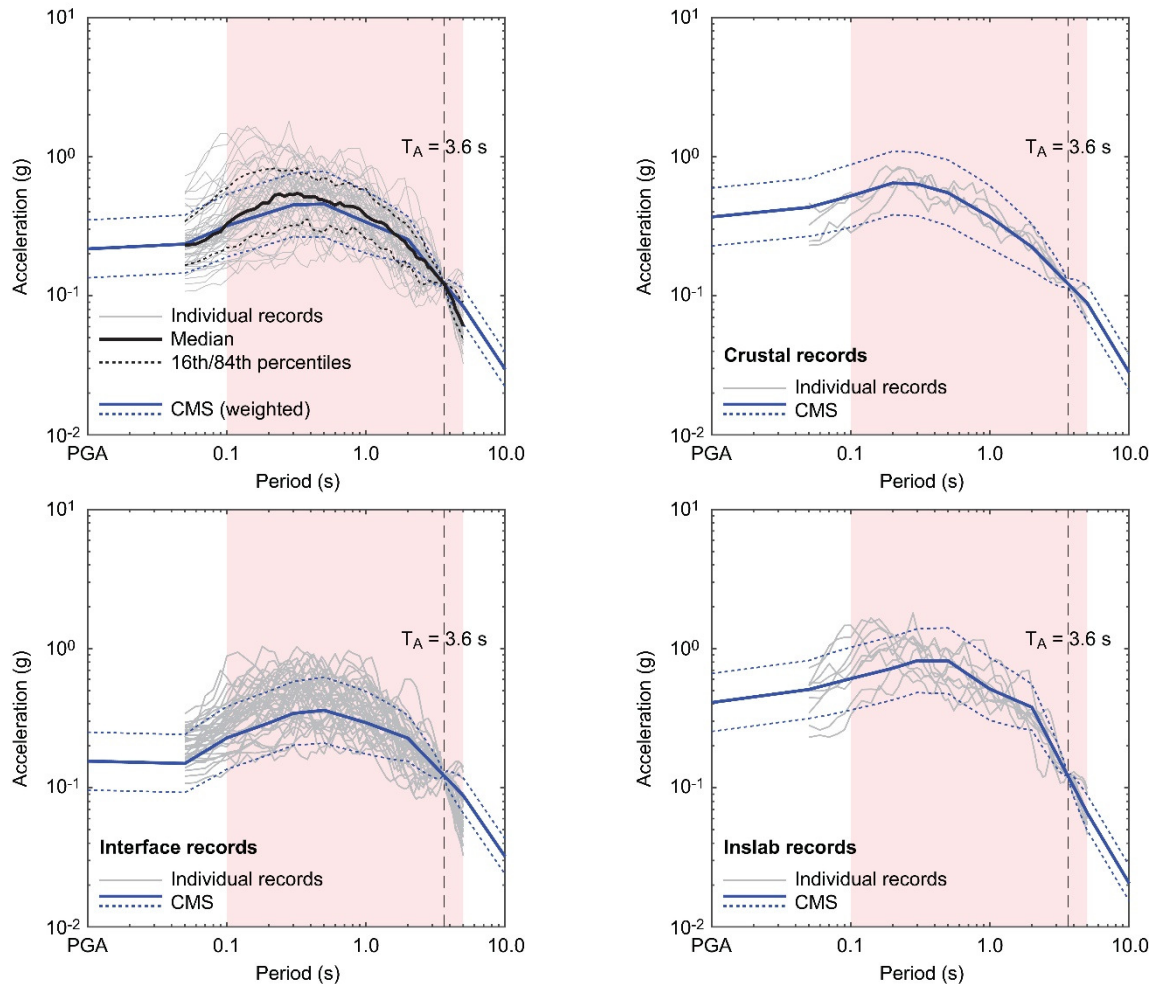


Figure 7.9: Comparison of the response spectra of the selected records with the target response spectrum for $T = 3.6$ s

Chapter 8 Validation of Proposed R_d and R_o Factors

This chapter presents the performance evaluation for the R_d and R_o factors considered. This evaluation process includes collapse risk assessment using: static pushover to IDA analysis (SPO2IDA) (Chapter 6), dynamic nonlinear time history analyses (NLTHA) and Incremental Dynamic Analysis (IDA) (Vamvatsikos and Cornell 2002).

8.1 Check for collapse prevention limit state according to NBCC 2015

NLTHA has been conducted using 15 GM records (i.e., 15 records, 2 components each) with 2% probability of exceedance in 50 years. The NBCC 2015 collapse prevention performance limit state is maximum inter-storey drift ratio (*MISDR*) = 2.5%. For the 10S-U, the interstorey drift demand in the Y (critical) direction and along the height of the building are presented in Figure 8.1a ($R_d = 2$ and $R_o = 1.5$) and Figure 8.1b ($R_d = 3$ and $R_o = 1.5$). In order to check the upper bound requirement, in the given figures, mean plus one standard deviation (SD) plots are also included. The gray lines in the figures represent the response of buildings under individual earthquake GM records. It is evident from Figure 8.1 that the mean *MISDR* demands are less than 2.5%. However, the mean + 1SD demands exceeds the 2.5% *MISDR* limit for $R_d = 3$. With this preliminary analysis, the $R_d = 2$ and $R_o = 1.5$ are suitable and efficient from the collapse prevention limit state requirement of NBCC 2015. For the different structural system, this analysis will be further extended and collapse risk using IDA will be quantified.

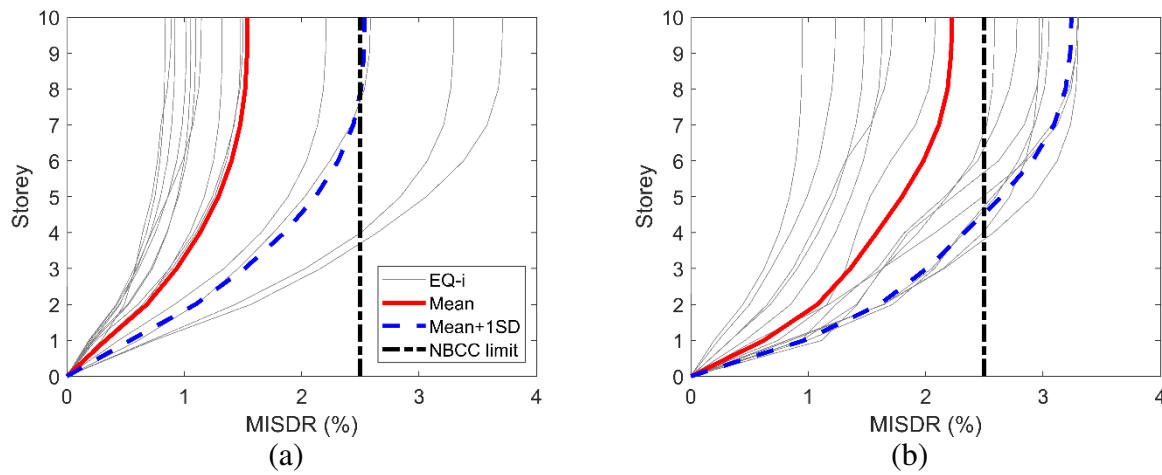


Figure 8.1: Maximum inter-storey drift ratios for 2% in 50 years return period (design-based earthquake GMs) for 10S-U building, a) $R_d = 2$, and b) $R_d = 3$

Figure 8.2 shows the story demands of *MISDR* in the Y direction for the 15S-C and 20S-C buildings and for $R_d = 2$. It is evident that the drift demands for the design earthquake are well below the NBCC limit of 2.5% *MISDR*. This improvement can be partly explained by the addition of the coupling beams, which add stiffness to the system.

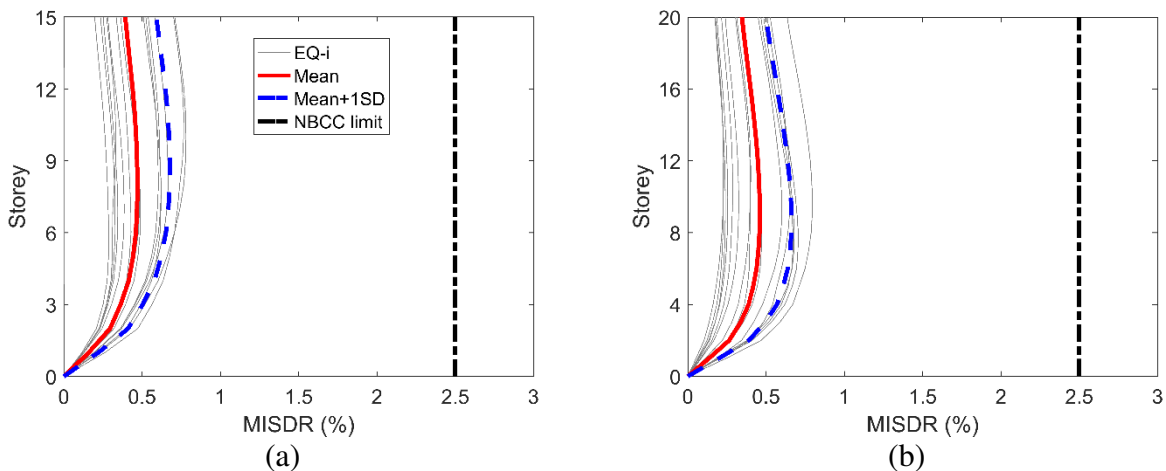


Figure 8.2: Maximum inter-storey drift ratios for 2% in 50 years return period (design-based earthquake GMs) for $R_d = 2$, a) 15S-C and b) 20S-C buildings

8.2 FEMA P695 collapse risk performance evaluation

To verify acceptability of the R_d and R_o factors, FEMA P695 suggests the use of IDA to obtain the collapse fragility and collapse margin ratio (*CMR*). The collapse fragility curves are modelled as a lognormal distribution, and defined by the median collapse intensity (\hat{S}_{CT}) and standard deviation of natural logarithm (β_{RTR}). Moreover, FEMA P695 defined β_{RTR} to be a dispersion of IDA results due to the variability within GM records. Due its insignificance on the final *CMR*, FEMA P695 suggests a constant value of $\beta_{RTR} = 0.4$ for structures with period based ductility ($\mu > 3$). The collapse margin ratio *CMR* is computed as:

$$CMR = \frac{\hat{S}_{CT}}{S_{MT}} \quad \textbf{8.1}$$

where S_{MT} = spectral acceleration value at the fundamental period of the archetype structure under consideration. Once the CMR of each archetype is calculated, FEMA P695 adjusts this value to Adjusted Collapse Margin Ratio ($ACMR$) to account for the Spectral Shape Factor (SSF):

$$ACMR = SSF_i CMR_i$$

In this research, the GMs were selected and scaled for each archetype model based on their spectral acceleration values at the fundamental period of the considered archetype building. Therefore, SSF was set to 1, i.e. $ACMR_i = CMR_i$. In order to accurately calculate the safety against collapse, FEMA P695 considers more sources of uncertainties. The following set of bullets describes the considered system uncertainties.

- Design requirement uncertainty (DR): according to FEMA P695, this type of uncertainty is related to the robustness and completeness of design requirements of the archetype buildings. Table 8.1 summarizes quantitative the factors to consider to quantify the uncertainty as the lognormal standard deviation parameter (θ_{DR}). This is assessment done qualitatively, based on completeness of the information and confidence in the basis of design requirement.

Table 8.1: Quality rating of design requirements (FEMA 2009)

Confidence in Basis of Design Requirements			
Completeness and Robustness	High	Medium	Low
High. High. Extensive safeguards against unanticipated failure modes. All important design and quality assurance issues are addressed.	(A) Superior $\beta_{DR} = 0.1$	(B) Good $\beta_{DR} = 0.2$	(C) Fair $\beta_{DR} = 0.35$
Medium. Reasonable safeguards against unanticipated failure modes. Most of the important design and quality assurance issues are addressed.	(B) Good $\beta_{DR} = 0.2$	(C) Fair $\beta_{DR} = 0.35$	(D) Poor $\beta_{DR} = 0.5$
Low. Questionable safeguards against unanticipated failure modes. Many important design and quality assurance issues are not addressed.	(C) Fair $\beta_{DR} = 0.35$	(B) Poor $\beta_{DR} = 0.5$	—

- Test data uncertainty (TD): uncertainty related to the quality of test data to calibrate and model the archetype buildings. Table 8.2 summarizes quantitative values of this uncertainty, as the lognormal standard deviation parameter (β_{TD}), based on the rating of quality of the test data.

Table 8.2: Quality rating of test data from an experimental investigation program (FEMA 2009)

Confidence in Test Results			
Completeness and Robustness	High	Medium	Low
High. Material, component, connection, assembly, and system behaviour well understood and accounted for all, or nearly all, important testing issues addressed	(A) Superior $\beta_{TD} = 0.1$	(B) Good $\beta_{TD} = 0.2$	(C) Fair $\beta_{TD} = 0.35$
Medium. Material, component, connection, assembly, and system behaviour generally understood and accounted for most important testing issues addressed.	(B) Good $\beta_{TD} = 0.2$	(C) Fair $\beta_{TD} = 0.35$	(D) Poor $\beta_{TD} = 0.5$
Low. Material, component, connection, assembly, and system behaviour fairly understood and accounted for Several important testing issues not addressed.	(C) Fair $\beta_{TD} = 0.35$	(D) Poor $\beta_{TD} = 0.5$	—

- Modeling uncertainty (MDL): uncertainty related to the accuracy, robustness and quality of the numerical models to capture seismic response and simulate the collapse mechanism of archetype buildings. Table 8.3 summarizes quantitative values of this uncertainty based on the rating of quality of the proposed numerical models as the lognormal standard deviation parameter (β_{MDL}). More information can be obtained from FEMA P695.

Table 8.3: Quality rating of index archetype models

Confidence in Basis of Design			
Completeness and Robustness	High	Medium	Low
High. Index models capture the full range of the archetype design space and structural behavioral effects that contribute to collapse.	(A) Superior $\beta_{MDL} = 0.1$	(B) Good $\beta_{MDL} = 0.2$	(C) Fair $\beta_{MDL} = 0.35$
Medium. Index models are generally comprehensive and representative of the design space and behavioral effects that contribute to collapse.	(B) Good $\beta_{MDL} = 0.2$	(C) Fair $\beta_{MDL} = 0.35$	(D) Poor $\beta_{MDL} = 0.5$
Low. Significant aspects of the design space and/or collapse behaviour are not captured in the index models.	(C) Fair $\beta_{MDL} = 0.35$	(D) Poor $\beta_{MDL} = 0.5$	—

Based on the above sources of uncertainties, the total uncertainty for the performance evaluation process is obtained by combining RTR, DR, TD, and MDL. This total uncertainty is used to modify the interim fragility curves of each archetype building. The new collapse fragility curve is defined by a random variable (S_{CT}) as:

$$S_{CT} = \hat{S}_{CT} \lambda_{TOT}$$

8.3

where \hat{S}_{CT} = median collapse intensity from IDA and λ_{TOT} is the lognormally distributed random variable with a unit median and standard deviation of β_{TOT} . The λ_{TOT} is computed as (FEMA P695):

$$\lambda_{TOT} = \lambda_{RTR}\lambda_{DR}\lambda_{TD}\lambda_{MDL} \quad 8.4$$

where $\lambda_{RTR}, \lambda_{DR}, \lambda_{TD}, \lambda_{MDL}$ = independent lognormal distributed random variables with medians of unity and standard deviation of $\beta_{RTR}, \beta_{DR}, \beta_{TD}, \beta_{MDL}$, respectively. At this point it is to be noted that the above four random variables are statically independent (their joint probability distribution is the product of their marginal distribution), and the total collapse uncertainty parameter (β_{TOT}) can be calculated as:

$$\beta_{TOT} = \sqrt{\beta_{RTR}^2 + \beta_{DR}^2 + \beta_{TD}^2 + \beta_{MDL}^2} \quad 8.5$$

For record-to-record uncertainty $\beta_{RTR} = 0.4$, FEMA (2009) summarizes the values of β_{TOT} . Acceptable values of adjusted collapse margin ratio of each archetype buildings can be calculated based on the assumption that the collapse value of spectral intensity is a lognormal distributed random variable. This distribution has a median of S_{CT} and lognormal standard deviation of β_{TOT} . By considering β_{TOT} and acceptable collapse probability as 10% and 20%, Table 8.4 summarizes the $ACMR_{10\%}$ and $ACMR_{20\%}$.

FEMA P695 proposed acceptability criteria to verify the adequacy of initially assumed force reduction factors is based on $ACMR_{10\%}$ and $ACMR_{20\%}$. The assumed R_d factors will be accepted if the calculated $ACMR$ ratios within the performance group and individually fulfill the following criterion:

- The calculated Average Adjusted Collapsed Margin Ratio ($ACMR$) within the defined performance group is greater than $ACMR_{10\%}$.

$$\overline{ACMR}_I \geq ACMR_{10\%} \quad 8.6$$

- The calculated individual Adjusted Collapsed Margin Ratio ($ACMR$) of each archetype building is greater than $ACMR_{20\%}$.

$$ACMR_I \geq ACMR_{20\%} \quad 8.7$$

Evaluation of the overstrength factor was carried out based on the following recommendations from FEMA P695:

- The system overstrength factor should be greater than the calculated largest average value of overstrength among the considered performance groups.
- Maximum allowable overstrength factor of 3 is recommended in ASCE/SEI 7-05 due to practical design considerations.
- In NBCC 2015, the maximum allowable overstrength factor is $R_o = 1.7$. For this research project, following NBCC 2015, the overstrength factor is set to $R_o = 1.5$.

Table 8.4: Acceptable values of adjusted collapse margin ratio (ACMR_{10%} and ACMR_{20%}) (FEMA 2009)

Total System Collapse Uncertainty	Collapse Probability				
	5%	10% (ACMR _{10%})	15%	20% (ACMR _{20%})	25%
0.275	1.57	1.42	1.33	1.26	1.20
0.300	1.64	1.47	1.36	1.29	1.22
0.325	1.71	1.52	1.40	1.31	1.25
0.350	1.78	1.57	1.44	1.34	1.27
0.375	1.85	1.62	1.48	1.37	1.29
0.400	1.93	1.67	1.51	1.40	1.31
0.425	2.01	1.72	1.55	1.43	1.33
0.450	2.10	1.78	1.59	1.46	1.35
0.475	2.18	1.84	1.64	1.49	1.38
0.500	2.28	1.90	1.68	1.52	1.40
0.525	2.37	1.96	1.72	1.56	1.42
0.550	2.47	2.02	1.77	1.59	1.45
0.575	2.57	2.09	1.81	1.62	1.47
0.600	2.68	2.16	1.86	1.66	1.50
0.625	2.80	2.23	1.91	1.69	1.52
0.650	2.91	2.30	1.96	1.73	1.55
0.675	3.04	2.38	2.01	1.76	1.58
0.700	3.16	2.45	2.07	1.80	1.60
0.725	3.30	2.53	2.12	1.84	1.63
0.750	3.43	2.61	2.18	1.88	1.66
0.775	3.58	2.70	2.23	1.92	1.69
0.800	3.73	2.79	2.29	1.96	1.72
0.825	3.88	2.88	2.35	2.00	1.74
0.850	4.05	2.97	2.41	2.04	1.77
0.875	4.22	3.07	2.48	2.09	1.80
0.900	4.39	3.17	2.54	2.13	1.83
0.925	4.58	3.27	2.61	2.18	1.87
0.950	4.77	3.38	2.68	2.22	1.90

8.3 Performance assessment of the proposed R_d factors using incremental dynamic analysis (IDA)

Incremental dynamic analysis (IDA) (Vamvatsikos and Cornell 2002) was used to compute the collapse risk. FEMA P695 suggests first to select the GMs for a 2% in 50 years uniform hazard spectrum (see Chapter 7 for the GM selection). Subsequently dynamic analyses have been carried out by scaling the GM records up to the collapse spectral acceleration.

8.3.1 Incremental dynamic analysis results

Initial approximation of the collapse spectral acceleration and interstorey drift were quantified using the SPO2IDA approach (Vamvatsikos and Cornell 2005). Based on a preliminary assessment, the GMs were scaled up until a spectral acceleration value triggered the collapse of

the building ($MISDR = 5\%$). In order to compute the collapse fragility curves and adjusted collapse margin ratio, the IDA was performed using OpenSees software (Mazzoni *et al.* 2006).

In order to assess the median and the standard deviation of the collapse intensity and to approximate the fragility curve, first, the partial IDA method was used (Baker 2015). Results of the partial IDA are depicted in Figure 8.3a. For the 10S-U building and for $R_d = 2$, a maximum intensity of 2.5 times the design intensity was considered and all analyses were conducted up to this intensity value. The partial IDA method is formulated as maximization problem to derive the lognormal distribution function parameter, $\hat{\theta}$ and $\hat{\beta}$, using the maximum likelihood function (Eq. 8.8). Using the probability of collapse points depicted in Figure 8.4, the maximum likelihood estimates $\hat{\theta} = 430\%$ and $\hat{\beta} = 0.5$ were obtained from the parametric analyses. The collapse fragility curve from the partial IDA is depicted in Figure 8.3b along with the collapse fragility curve derived from full-IDA (described subsequently). The two fragility curves are shown to be almost identical, validating the use of partial-IDA for the case study building and the considered ground motions.

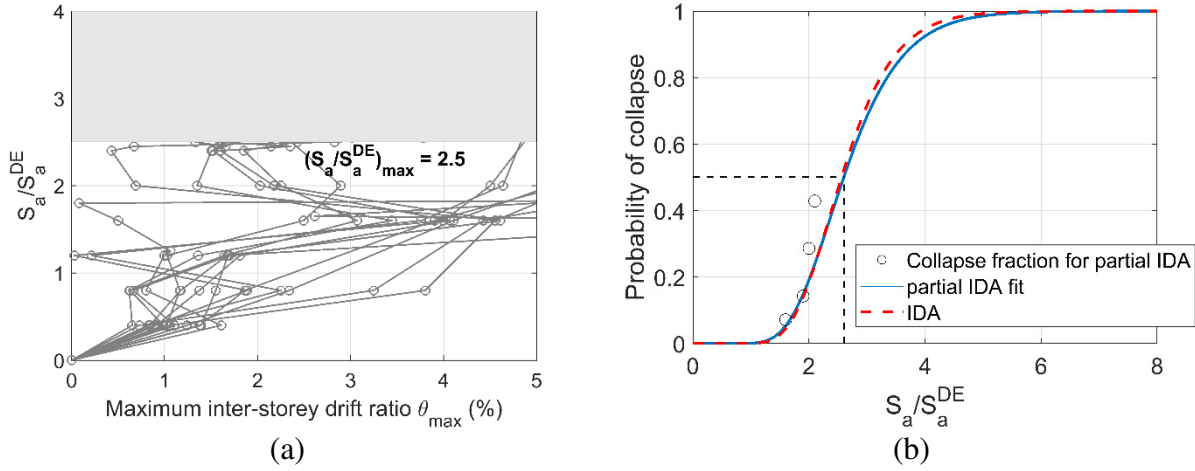


Figure 8.3: Partial IDA method for the 10S-U building for $R_d = 2$ in Y direction: a) IDA curves, and b) Collapse fragility curve

$$\begin{aligned} \{\hat{\theta}, \hat{\beta}\} = \operatorname{argmax}_{\theta, \beta} & \sum_{j=1}^m \left[\ln \phi \left(\frac{\ln(IM_i/\theta)}{\beta} \right) \right] \\ & + [n - m] \ln \left[1 - \Phi \left(\frac{\ln(IM_{max}/\theta)}{\beta} \right) \right] \end{aligned} \quad 8.8$$

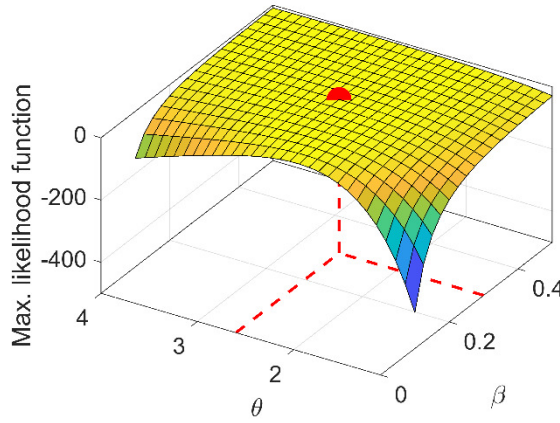


Figure 8.4: Parametric analysis and derivation of maximum likelihood parameters for the partial IDA lognormal distribution

Next, the IDA simulation was continued to get the collapse intensity values of all GMs. Figure 8.5 illustrates the IDA curves for the 10S-U building for $R_d = 2$ and $R_d = 3$. Figure 8.6 shows the IDA results for 15S-C and 20S-C buildings, also in the Y direction. The horizontal axis represents the maximum inter-story drift ratio (θ_{max}). The vertical axis gives the intensity measure which is defined as the spectral acceleration at the fundamental period of the building (S_a), normalized by its value for the design earthquake (S_a^{DE}). The IDA results shown in Figures 8.5 and 8.6 will be used to obtain the collapse fragility curves, and are discussed in the next section.

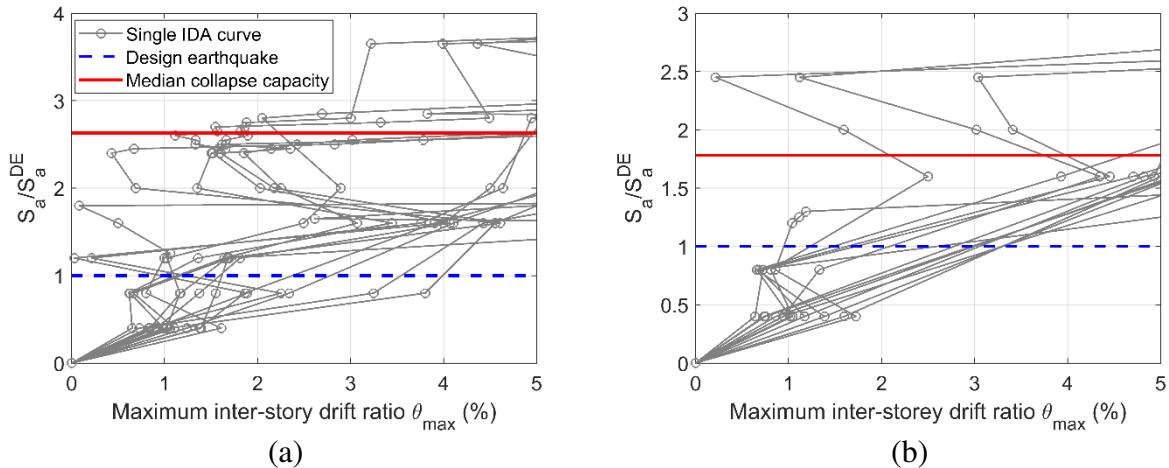


Figure 8.5: IDA curves of the 10S-U building in the Y direction: a) $R_d = 2$, and b) $R_d = 3$

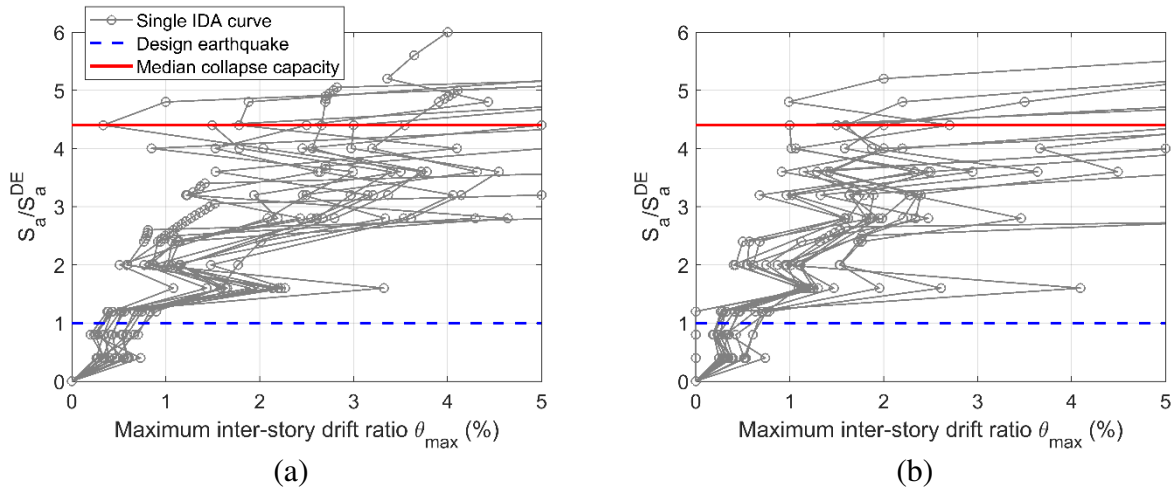


Figure 8.6: IDA curves for $R_d = 2$ in the Y direction, a) 15S-C and b) 20S-C buildings

8.3.2 Total system uncertainty

The total uncertainty (β_{TOT}) is determined with consideration of β_{RTR} , β_{DR} , β_{MDL} , and β_{TD} . Given its insignificant effect on the final *ACMR* value, FEMA P695 sets $\beta_{RTR} = 0.4$. The design requirement uncertainty (β_{DR}) was determined to be fair (Table 8.1) with $\beta_{DR} = 0.35$. For this selection the confidence in the bases of design requirement is considered as medium. Moreover, considering CLT as a new construction material and the complexity in characterizing the structural behavior of wood, the completeness and robustness in the design method for this hybrid building was tagged as medium. Since the experimental tests on this hybrid structure are limited to its component level, the uncertainty related to test data was selected as fair (Table 8.2) with $\beta_{TD} = 0.35$. Uncertainty related to modeling was selected to be fair (Table 8.3) with $\beta_{MDL} = 0.35$. Finally, based on these selected values, the $\beta_{TOT} = 0.75$ is computed using Eq. 8.5.

8.3.3 Collapse fragility curves

The fragility curves reflect the probability of collapse of the hybrid buildings. These curves are cumulative distribution functions (CDF) developed by fitting a lognormal distribution through collapse intensity values for all GMs. The probability of these collapse points was determined by dividing the number of GM records that initiated the collapse of building to the total number of GM records (15). Median collapse intensity values and standard deviation of the collapse data were used as an input to define the CDF. The fragility curve (Full-IDA) was developed by the actual obtained lognormal standard deviation of collapse data points, and the “adjusted curve” (Full-IDA adjusted) was developed with the same median but a standard deviation of $\beta_{TOT} = 0.75$. For 10S-U, the full- and adjusted-IDC collapse fragilities are depicted in Figure 8.7. The adjusted IDC, with higher standard deviation flattens the curve. The fragilities for 15S-C and 20S-C are depicted in Figure 8.8.

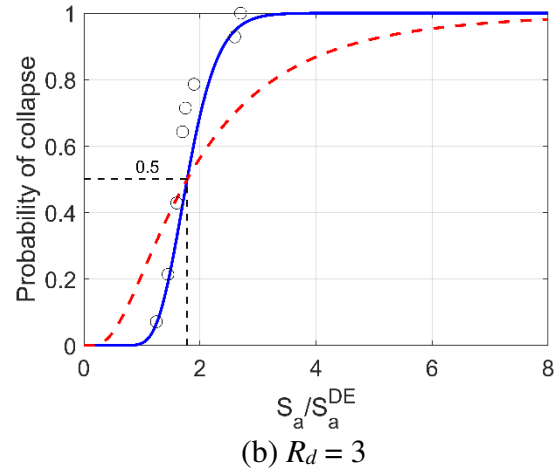
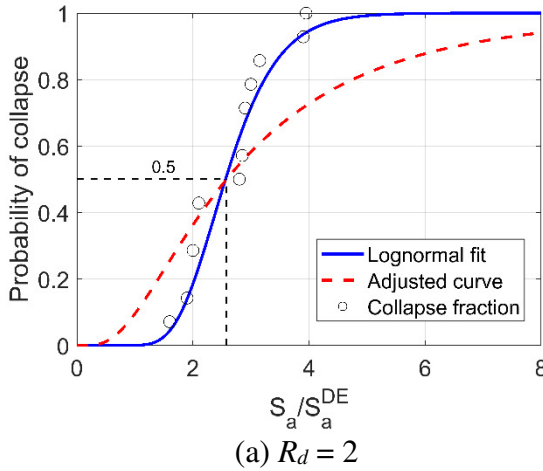


Figure 8.7: Collapse fragility curves for the 10S-U building, a) $R_d = 2$, and b) $R_d = 3$

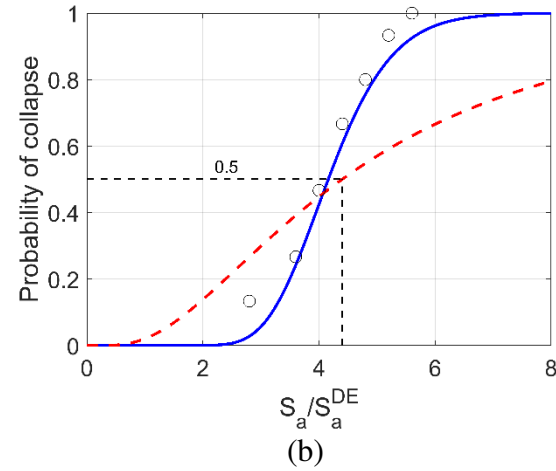
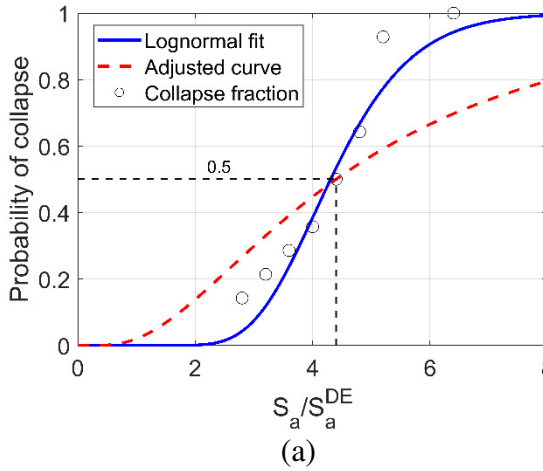


Figure 8.8: Collapse fragility curve for the $R_d = 2$, a) 15S-C and b) 20S-C buildings

FEMA P695 proposed acceptability criteria to verify the adequacy of initially assumed force reduction factors based on $ACMR_{10\%}$ and $ACMR_{20\%}$. The assumed R_d factors are accepted if the calculated $ACMR$ ratios were within the performance group and individually exceeded the values in Table 8.5. Accordingly, the proposed R_d factor are accepted if the calculated average $ACMR$ values within the performance group ($ACMR_{10\%}$) exceeds 2.61. Moreover, for individual criteria, the proposed factors were acceptable if the calculated $ACMR$ value ($ACMR_{20\%}$) exceeds 1.88. Since there exist one archetype per performance group, the $ACMR_{10\%} = 2.61$ was used for each archetype conservatively.

The *ACMR* results are summarized in Table 8.5. From Table 8.5, for 10S-U building, the $R_d = 2$ satisfies the $ACMR_{10\%} > 2.61$ criterion. As a result, it is selected as the appropriate R_d factor. For the R_o factor, the SPO analyses shows values higher than 1.7, which is the upper limit NBCC 2010. For the 20S-C, the $R_d = 3$ can potentially satisfy the design requirement. However, to make it consistent with all building heights, it is concluded that for the 10S-U, 15S-C and 20S-C buildings, the $R_d = 2$ and $R_o = 1.5$ factors will yield a safe design of the proposed timber-RC hybrid building.

Table 8.5: Performance evaluation table per FEMA P695

Building ID	R_d	R_o	$ACMR_{SPO2IDA}$	$ACMR_{IDA}$	FEMA P695 requirement	Pass/fail
10S-U	2	1.5	2.65	2.63	2.61	Pass
	3	1.5	1.83	1.78	2.61	Fail
15S-C	2	1.5	3.35	4.40	2.61	Pass
20S-C	2	1.5	4.45	4.40	2.61	Pass
	3	1.5	3.29	-	2.61	Pass
	4	1.5	2.51	-	2.61	Fail

Chapter 9

Conclusions and Future Recommendations

9.1 Wind tunnel testing and wind serviceability performance assessment study conclusions
HFPI wind tunnel tests were carried out on 10-, 15-, 20-, 30- and 40-storey hybrid mass-timber building models with a typical rectangular floor plan and 1:1.5 aspect ratio. Signal processing and statistical data analysis were performed to interpret the results. Mean and root mean square maps of pressure coefficient were presented for all building models. Probability distribution plots of the pressure signals show the non-Gaussian nature of the pressure field in the vortex shedding and wake regions. To support the finding, kurtosis and skewness contour maps were also produced. The non-Gaussian peak pressure coefficients were computed using a standard signal translation process. Both Gamma and Normal probability distribution types were used as a parent probability distribution of the measured pressure signals. The extreme value I (Gumbel) distribution was used to characterize the probability of the peaks. The peak pressure coefficients obtained from this project could be used for the cladding design of the case study high-rise hybrid mass-timber buildings.

The case study hybrid mass-timber buildings were structural designed using the dead, live, and 50-year wind loads from NBCC (2015) provisions and design wind speed maps. The buildings were assumed to be in Toronto, Ontario. We used both the worst-gravity and worst-wind load combinations rules of NBCC (2015) to provide adequate strength against extreme wind loads. The design process includes, design of the gravity system (CLT floor system, Glulam columns, RC spandrel beams), design of the CLT shear and core walls, RC link beams, HSK connectors for the factored gravity loads. Design checks of the LLRS were carried out considering the in-plane shear and coupled axial and out of plane bending demands due to combined effect of gravity and lateral wind loads.

Modal analysis was carried out to quantify the frequencies of vibration, mode shape, and generalized mass of the case study buildings. The Newmark's Beta method was used to directly solve the equation of motion and obtain the response of the tall wood buildings subjected to dynamic wind loads. The displacement responses from the analysis were converted to other response parameters (shear force, bending moment, acceleration) using the modal participation factors and modal combination rules proposed by Chen and Kareem (2005). The overall predicted design shear forces contain mean, background and resonant components. The mean and background components of the design wind loads were obtained by integrating the surface

pressures of the building from the aerodynamic wind tunnel test data. The resonance component is mainly due to the turbulent wind energy at the fundamental frequency of the buildings, which depends on the building's dynamic properties.

When subjected to wind loads, structures with a fundamental frequency less than 1 Hz responds dynamically with a significant contribution from resonance phenomena. Therefore, the performance assessment only considered case study mass-timber buildings taller than 15-storey. In the report, we presented and discussed the time history of structural responses (base moment, base shear, top floor acceleration, top floor displacement) of all the case study buildings. Design revisions were carried out by calculating the peak static wind loads from the presented time histories. The presented time histories clearly show the dependence of response parameters on building height. As expected, the responses of 15-storey buildings are mainly due to the mean and background components of the wind loads; a very little contribution from the resonance component. As presented in the report, the 30-storey building satisfies the serviceability criteria of NBCC (2015) with a small margin. The base shear and moment responses are an order of magnitude less than the response of the 40-storey building. Additionally, the distribution of shear and moment responses with the wind angle of attack between the 40- and 30-storey buildings is quite different. This might be due to the significant variation of mode shapes and fundamental frequencies of the buildings. As expected the peak floor acceleration responses of the 20- and 30-storey buildings are less than 25 milli-g (NBCC 2015). All the studied buildings except the 40-storey buildings satisfy the serviceability criteria of NBCC (2015). Therefore, from this project, it can be concluded that tall-wood buildings exceeding the height of 100 meters either need supplemental damping or "Wind bracing" through different hybridization techniques to satisfy the serviceability criteria of the 2015 NBCC.

In this project, the case study hybrid mass-timber buildings taller than 20 storey are extremely sensitive to wind-induced motions. For an assumed critical damping ratio of 1%, the 40-storey (136 meters tall) case study tall wood building did not meet the habitability criteria, and the 30-storey building satisfies the same criteria with a small safety margin. This finding implies that serviceability criteria than ultimate strength requirements could govern the design of tall wood buildings. Therefore, we used the First Order Second Moment (FOSM) approach to develop preliminary load factors for the serviceability-based wind design of tall mass-timber buildings. The result indicates that if the critical damping ratio of the building is more than 3%, the current load factor of NBCC (2015), 1.4, could be satisfactory. However, for low damped tall mass-timber

buildings, we recommend the use of $\gamma=1.6$, which could give extra safety for highly damped mass-timber buildings.

9.2 Seismic design factors conclusions

The seismic force modification factors are developed for the timber-concrete hybrid structure. The hybrid structure incorporates CLT panels for both building floors and laterally resisting shear-walls. Furthermore, reinforced concrete link-beams are considered for the 15 and 20-story buildings (15S-C and 20S-C, respectively) to couple the CLT walls. For connecting the CLT walls to the upper and lower story concrete (spandrel) beams, the modified HSK connection was used for both the hold-downs and the shear connectors. The FEMA P695 (FEMA 2009) was followed in this study to develop the archetype models and to quantify the seismic force modification factors. For the 10S-U building, two ductility factors (i.e. $R_d = 2$ and 3) were examined, while a value $R_d = 4$ was further considered for the 20S-C building.

The studied system consists a novel hybrid system design for high-rise timber-based buildings. Due to the lack of precedents for many of the elements, connections and sub-systems in the system, scarce experimental data exist to give extensive information on the system inelastic response. Therefore, several modelling assumptions needed to be made regarding both the CLT core as well as the perimeter frame systems. The modelling assumptions derive from the effective stiffness, strength and ductility properties of these systems. Modelling assumptions and design and assessment criteria add to the total uncertainty regarding the dynamic inelastic behavior of the system up to collapse. This uncertainty is reflected in the selection of the variance factors for the calculation of the adjusted collapse margin ratio (ACMR).

To validate the assumed force modification factors, the ACMR, as defined in FEMA P695, was calculated based on two procedures. As a first step in the assessment procedure, the SPO2IDA method was carried out. SPO2IDA is based on nonlinear-static analyses and SDOF-approximations of the global system, and it was carried out to give an initial estimate of the ACMR. The SDOF approximation is a major assumption of the SPO2IDA method since higher modal contributions are disregarded and an assumption has to be made regarding the lateral-force distribution. Based on the SPO2IDA, the factors $R_d = 2$ and $R_o = 1.5$ lead to values for the ACMR within the limits of FEMA P695.

As a second step, for the selected archetypes and R_d values, the IDA procedure was carried out. IDA is based on non-linear response-history analyses for a selected suite of GMs scaled to an incrementally-increasing seismic intensity. IDA gives an improved estimate of the ACMR, by explicitly accounting for the dynamic properties and response of the inelastic MDOF structure.

Based on the results of IDA, an $R_d = 2$ and an $R_o = 1.5$ seem to be appropriate for the studied system by providing with an ACMR value that is within the permitted range of FEMA-P695. In the selection of the smaller value for the force modification factor, the structural system limitations described in the following paragraph were also taken into account.

9.3 System limitations and future recommendations

The studied system was initially perceived and accordingly designed as a high-rise timber-concrete hybrid system, with the purpose to resist wind loads. The design for wind forces is an elastic design and thus it bears major differences with inelastic seismic design. For resisting seismic loads, the system has been found to have the following limitations:

- The concentration of most of the system's lateral stiffness at the central core, without adding any stiff elements at the perimeter leads to a torsionally-flexible system. As a result, torsional forces should be accounted for in the design detailing of the structural members of the system.
- The perimeter frames consisting of glulam columns and concrete beams need to be uncoupled (non-moment resisting), in order to not participate in the inelastic mechanism of the system. If the frames are coupled, they have to be explicitly accounted for in the seismic design procedure with provisions for combined bending, torsion and shear forces of the frame elements and connections. On the other hand, the need to uncouple the frame for in-plane response raises practical concerns regarding the connectivity of the frames, since they are still expected to transfer the beam torsional moments to the ground via torsional-moment-resisting connections with the glulam columns. As a result, an independent behaviour has to be attained for the frame connections in bending and in torsion.
- Scaling down the high-rise wind-resisting building to a low-to-medium-rise seismic-resisting building comes up with challenges regarding its structural system. The concrete beams reduce the building face area and as a result the wind-induced pressure on the high rise building. In addition, they enhance its over-turning resistance, by adding to its total weight. However, for the low-to-medium-rise seismic-resisting system, the beams add seismic mass and thus increase the inertial load of the building floors. Furthermore, they impose constraints to DOFs of the system that could otherwise be exploited to dissipate seismic energy (panel-to-panel sliding at the vertical joints). Additionally, the efficiency of the coupling beams is considerably reduced for the lower rises as compared with the high-rise building.

Based on the aforementioned limitations, future research directions can be defined for the hybrid mass-timber building. On one hand, a configuration study regarding the locations of the lateral-load resisting elements (CLT walls) should be carried out to enhance the torsional rigidity of the building system. Secondly, a more comprehensive study of assessing the effective stiffness, strength and ductility provided by the perimeter frames should be pursued. This study should consider the relative stiffness contribution of the glulam column – spandrel beam frames with respect to the segmented (discontinuous) CLT wall core. Experimental data would be required for the validation of this study. Finally, the consideration of several energy dissipation and self-centering devices could be examined to enhance the system performance and resilience.

Bibliography

- ASCE (2010). Minimum Design Loads for Buildings and Other Structures. ASCE Standard ASCE/SEI 7-10, Reson, VA.
- Atkinson, G. M., and Adams, J. (2013). Ground motion prediction equations for application to the 2015 Canadian national seismic hazard maps. *Canadian Journal of Civil Engineering*, 40, 988–998.
- Atkinson, G. M., and Goda, K. (2013). Probabilistic seismic hazard analysis of civil infrastructure. In: *Handbook of Seismic Risk Analysis and Management of Civil Infrastructure Systems* (S. Tesfamariam, K. Goda, eds.), Woodhead Publishing Ltd., Cambridge, United Kingdom, 3–28 (doi: 10.1533/9780857098986.1.3).
- Baker, J.W. (2011). The conditional mean spectrum: a tool for ground motion selection. *Journal of Structural Engineering*, 137, 322–331.
- Baker, J.W. (2015). Efficient analytical fragility function fitting using dynamic structural analysis. *Earthquake Spectra*, 31(1), 579-599.
- Bartlett, F.M., Hong, H.P. and Zhou, W. (2003). Load factor calibration for the proposed 2005 edition of the National Building Code of Canada: Statistics of loads and load effects. *Canadian Journal of Civil Engineering*, 30(2), 429-439.
- Bashor, R., Kijewski-Correa, T., and Kareem, A. (2005). “On the wind-induced response of tall buildings: the effect of uncertainties in dynamic properties and human comfort thresholds.” In Proceedings of Americas Conference on Wind Engineering, Baton Rouge, LA, USA.
- Bashor, R., and Kareem, A. (2009). “Probabilistic assessment of occupant comfort in tall buildings. In Structures Congress 2009: Don't Mess with Structural Engineers: Expanding Our Role” Structures Congress April 30-May 2, 2009, Austin, Texas, United States.
- Bezabeh, M. A., Bitsuamlak, G. T., Popovski, M., and Tesfamariam, S. (2018a). Probabilistic serviceability-performance assessment of tall mass-timber buildings subjected to stochastic wind loads: Part I-structural design and wind tunnel testing. *Journal of Wind Engineering and Industrial Aerodynamics*, 181, 85-103.
- Bezabeh, M. A., Bitsuamlak, G. T., Popovski, M., and Tesfamariam, S. (2018b). Probabilistic serviceability-performance assessment of tall mass-timber buildings subjected to stochastic wind loads: Part II-structural reliability analysis. *Journal of Wind Engineering and Industrial Aerodynamics*, 181, 112-125.
- Bezabeh, M.A., Bitsuamlak, G., and Tesfamariam, S. (2018c). Risk-based wind design of tall mass-timber buildings. The 2018 Canadian Society for Civil Engineering, Structural Specialty Conference, Fredericton, NB, Canada.
- CSA (Canadian Standards Association). (2014). *Engineering Design in Wood*. CSA O86-14. Canadian Standards Association, Toronto, ON.
- Casagrande, D., Doudak, G., Mauro, L.(2018). Analytical approach to establishing the elastic behavior of multipanel CLT shear walls subjected to lateral loads. *Journal of Structural Engineering*, 144(2), 1–13.
- Cassidy, J.F., Rogers, G.C., Lamontagne, M., Halchuk, S., and Adams, J. (2010). Canada's earthquakes: the good, the bad, and the ugly. *Geoscience Canada*, 37, 1–16.
- Chen, Z., and Chui, Y.-H. (2017). Lateral load-resisting system using mass timber panel for high-

- rise buildings. *Frontiers in Built Environment: Earthquake Engineering*, 3(July). <https://doi.org/10.3389/fbuil.2017.00040>.
- Chen, X. and Kareem, A. (2004). Equivalent static wind loads on buildings: New model. *Journal of Structural Engineering*, 130(10), 1425–1435.
- Davenport, A.G. (1964). Note on the distribution of the largest value of a random function with application to gust loading. *Proc. Inst. Civ. Eng.*, 28(2), 187–196.
- Davenport, A.G. (1983). The relationship of reliability to wind loading. *Journal of Wind Engineering and Industrial Aerodynamics*, 13(1-3), 3-27.
- Dabaghi, M., Saad, G., and Allhassania, N. (2019). Seismic collapse fragility analysis of reinforced concrete shear wall buildings. *Earthquake Spectra*, 35(1), 383-404.
- Dragoiescu, C., Garber, J., and Kumar, S.S., (2006). A comparison of force balance and pressure integration techniques for predicting wind-induced response of tall buildings. In: Structural engineering and public safety proceedings of the structures congress, Structures Congress, 18-21 May 2006, St. Louis, Missouri, United States.
- ESDU (Engineering Sciences Data Unit) (1974). Characteristics of atmospheric turbulence near the ground. No. 74031.
- Fairhurst, M. (2014). Dynamic analysis of the FFTT system. MSc dissertation, University of British Columbia.
- FEMA. (2009). *P695 Quantification of Building Seismic Performance Factors*. Redwood City, California: Applied Technology Council.
- FEMA. (2004). NEHRP Recommended Provisions for Seismic Regulations for New Buildings and Other Structures, FEMA 450-2/2003 Edition, Part 2: Commentary, Federal Emergency Management Agency, Washington, D.C.
- Goda, K., and Atkinson, G.M. (2011). Seismic performance of wood-frame houses in southwestern British Columbia. *Earthquake Engineering & Structural Dynamics*, 40, 903–924.
- Goda, K., and Taylor, C.A. (2012). Effects of aftershocks on peak ductility demand due to strong ground motion records from shallow crustal earthquakes. *Earthquake Engineering & Structural Dynamics*, 41(15), 2311–2330.
- Goda, K., Campbell, G., Hulme, L., Ismael, B., Ke, L., Marsh, R., Sammonds, P., So, E., Okumura, Y., Kishi, N., Koyama, M., Yotsui, S., Kiyono, J., Wu, S., and Wilkinson, S. (2016). The 2016 Kumamoto earthquakes: cascading geological hazards and compounding risks. *Frontiers in Built Environment*, 2(19), doi: 10.3389/fbuil.2016.00019.
- Goda, K., Wenzel, F., and De Risi, R. (2015). Empirical assessment of nonlinear seismic demand of mainshock-aftershock ground motion sequences for Japanese earthquakes. *Frontiers in Built Environment*, 1(6), doi: 10.3389/fbuil.2015.00006.
- Green, M., and Karsh, J. E. 2012. Tall wood—The Case for Tall Wood Buildings. Wood Enterprise Coalition, Vancouver, Canada.
- Halchuk, S.C., Adams, J.E., and Allen, T.I. (2015). Fifth generation seismic hazard model for Canada: grid values of mean hazard to be used with the 2015 National Building Code of Canada, Geological Survey of Canada, Open File 7893, 22 p.
- Halchuk, S., Adams, J., and Allen, T.I. (2016). Fifth generation seismic hazard model for Canada: crustal, in-slab, and interface hazard values for southwestern Canada; Geological Survey of Canada, Open File 8090, 19 p.

- Halchuk, S., Allen, T.I., Adams, J., and Rogers, G.C. (2014). Fifth generation seismic hazard model input files as proposed to produce values for the 2015 National Building Code of Canada, Geological Survey of Canada, Open File 7576, 15 p.
- Haselton, C. B., Liel, A.B., Lange, S. T., and Deirlein, G. G. (2008). *Beam-column element model calibrated for predicting flexural response leading to global collapse of RC frame buildings*. Pacific Earthquake Engineering Research Center, Berkeley, CA.
- Hong, H. P., Hong, P., & Wang, W. (2010). Reliability of steel frames designed in accordance with the National Building Code of Canada seismic provisions and its implication in codified design. *Engineering Structures*, 32(5), 1284-1291.
- Hyndman, R.D., and Rogers, G.C. (2010). Great earthquakes on Canada's west coast: a review. *Canadian Journal of Earth Sciences*, 47, 801–820.
- Ibarra, L. F., and Krawinkler, H. (2005). Global collapse of frame structures under seismic excitations. Pacific Earthquake Engineering Research Center, Berkeley, CA.
- Ibarra, L.F., Medina, R.A., and Krawinkler, H. (2005). Hysteretic models that incorporate strength and stiffness deterioration. *Earthquake Engineering & Structural Dynamics*, 34(12), 1489-1511.
- Gavric, I. Fragiocomo, M., Popovski, M., A. C., Reinhardt, H. W., and Garrecht, H. (2013). Materials and Joints in Timber Structures: Recent Developments of Technology. RILEM Bookseries, 9(April 2015). <https://doi.org/10.1007/978-94-007-7811-5>.
- Izzi, M., Casagrande, D., Bezzi, S., Pasca, D., Follesa, M., and Tomasi, R. (2018). Seismic behaviour of cross-laminated timber structures: A state-of-the-art review. *Engineering Structures*, 170, 42-52.
- Kim, T., and Foutch, D.A. (2007). Application of FEMA methodology to RC shear wall buildings governed by flexure. *Engineering Structures*, 29(10), 2514-2522.
- Lignos, D.G., and Krawinkler, H. (2012). Development and utilization of structural component databases for performance-based earthquake engineering. *Journal of Structural Engineering*, 139(8), 1382-1394.
- Merrick, R. and Bitsuamlak, G.T. (2009). Shape effects on the wind-induced response of high-rise buildings. *Journal of Wind Engineering*, 6(2), 1-18.
- Mitchell, D., Tremblay, R., Karacabeyli, E., Paultre, P., Saatcioglu, M. and Anderson, D.L. (2003). Seismic force modification factors for the proposed 2005 edition of the National Building Code of Canada. *Canadian Journal of Civil Engineering*, 30(2), 308-327.
- Minciarelli, F., Gioffrè, M., Grigoriu, M., and Simiu, E. (2001). Estimates of extreme wind effects and wind load factors: Influence of knowledge uncertainties. *Prob. Eng. Mech.*, 16(4), 331–340.
- NRC (National Research Council). (2015). *National Building Code of Canada 2015*. National Research Council of Canada, Ottawa, ON.
- Pei, S., van de Lindt, J.W., Popovski, M., Berman, J.W., Dolan, J. D., Ricles, J., Rammer, D.R. (2016). Cross-laminated timber for seismic regions: Progress and challenges for research and implementation. *Journal of Structural Engineering*, 142(4), E2514001.
- Sadek, F. and Simiu, E., (2002). Peak non-Gaussian wind effects for database-assisted low-rise building design. *Journal of Engineering Mechanics*, 128(5), 530-539.
- SOM. (2013). Timber Tower Research Project. Skidmore, Owings & Merrill LLP.

<https://doi.org/10.1017/CBO9781107415324.004>

STRUCTURLAM. (2016). CROSSLAM®CLT Technical Design Guide.

Suresh Kumar, K. and Stathopoulos, T. (1998). Power spectra of wind pressures on low building roofs. *Journal of Wind Engineering and Industrial Aerodynamics*, 74-76, 665-674.

Tesfamariam, S., and Goda, K. (2015). Loss estimation for non-ductile reinforced concrete building in Victoria, British Columbia, Canada: effects of mega-thrust M_w 9-class subduction earthquakes and aftershocks. *Earthquake Engineering & Structural Dynamics*, 44, 2303–2320.

Tesfamariam, S., Stiemer, S.F., Bezabeh, M., Goertz, C., Popovski, M., and Goda, K. (2015). Force based design guideline for timber-steel hybrid structures : steel moment resisting frames with CLT infill walls [R]. doi:<http://dx.doi.org/10.14288/1.0223405>

Vamvatsikos, D. and Cornell, A. (2006). Direct estimation of the seismic demand and capacity of oscillators with multi-linear static pushovers through IDA. *Earthquake Engineering & Structural Dynamics*, 35(9), 1097-1117.

Warsido, W. and Bitsuamlak, G.T. (2015). Synthesis of wind tunnel and climatological data: A Copula based approach. *Structural Safety*, 57, 8-17.

Zhang, X. (2017). Seismic design of timber steel hybrid high-rise buildings (Doctoral dissertation, University of British Columbia).

Zhang, X., Popovski, M. and Tannert, T. (2018). High-capacity hold-down for mass-timber buildings. *Construction and Building Materials*, 164, 688–703.